DESIGN AND SIMULATION OF LITHIUM NIOBATE WAVEGUIDES AND DEVICES

BY

HUA WANG
B.Sc., M. Eng.

DESIGN AND SIMULATION OF
LITHIUM NIOBATE WAVEGUIDES AND DEVICES

DESIGN AND SIMULATION OF LITHIUM NIOBATE WAVEGUIDES AND DEVICES

By

HUA WANG
B.Sc., M. Eng.

A Thesis
Submitted to the School of Graduate studies
in Partial Fulfillment of the Requirements
for the Degree
Master of Engineering

McMaster University

MASTER OF ENGINEERING (2005) MCMASTER UNIVERSITY
(Electrical and Computer Engineering) Hamilton, Ontario

TITLE: **Design and Simulation of Lithium Niobate Waveguides and Devices**

AUTHOR: Hua Wang
B. Sc. (Nanjing University of Science and Technology)
M. Eng. (Nanjing University of Science and Technology)

SUPERVISOR: Dr. W. -P. Huang
Professor, Department of Electrical and Computer Engineering

CO-SUPERVISOR: Dr. C. Q. Xu
Professor, Department of Engineering Physics

NUMBER OF PAGES: xii, 127

ABSTRACT

This thesis deals with the research development in design and modeling of the lithium niobate ($LiNbO_3$) optical waveguides. In particular, the material and modal properties of the titanium (Ti)-indiffusion and annealed proton-exchange (APE) are investigated thoroughly. By linking the relation of the design and fabrication parameters with modal properties of the $LiNbO_3$ waveguides, a comparative study on modeling and characterization of diffused optical waveguides is presented.

First we investigate the diffusion, exchange, and annealing processes analytically and numerically. Through comparing different models of index change with concentration of the related species such as titanium and hydrogen, the material properties can be calculated. The accuracy and the scope of validity for the analytical methods are also investigated. Some important fabrication and design parameters are abstracted and used for calculating the index distribution of the optical waveguides. Then, by applying a rigorous finite difference method, the modal properties of the diffused waveguides, such as modal profile, effective index, and coupling loss with the standard fiber, can be calculated. The modal properties of the optical waveguides directly link to the fabrication parameters of corresponding waveguides. Based on modal properties of optimized waveguides, the device performances of the related devices can be easily obtained.

Based on the analysis of general $LiNbO_3$ optical waveguides, the detail material and modal properties of the titanium-indiffusion and APE $LiNbO_3$ optical waveguides are further investigated. Their fabrication processes are reviewed and typical process parameters are given. Furthermore, by comparing with measurement results of the titanium-indiffusion and APE $LiNbO_3$ optical waveguides made in McMaster University, the relation between the waveguide modal performance and design parameters is built through some effective methods and ready to be applied in the design of optical devices.

Finally, we reconstruct the refractive index distribution of the optical waveguides by using the measurement results of modal properties.

Acknowledgements

I would like to express my sincere thanks and deep appreciation to my dedicated supervisors, Dr. Wei-Ping Huang and Dr. Chang-qing Xu, for their guidance, support, and encouragement. I benefited from their diverse insights and interests throughout this research work. I would also like to thank Dr. Xun Li, and Dr. Shiva Kumar, in Photonic Research Group, Dr. Chenglin Xu in Apollo Inc., for their kind assistance and helpful comments. The use of the photonic CAD software from Apollo Inc. (Hamilton, Ontario) was acknowledged with deep gratitude.

I would like to deeply appreciate the members of the Photonic Research Group at the Department of Electrical and Computer Engineering and the Department of Engineering Physics for their help and friendship, especially Bo Chen, Wan-Gou Liang, Fang-fang, Yu Chen. I would also like to thank the staff of the Department of Electrical and Computer Engineering for their support and collaboration.

Last, not least, I would like to thank my husband, Lin-Ping Shen and our lovely daughters, Julia and Jenny, for their continued love, patience, inspiration, and support.

Contents

List of Figures

List of Tables

Chapter 1

Introduction

The continuous expansion of data communications, telecommunications, and high speed internet services is accelerating the research and development of broadband high capacity optical and high flexibility wireless networks for worldwide communications traffic. Due to its huge bandwidth nature, the WDM (wavelength division multiplexing) optical network becomes one of the hottest research areas for next-generation internet services, including IP (internet protocol)-routing WDM networks and WDM optical access networks. In order to increase the capacity and high flexibility of communication networks, optical components such as lasers, modulators, switches, wavelength routers, wavelength multiplexers, and wavelength converters are key devices for WDM optical networks. By integrating all optical functions of individual components into one package at the wafer level for low cost and high efficiency, waveguide-based photonic integrated circuits (PICs), or photonic lightwave circuits (PLCs), play an important role in realizing multi-function and low cost of the optical components.

As one of the important basic optical waveguides, due to some unique features such as large electro-optic (EO) coefficients and high second-order nonlinearity, lithium niobate ($LiNbO_3$)-based optical waveguides have been used in many components such as optical modulators, switches, directional couplers, mode splitters, phase shifters, and wavelength converters. They have been received considerable attention for four decades and still stay as a hot research topic [1]-[7]. There are tremendous theoretical and experimental efforts to analyze and design the $LiNbO_3$-based diffused waveguides and related devices.

1.1 Optical waveguides

Optical waveguides (WGs) are the fundamental component of the optical communication systems. Figure 1.1 shows the schematic view of the optical waveguide in corresponding Cartesian coordinate system (x, y, and z), in which the waveguide cross-section is in the *x-y* plane, the wave propagation is along the *z*-axis, and the coordinate zero point (0, 0, 0) is located at the interface between $LiNbO_3$ substrate and buffer layer. In general, optical waveguides are guided-wave devices composed of a guiding core (i. e., the shade area in Figure 1.1) and a cladding region, in which the refractive index of the core is higher than that of the cladding and the light is confined in the transverse plane (i. e., *x-y plane* in Figure 1.1). Their guiding mechanism is based on the total internal reflection (TIR) effect. Except the well-known fiber structure, the common-used optical waveguide is a planar waveguide in which the light is confined in the cross-section and propagates in the *z* direction.

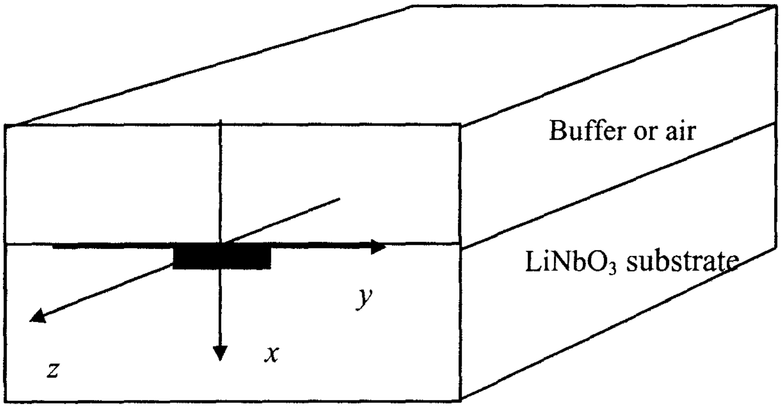

Figure 1.1 A schematic view of coordinate system of the diffused waveguide

- Optical waveguides
  - Planar
    - Step - index
      - Silica - based waveguide
      - Semiconductor - based waveguide
      - Other waveguides
    - Graded - index
      - $LiNbO_3$ waveguides
        - Ti - indiffusion
        - Annealed proton exchange
        - Others
      - Other waveguides
  - Fiber
    - Step - index
    - Graded - index

Figure 1.2 Simple classification of the optical waveguides

According to the different index profiles, optical waveguides can be classified into two kinds of waveguides: step-index waveguide and graded-index waveguide. According to the property of the base material (i. e., wafer), optical waveguides can be categories into several technologies such as III-V (e. g., InP and GaAs) semiconductor, Silica-on-Silicon (SOS), Silicon-on-Insulator (SON), Polymer, lithium niobate ($LiNbO_3$), and Ion-exchange. According to the index variations of the media with the direction of the electric filed, optical waveguides also can be categorized into three kinds of medium: isotropic, uniaxial, and biaxial. Due to the anisotropy nature, the $LiNbO_3$ crystal is a uniaxial media. If the principle axis of media is chosen as shown in Figure 1.1, we have that $n_{xx} = n_{yy} \neq n_{zz}$ for the $LiNbO_3$ crystal, where n_{xx}, n_{yy} and n_{zz} are the refractive indices along the x, y, z direction. Figure 1.2 shows the typical classification of the optical waveguides. From Figure 1.2, we know that the $LiNbO_3$-based waveguide is one of the planar uniaxial graded-index waveguides.

1.2 $LiNbO_3$-based Optical Waveguides

Bulk $LiNbO_3$ crystal is a synthetic, single-crystal, and negative uniaxial oxide material. It was first discovered in 1949 by B. T. Matthias and J. P. Remeika [8]. $LiNbO_3$ has some applications in non-linear optics and electro optics. With some diffusion processes such as titanium diffusion and proton exchange, $LiNbO_3$ optical waveguide has diffused index profile and can be used as guided-wave devices. The first commercial $LiNbO_3$-based device, an optical modulator, was introduced in 1986 by Crystal Technology Inc.[9]. By using different $LiNbO_3$ crystal orientations, some typical optical diffused waveguides are realized and some features such as large electro-optic coefficients and high second-order nonlinearity can be utilized. Without loss of generality, for example, Z-cut X-propagating $LiNbO_3$ optical waveguides is shown in Figure 1.3, where X, Y, Z are the crystal orientations. By compared with the waveguide coordinators x, y, z as shown in Figure 1.1. The refractive index tensor of the corresponding optical waveguide has the form of uniaxial crystal ($n_{xx} = n_{yy} \neq n_{zz}$) and can be expressed as follows,

$$\tilde{n}^2 = \begin{pmatrix} n^2_{xx} & 0 & 0 \\ 0 & n^2_{yy} & 0 \\ 0 & 0 & n^2_{zz} \end{pmatrix} = \begin{pmatrix} n^2_e & 0 & 0 \\ 0 & n^2_o & 0 \\ 0 & 0 & n^2_o \end{pmatrix} \tag{1.1}$$

where n_{xx}, n_{yy} and n_{zz} are the refractive indices along the x, y, z direction, n_o and n_e are the refractive indices of ordinary and extraordinary beam, respectively. It is worth to note that, due to the nature of proton exchange process, only the extraordinary index n_e is increased and only one type of modes in proton exchange waveguides is supported. For example, *X*-cut proton exchanged waveguides support TE modes and *Z*-cut proton exchanged waveguides support TM modes. The detailed definition of the crystal orientation cuts and relation between them are described in Appendix A.

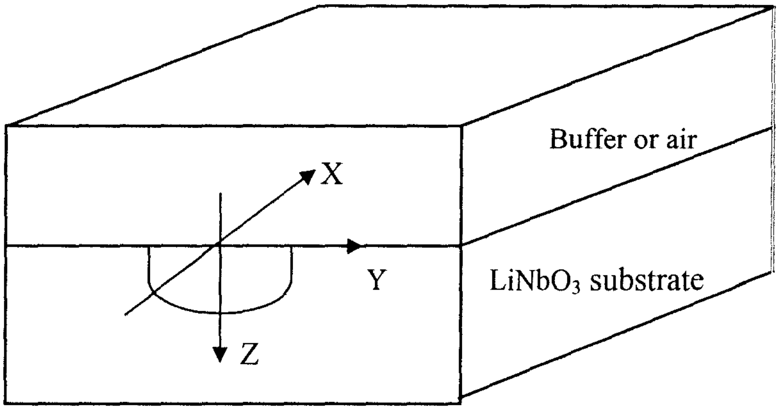

Figure 1.3 The crystal orientation (*X*, *Y*, *Z*) of $LiNbO_3$ optical waveguides

Several techniques are used to fabricate the $LiNbO_3$-based optical waveguide substrates. They are titanium in-diffusion, annealed proton exchange, Li_2O out-diffusion, Silver-lithium ion exchange, ion-implantation, and liquid phase epitaxy. The Li_2O out-diffusion is the first available technique. Low optical confinement and single polarization are the major drawbacks of this technique. The second fabrication technique is the proton exchange process with high optical confinement. However, it has some shortcomings such as high propagation loss and reduced electro-optic efficiency due to the high proton concentration during the proton exchange process. In order to overcome these problems, some advanced fabrication techniques were developed. Among them, the titanium in-diffusion and annealed proton exchange, as underlined in Figure 1.2, are the two important techniques and focused in this thesis. Figure 1.4 shows the cross-section of $LiNbO_3$ optical waveguides, where the species strip (e. g., Ti strip in $Ti:LiNbO_3$ waveguides and H^+ proton strip in APE $LiNbO_3$ waveguides) has the width w and thickness τ. In the current model, the Ti strip in $Ti:LiNbO_3$ waveguides is above the y-axis, and the H^+ proton strip in APE $LiNbO_3$ waveguides is below the y-axis.

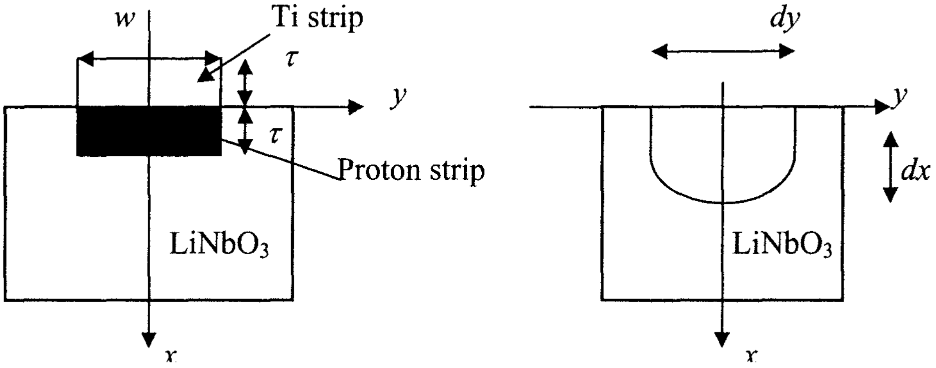

(a) Before in-diffusion/annealing (b) After in-diffusion/annealing

Figure 1.4 The cross-section of $LiNbO_3$ optical waveguides

Due to some unique features, such as easy fabrication and low loss, titanium in-diffused $LiNbO_3$ waveguides are most widely used. In this technique, a Ti-strip with a certain thickness and width is deposited on the $LiNbO_3$ substrate, and then the substrate is heated in a diffusion furnace with time at a high temperature. In order to prevent the out-diffusion of lithium, some type of wet oxygen-like atmosphere or gas flow condition is needed. Indices within the diffusion region are changed and become graded-index distribution during the thermal diffusion process. Since the indices within the diffusion region are usually slightly higher than those in the surrounding area, the weakly guided diffused waveguides are fabricated. The detailed fabrication process is described in Appendix B.

Annealed proton exchange (APE) on the $LiNbO_3$ material is an effective technique for the formation of low-loss and high electro-optical optical waveguides. In this technique, hydrogen (H^+) ions in the liquid (e. g., benzoic or pyrophosphoric acid) are exchanged with Lithium (Li^+) ions that lead to a large increase in the extraordinary refractive index. Then annealing is used to eliminate compositional instabilities in the exchanged layer and to restore desirable optical properties such as the large electro-optical coefficients. While a step-like hydrogen profile is retained during the early stages of annealing at relatively low temperature, annealing at higher temperature produces a highly graded profile. Therefore, the two-step proton-exchange and thermal annealing process are used in the formation of optical annealed proton-exchange (APE) $LiNbO_3$ waveguides. Again, typical fabrication process for APE $LiNbO_3$-based waveguides is given in Appendix B.

1.3 Motivations and Objectives

As we know, $LiNbO_3$-based optical waveguides, one of the important basic optical waveguides, have been used in many components such as optical modulators, and wavelength converters. There are tremendous theoretical and experimental efforts to analyze and design the $LiNbO_3$-based diffused waveguides and related devices. In order to design the optical waveguides with certain required properties, the relation between the required properties and design parameters should be understood. Due to complexity of the overall process, in general, the material properties and modal characteristics of the $LiNbO_3$-based diffused waveguides were investigated separately. For example, the material properties of the waveguides were researched based on the simplified model of modal calculation, or the modal characteristics of the waveguides are calculated based on the analytical model of the material properties. There are few efforts to link this whole process. In order to understand the working principle of the $LiNbO_3$-based diffused waveguides, it is necessary to do some research study on modeling and design methods of the diffused waveguides by considering the whole fabrication process, which includes material properties, fabrication parameters, index profiles, near-filed patterns, and inverse index algorithms.

In this research, based on the titanium in-diffusion and annealed proton-exchange waveguides, the material properties and modal characteristics of the lithium niobate optical waveguides based on are investigated thoroughly. By linking the relation of the design and fabrication parameters with modal properties of the $LiNbO_3$-based waveguides, a comparative study on modeling and characterization of diffused optical waveguides is presented [7].

Based on the analysis of general $LiNbO_3$ optical waveguides, the detail material and modal properties of the titanium in-diffusion and annealed proton-exchange $LiNbO_3$ optical waveguides can be further investigated. Through comparing different models of index change with concentration of the related species such as titanium and hydrogen, the material properties can be obtained. Therefore, the relation between the waveguide modal performance and design parameters can be built through some effective methods and this process is very useful to be applied in the design of optical devices.

1.4 Thesis Outline

This thesis presents the design and simulation of lithium niobate ($LiNbO_3$)-based optical waveguides. The material models of $LiNbO_3$-based optical waveguides are summarized and solved analytically and numerically, and corresponding index models are obtained. Also, based on the finite difference method, the modal properties are calculated and used to compare with the measured values of Ti: $LiNbO_3$ and APE $LiNbO_3$ optical waveguides.

In Chapter 2, the material models of $LiNbO_3$-based optical waveguides are summarized and solved analytically and numerically, and corresponding index models are obtained. Based on the finite difference method, the modal properties such as modal profiles and coupling loss with fiber are calculated in Chapter 3. In Chapter 4 and Chapter 5, the individual material and model properties for the Ti:$LiNbO_3$ and APE $LiNbO_3$ optical waveguides are presented and compared with the measured values of the different optical waveguides. In Chapter 6, by utilizing the measured values, some reverse algorithms are used to obtain the index profile of the optical waveguides. Finally, conclusions are given in Chapter 7.

Chapter 2

Material Properties of $LiNbO_3$ Optical Waveguides

As we know, the modal properties of the diffused waveguides are solely dependent on its refractive index distribution, which can be calculated by the diffusion parameters of the diffusion processes such as well-known titanium in-diffusion and annealed proton exchange (APE) in lithium niobate ($LiNbO_3$). In this chapter, we start the two-dimensional (2D) Fickian diffusion equation for general diffusion process. Then the corresponding analytical and numerical solutions are given. Finally, the general relations between material properties and index properties are presented.

2.1 Bulk Lithium Niobate ($LiNbO_3$)

For the successful use of $LiNbO_3$ functional devices and nonlinear experiments, knowledge of bulk $LiNbO_3$ uniaxial crystal's refractive indices as a function of wavelength, temperature, and Li_2O ratio is necessary. In particular, the stoichometric (i.e., 50 % of Li_2O) and congruent (i. e., 48.6 % of Li_2O) bulk $LiNbO_3$ crystals, on which most of practical $LiNbO_3$-based devices are based, are most useful.

For the sake of simplicity, we assume that the operating wavelength is within communication bands (i.e., 0.1~2.0 μm) and far from the absorption peak. For the congruently grown (melting) $LiNbO_3$ (i. e., 48.6 mol % of Li_2O, or 94.2 mol % of Li/Nb), the dispersion relations of $(Li_{0.486}Nb_{0.514})_2O_3$ material have the following equations, which we label as *Model* 1[10],

$$\begin{aligned} n_o^2 &= 4.9130 + \frac{0.1173 + 1.65\times10^{-8}T^2}{\lambda^2 - (0.212 + 2.7\times10^{-8}T^2)^2} - 2.78\times10^{-2}\lambda^2 \\ n_e^2 &= 4.5567 + 2.605\times10^{-7}T^2 + \frac{0.097 + 2.7\times10^{-8}T^2}{\lambda^2 - (0.201 + 5.4\times10^{-8}T^2)^2} - 2.24\times10^{-2}\lambda^2 \end{aligned} \qquad (2.1)$$

where λ is the wavelength in nanometers (nm) (e. g., 400 ~ 4000 nm), and T is the temperature in Kelvin (K) (e. g., 292 ~ 647K). From the Reference [10], we know that standard deviation of (2.1) is 2.2x10^{-4}. At the room temperature (or 20°C), the refractive indices of ordinary and extraordinary n_o and n_e of the $LiNbO_3$ crystal can be simplified as the following modified Sellmeier equations with 5x10-5 standard deviation, which we label as *Model* 2 [11][12],

$$\begin{aligned} n_o^2 &= 4.9048-[0.11768/(0.04750-\lambda^2)]-0.027169\lambda^2 \\ n_e^2 &= 4.5820-[0.099169/(0.04432-\lambda^2)]-0.021950\lambda^2 \end{aligned} \qquad (2.2)$$

where λ is the wavelength in micrometers (μm). From (2.2), the refractive index n_o = 2.2866 and n_e = 2.2026 at a wavelength of 0.6328 μm, and n_o = 2.2112 and n_e = 2.1381 at a wavelength of 1.55 μm. In general, based on the function of wavelength and composition, the refractive index $n(\lambda)$ of bulk $LiNbO_3$ crystal can be expressed as the following general Sellmeier formula [13],

$$n^2 = 1+\sum_{i=0}^{\infty}\frac{A_i}{1-\lambda_i^2/\lambda^2} \qquad (2.3)$$

where A_i and λ_i (i = 0, 1, 2, ...) are amplitude coefficients and oscillator wavelengths determined by fitting with experimental results. In general, with respect to the stoichiometric composition, Lithium niobate can be grown with Li deficits up to 4% proving a comparably wide composition range for $LiNbO_3$ single crystals. Usually, the generalized two-term Sellmeier formula (i = 0 and 1) is utilized [14],

$$n^2 = 1+\frac{A_0(\delta)}{1-\lambda_0^2/\lambda^2}+\frac{A_1(\delta)}{1-\lambda_1^2/\lambda^2} \qquad (2.4)$$

where $A_0(\delta)=A_0(1-\gamma\delta)$, $A_1(\delta)=A_1\delta$, δ is a function of mole ratio of Li_2O material, and γ has a value between 0 (only contributions for plasmons, dependent on O^{2-} content) and 4/5 (only transitions into the conduction band, dependent on Nb^{5+} content). For the sake of convenience and simplicity, we chose $\gamma = 3/10$ and δ with the relation [14],

$$\delta = \frac{10}{3}\frac{50-C_{Li}}{100} \qquad (2.5)$$

where C_{Li} donates a mole ratio (mol %) of Li_2O material. By combining (2.2) with (2.3), the general material model of bulk $LiNbO_3$ is deduced, which we label as *Model* 3,

$$n_i^2 = 1 + \frac{50 + C_{Li}}{100}\frac{A_{0,i}}{1 - \lambda_{0,i}^2/\lambda^2} + \frac{50 - C_{Li}}{100}\frac{A_{1,i}}{1 - \lambda_{1,i}^2/\lambda^2} \tag{2.6}$$

where λ is wavelength in nanometers (nm), n_i($i = e, o$) are the extraordinary and ordinary refractive indices of $LiNbO_3$. By fitting the above generalized Sellmeier equation to the experimental data, a set of four coefficients of $A_{0,i}$, $A_{1,i}$, $\lambda_{0,i}$, and $\lambda_{1,i}$ ($i = e, o$) in (2.6) can be extracted. For example, the typical values of A_i and λ_i of bulk $LiNbO_3$ with a range from 46.1 to 50.0 mol % of Li_2O are the following [14],

$$\begin{array}{ll} A_{0,o} = 3.854 & A_{0,e} = 3.489 \\ \lambda_{0,o} = 186.535\ nm & \lambda_{0,e} = 176.466\ nm \\ A_{1,o} = 3.552 & A_{1,e} = 6.004 \\ \lambda_{1,o} = 208.592\ nm & \lambda_{1,e} = 223.479\ nm \end{array} \tag{2.7}$$

where λ is the wavelength in nm with a range from 405 to 1650 nm.

By substituting (2.7) into (2.6), we have,

$$\begin{aligned} n_o^2 &= 1 + \frac{50 + C_{Li}}{100}\frac{3.854}{1 - (186.535/\lambda)^2} + \frac{50 - C_{Li}}{100}\frac{3.552}{1 - (208.592/\lambda)^2} \\ n_e^2 &= 1 + \frac{50 + C_{Li}}{100}\frac{3.489}{1 - (176.466/\lambda)^2} + \frac{50 - C_{Li}}{100}\frac{6.004}{1 - (223.479/\lambda)^2} \end{aligned} \tag{2.8}$$

Figure 2.1 shows extraordinary and ordinary refractive indices of bulk $LiNbO_3$ as a function of wavelength for various crystal compositions with experimental results. The agreement between experimental data and the numeral fits is excellent. In general, the standard deviation is 1.8×10^{-3} [14], which is mainly due to uncertainties in the concentration data. In order to compare the results from different models, the extraordinary and ordinary refractive indices as a function of wavelength of the congruent $(Li_{0.486}Nb_{0.514})_2O_3$ (20°C, 48.6 mol % of Li_2O) are calculated and shown in Figure 2.2. From Figure 2.2, it is found that, except slight difference of n_e due to different measured environments, they agree well. Figure 2.3 shows the extraordinary and ordinary refractive indices of mode3 as a function of wavelength of the congruent $(Li_{0.486}Nb_{0.514})_2O_3$ (24.5°C, 48.6 mol % of Li_2O) with some experimental results.

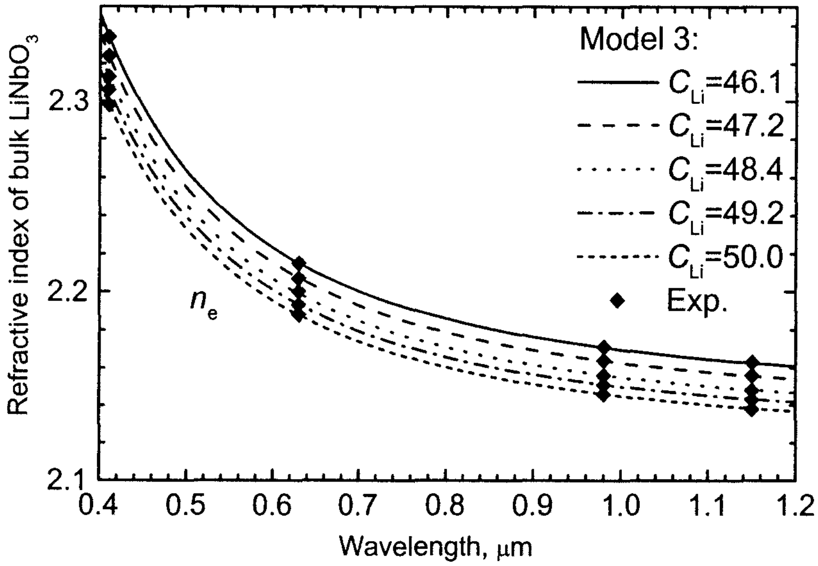

(a) Extraordinary refractive index.

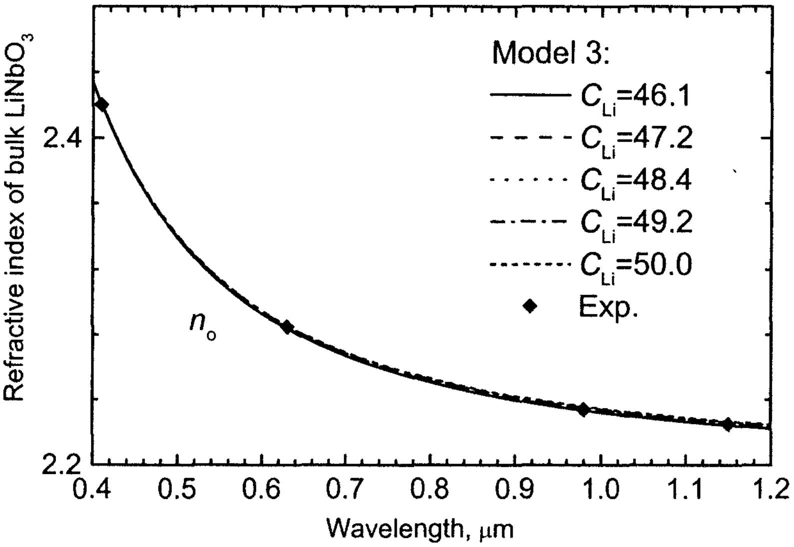

(b) Ordinary refractive index.

Figure 2.1 Extraordinary and ordinary refractive indices of bulk LiNbO$_3$ as a function of wavelength for various crystal compositions with experimental results: (a) Extraordinary index and (b) Ordinary index.

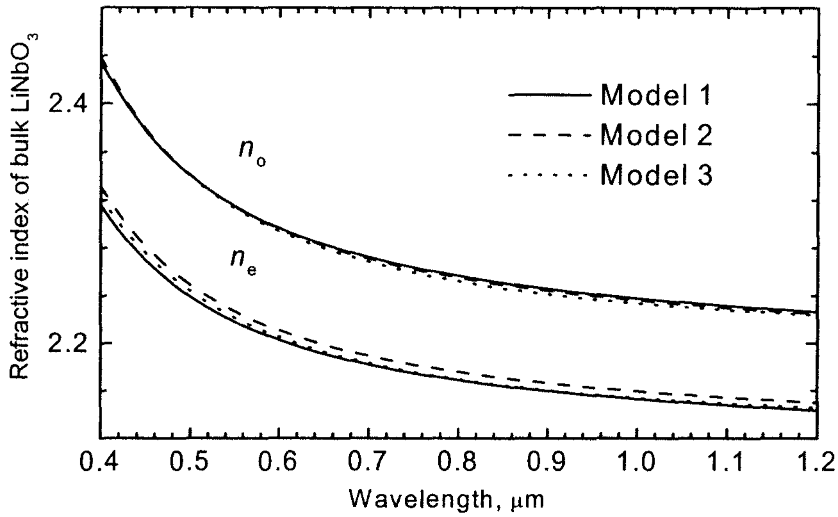

Figure 2.2 Extraordinary and ordinary refractive indices of three modes as a function of wavelength of the congruent $(Li_{0.486}Nb_{0.514})_2O_3$ (20°C, 48.6 mol % of Li_2O).

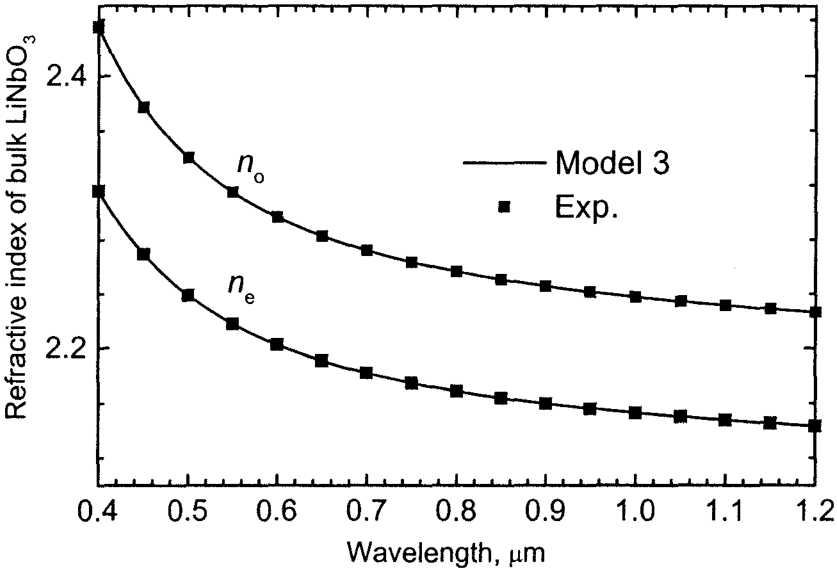

Figure 2.3 Extraordinary and ordinary refractive indices of mode3 as a function of wavelength of the congruent $(Li_{0.486}Nb_{0.514})_2O_3$ (24.5°C, 48.6 mol % of Li_2O) with some experimental results [14].

Finally, the refractive indices of ordinary and extraordinary beam, n_o and n_e of the congruently melting $LiNbO_3$ crystal at wavelength of 0.6328 μm with their experiment results are calculated and shown in Table 2.1.

Table 2.1 Extraordinary and ordinary refractive indices of mode 3 as a function of wavelength of the congruent $(Li_{0.486}Nb_{0.514})_2O_3$ (48.6 mol % of Li_2O) with some experimental results

Source	n_o	n_e	Standard deviation	note
Model 1	2.2875	2.2002	$2.2\text{x}10^{-4}$	T=20°C
Mode 2	2.2849	2.1969	$5\text{x}10^{-5}$	T=20°C
Model 3	2.2865	2.2024	$1.8\text{x}10^{-4}$	
Exp. [14]	2.2866	2.2026		T=20°C
Exp.[12]	2.2865	2.2012	$5.0\text{x}10^{-4}$	Prism coupling method

From above figure, we are able to know that the three models about ordinary refractive index are in very good agreements while the three models about extraordinary index have a slight deviation.

2.2 Two Dimensional (2D) Fickian Diffusion Equation

For the sake of simplicity, we assume that the longitudinal direction of considered diffused waveguide is invariant ($\partial/\partial z = 0$). The diffusion of the diffused waveguide can be modeled by the two-dimensional (2D) Fickian thermal diffusion equation [15],

$$\frac{\partial C}{\partial t} = \frac{\partial}{\partial x}(D_x \frac{\partial C}{\partial x}) + \frac{\partial}{\partial y}(D_y \frac{\partial C}{\partial y}) \tag{2.9}$$

where $C(x, y, t)$ is the relative concentration distribution of the diffusion species such as Ti^+ of $Ti:LiNbO_3$ waveguide or H^+ of APE $LiNbO_3$ waveguide, D_x and D_y are the diffusion coefficients along the x-axis and y-axis, respectively, which are given approximately by [16]

$$D_i = D_0^i e^{-E_0^i/kT} = D_0^i e^{-T_0^i/T}, \ i = x, y \tag{2.10}$$

where D_0^i ($i = x$, y) is the diffusion constant, which is proportional to the jump distance and to the jump frequency of the diffusion atoms in the crystal, and $E_0^i (= kT_0^i, i = x, y)$ is the activation energy along i direction, which produced by the surrounding ions or atoms of the crystal. The constant k is Boltzmann's constant and T is the diffusion temperature in Kevin (K).

In general, the diffusion coefficients are not necessarily constant in the crystal since this activation energy may be affected locally by defects, vacancies, or compositional variations in the crystal. In most of cases, the diffusion coefficients can be calculated as a constant of independence of x and y. Therefore, the 2D diffusion equation of (2.10) can be simplified as

$$\frac{\partial C}{\partial t} = D_x \frac{\partial^2 C}{\partial x^2} + D_y \frac{\partial^2 C}{\partial y^2} \tag{2.11}$$

which can be found in most of published papers.

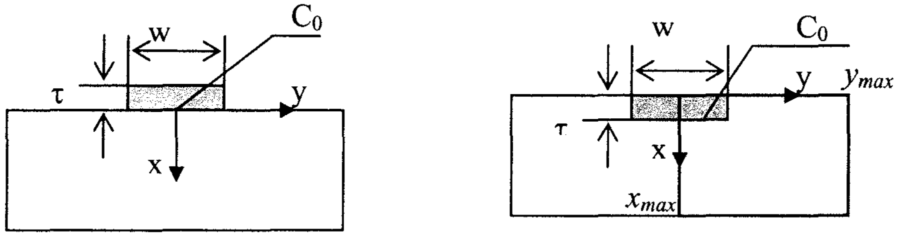

(a) Original (b) Equivalent

Figure 2.4 The transformation of the computational region

In order to simplify our problem, we consider the initial layer of strip just below the surface (i. e., $0 < x < \tau$, $-w/2 < y < w/2$) as shown in Figure 2.4. This approximation is appropriate for diffusion times that are long compared to the time required to diffuse the source material into the bulk. The symmetric mathematical space can be reduced to the computation window: $0 < x < x_{max}$, $0 < y < y_{max}$. In order to model the diffusion equation efficiently, we assume the computation window (i. e., x_{max} and y_{max}) large enough, which leads the general boundary conditions (C, $D_x\partial C/\partial x$, and $D_y\partial C/\partial y$ continuous) into the boundary conditions of the computation window:

$$C(x_{max}, y, t) = 0 \text{ for all } 0 < y < y_{max} \tag{2.12}$$

$$C(x, y_{max}, t) = 0 \text{ for all } 0 < x < x_{max} \tag{2.13}$$

$$\frac{\partial C(x,y,t)}{\partial x}\Big|_{x=0} = 0 \text{ for all } 0 < y < y_{max} \tag{2.14}$$

$$\frac{\partial C(x,y,t)}{\partial y}\bigg|_{y=0} = 0 \text{ for all } 0 < x < x_{max} \tag{2.15}$$

As described in Figure 2.4, the physical initial conditions of strip layer are in the region: $0 < x < \tau$, $-w/2 < y < w/2$ with the thickness τ and the half width $w/2$,

$$C(x, y, t)\big|_{t=0} = C_0, \quad 0 < x < \tau, \ -w/2 < y < w/2 \tag{2.16}$$

$$C(x, y, t)\big|_{t=0} = 0, \quad \text{elsewhere.} \tag{2.17}$$

where $C(x, y, t)$ is the diffusion concentration and C_0 is the initial diffusion concentration.

2.3 Analytical Solution of 2D Diffusion Equation

For a strip of film deposited on a $LiNbO_3$ substrate with a width w and thickness τ deposited on a $LiNbO_3$ substrate as shown in Figure 2.4, the waveguide cross section is in the x-y plane, and the wave propagation is along the z-axis. In the absence of any external perturbation or source, the diffusion equation of (2.9) with constant diffusion coefficients D_x and D_y can be rewritten as

$$\frac{\partial C(x,y,t)}{\partial t} = D_x \frac{\partial^2 C(x,y,t)}{\partial x^2} + D_y \frac{\partial^2 C(x,y,t)}{\partial y^2} \tag{2.18}$$

The significant feature of (2.18) of the 2D diffusion equations is that the x and y dependences of $C(x, y, t)$ are separable. By using the method of separate variables, the approximate analytical solution of the diffusion equation goes as follow:

$$C(x, y, t) = C_0 F(x, t) G(y, t) \tag{2.19}$$

where $F(x,t)$ and $G(y,t)$ are one dimensional functions, and C_0 is the initial diffusion concentration (e. g., the atomic density of the Ti strip in $Ti:LiNbO_3$ waveguide). The corresponding physical parameters (i. e., C_0, diffusion coefficients D_x and D_y) are determined by the individual diffusion techniques such as Ti indiffusion and proton exchange. By putting (2.19) into (2.18), 1D diffusion concentration functions $F(x, t)$ and $G(y, t)$ are defined by the following one dimensional (1D) diffusion equations,

$$\frac{\partial F(x,t)}{\partial t} = D_x \frac{\partial^2 F(x,t)}{\partial x^2} \tag{2.20}$$

$$\frac{\partial G(y,t)}{\partial t} = D_y \frac{\partial^2 G(y,t)}{\partial y^2} \tag{2.21}$$

where the boundary conditions and initial conditions are modified as follows

$$F(x_{max}, t) = F(-x_{max}, t) = 0 \tag{2.22}$$

$$G(y_{max}, t) = G(-y_{max}, t) = 0 \tag{2.23}$$

$$F(x,t)\,|_{t=0} = 1,\ -\tau < x < \tau; \qquad F(x, t)\,|_{t=0} = 0, \text{ elsewhere.} \tag{2.24}$$

$$G(y,t)\,|_{t=0} = 1,\ -w/2 < y < w/2; \ C(y,t)\,|_{t=0} = 0, \text{ elsewhere.} \tag{2.25}$$

where $F(x, t)$ and $G(y, t)$ are the 1D diffusion concentrations of the unity strip source along the x-axis and y-axis, respectively. It is worth to note that the symmetrical boundary conditions of (2.16) and (2.17) are eliminated by extending the boundary conditions into whole region: $-x_{max} < x < x_{max}$ and $-y_{max} < y < y_{max}$. Therefore, the extended strip has width w and thickness 2τ. From the diffusion theory [15], the solution of 1D diffusion equation is given from a line source of unity strength at y' along z,

$$g(y, y', t) = \frac{1}{2\sqrt{\pi D_y t}} \exp(-(y-y')^2/(2\sqrt{D_y t})^2) = \frac{1}{d_y\sqrt{\pi}} \exp(-(y-y')^2/d_y^2) \tag{2.26}$$

where $-w/2 \le y' \le w/2$, $d_y = 2\sqrt{D_y t}$ is the diffusion length along the y-axis and t is the diffusion time in the fabrication process. In general, the above expression holds when t is much larger than the diffused time from the strip to the bulk $LiNbO_3$, which means that concentration has a Gaussian-like distribution. By considering the w-width strip source, which is made up of a series of line sources integrating y' from $-w/2$ to $w/2$, the concentration of 1D diffusion equation becomes,

$$G(y, t) = \int_{-w/2}^{w/2} g(y, y', t)dy' = \frac{1}{d_y\sqrt{\pi}} \int_{-w/2}^{w/2} \exp(-(y-y')^2/d_y^2)dy' \tag{2.27}$$

Let $(y-y')/d_y = u$, or $dy' = -d_y du$, the concentration $G(y, t)$ of 1D diffusion equation with a unity strength strip source becomes,

$$G(y,t) = -\frac{1}{\sqrt{\pi}} \int_{(y+w/2)/d_y}^{(y-w/2)/d_y} \exp(-u^2)du$$

$$= \frac{1}{\sqrt{\pi}} \int_0^{(w/2-y)/d_y} \exp(-u^2)du + \frac{1}{\sqrt{\pi}} \int_0^{(y+w/2)/dy} \exp(-u^2)du$$

$$=\frac{1}{2}\left[erf\left(\frac{w/2-y}{d_y}\right)+erf\left(\frac{w/2+y}{d_y}\right)\right] \tag{2.28}$$

where the error function $erf(y) = \frac{2}{\sqrt{\pi}}\int_0^y \exp(-u^2)du$ was used and its properties are described in Appendix C. It is noticed that $erf(y)|_{y\text{->}\pm\infty}= \pm 1$ and boundary conditions of (2.23) at $y = \pm y_{max}$ are met naturally. Similarly, the concentration $F(x, t)$ is given from a 2τ-thickness strip source of unity strength along z,

$$F(x,t)=\frac{1}{2}\left[erf\left(\frac{\tau-x}{d_x}\right)+erf\left(\frac{\tau+x}{d_x}\right)\right] \tag{2.29}$$

where $d_x = 2\sqrt{D_x t}$ is the diffusion length along the x-axis. Therefore, the analytical solution of the 2D diffusion equation of (2.18) with constant diffusion coefficients D_x, D_y of a strip source defined by boundary conditions of (2.12)-(2.17) is

$$C(x,y,t)=\frac{C_0}{4}\left[erf\left(\frac{\tau-x}{d_x}\right)+erf\left(\frac{\tau+x}{d_x}\right)\right]\left[erf\left(\frac{w/2+y}{d_y}\right)+erf\left(\frac{w/2-y}{d_y}\right)\right] \tag{2.30}$$

where $d_x = 2\sqrt{D_x t}$ and $d_y = 2\sqrt{D_y t}$ are the diffusion lengths along the x-axis and the y-axis, respectively. According to the property of concentration functions $F(x, t)$ and $G(y, t)$, which are described in Appendix C, the function $C(x, y, t)$ has the maximum surface diffusion concentration when $x = y = 0$, which is called the surface diffusion concentration C_s,

$$C_s = erf\left(\frac{\tau}{d_x}\right)erf\left(\frac{w}{2d_y}\right)C_0 \tag{2.31}$$

If the thickness of the strip is very thin (or $d_x \gg \tau$), the exponent factor $\exp((y-y')^2/d_x^2) \approx \exp(y^2/d_x^2)$, and the 1D concentration function of $F(x, t)$ can be simplified as

$$F(x,t)=\frac{1}{d_x\sqrt{\pi}}\int_{-\tau}^{\tau}\exp(-(x-x')^2/d_x^2)dx' \approx \frac{2\tau}{d_x\sqrt{\pi}}\exp\left(-\frac{x^2}{d_x^2}\right) \tag{2.32}$$

Then, the 2D concentration $C(x, y, t)$ becomes,

$$C(x,y,t)=\frac{\tau}{2d_x\sqrt{\pi}}C_0\exp\left(-\frac{x^2}{d_x^2}\right)\left[erf\left(\frac{w/2+y}{d_y}\right)+erf\left(\frac{w/2-y}{d_y}\right)\right] \tag{2.33}$$

which can also be found in many published papers [18].

On the other hand, if the width of the strip is very large (or $w \gg d_y$), the 1D concentration function of $G(y, t)$ is simplified as

$$G(y,t) = \frac{1}{2}[erf(\frac{w/2-y}{d_y})+erf(\frac{w/2+y}{d_y})] \approx erf(\frac{w}{2d_y}) \approx 1 \tag{2.34}$$

where the property of the error function, described in Appendix C, was used. Then, the 2D concentration $C(x, y, t)$ becomes,

$$C(x,y,t)=\frac{1}{2}C_0[erf(\frac{\tau-x}{d_x})+erf(\frac{\tau+x}{d_x})] \tag{2.35}$$

where d_x is the diffusion lengths along the x-axis.

2.4 Numerical Solution of 2D Diffusion Equation

In the previous section, we assume that diffusion coefficients of the strip are constant in the whole computation domain and independent of process parameters. Actually, the diffusion coefficients may not be constant in the crystal because the activation energy may be affected locally by defects, vacancies, or compositional variations. In order to consider this variation, the 2D diffusion equation of (2.18) belongs to a initial value problem and can be solved by the numerical methods such as the finite difference method (FDM). In general, there are various possibilities to solve the diffusion equation of (2.18), but only some of which are stable. The well-known Crank-Nicholson scheme is stable, which we employ here. For the sake of simplicity, the uniform-mesh sizes $\Delta_i(=\Delta x)$, Δ_j $(=\Delta y)$, and Δt are used. We may employ the following "forward and backward in half time, centered in space" scheme for the 1D diffusion equation of (2.20) as shown in Figure 2.5,

$$C_i^{n+1/2}=C_i^n+\Delta t D_i\frac{C_{i+1}^n-2C_i^n+C_{i-1}^n}{2\Delta_i^2}=C_i^{n+1}-\Delta t D_i\frac{C_{i+1}^{n+1}-2C_i^{n+1}+C_{i-1}^{n+1}}{2\Delta_i^2} \tag{2.36}$$

or

$$\Delta t D_i C_{i-1}^{n+1} - 2(\Delta t D_i + \Delta x^2) C_i^{n+1} + \Delta t D_i C_{i+1}^{n+1} = -2\Delta x^2 C_i^n - \Delta t D_i (C_{i+1}^n - 2C_i^n + C_{i-1}^n)$$

which is the well-known Crank-Nicholson scheme, an implicit form and stable. By applying the corresponding boundary conditions (BCs) such as Neumann BC: $C_{i-1} = C_i$, and Dirichet BC: $C_{i+1} = -C_i$ at $\Delta_i /2$ ($i = 1, n_x$), we have the following matrix form,

$$[M]_{(n_x \times n_x)}[C]_{(n_x \times 1)} = [R]_{(n_x \times 1)} \tag{2.37}$$

where $[M]$ is a regional matrix and updating C for each time step is easily realized.

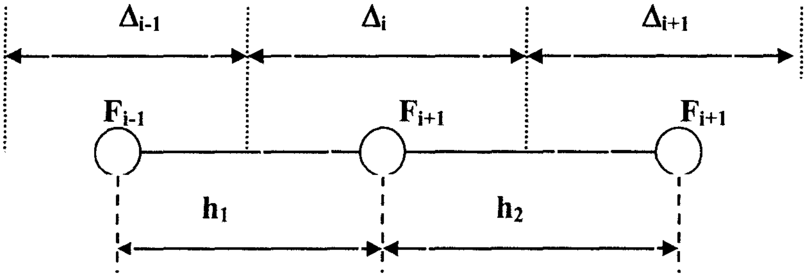

Figure 2.5 The 1D finite difference (FD) mesh allocation

In general, the diffusion coefficients are the functions of variables x and y, and concentrations (nonlinear), the2D diffusion equation can be solved numerically (e. g., FDM method) as shown in Figure 2.6.

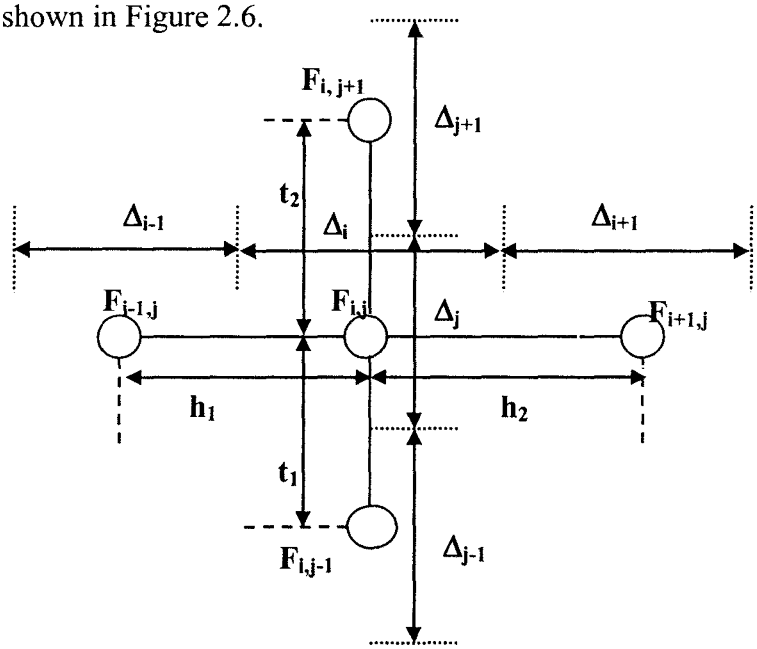

Figure 2.6 The 2D finite difference (FD) mesh allocation

From Figure 2.6 , the corresponding finite difference term of (2.9) can be obtained,

$$\frac{\partial F}{\partial f}\Big|_i = \frac{1}{h_1+h_2}\left(F^{i+1}-F^{i-1}\right)+O(\Delta_i^2) \qquad (2.38)$$

$$\frac{\partial}{\partial f}\left(D\frac{\partial F}{\partial f}\right)\Big|_i = \frac{2}{h_1+h_2}\left(F^{i+1}\frac{D_{i+1/2}}{h_2}-F^{i}\left(\frac{D_{i+1/2}}{h_2}+\frac{D_{i-1/2}}{h_1}\right)+F^{i-1}\frac{D_{i-1/2}}{h_1}\right)+O(\Delta_i^{\,2}) \qquad (2.39)$$

where the non-uniform mesh sizes Δ_{i-1}, Δ_i, and Δ_{i+1} are used. The mesh distances are that $h_1 = (\Delta_{i-1}+\Delta_i)/2$ and $h_2 = (\Delta_{i+1}+\Delta_i)/2$. The diffusion coefficients at the mesh nodes:

$$D_{i-1/2} = (D_{i-1}\Delta_{i-1}+D_i\,\Delta_i)/2h_1\,;\ D_{i+1/2} = (D_{i+1}\Delta_{i+1}+D_i\,\Delta_i)/2h_2 \qquad (2.40)$$

By employing the "forward and backward in half time, centered in space" scheme, the 2D diffusion equation can be discretized as follows,

$$\begin{aligned}
&-C_{k-nx}^{n+1}\frac{D_{i,j-1/2}^{y}}{S_{1y}}-C_{k-1}^{n+1}\frac{D_{i-1/2,j}^{x}}{S_{1x}}+C_{k}^{n+1}\left(1+\frac{D_{i+1/2,j}^{x}}{S_{2x}}+\frac{D_{i-1/2,j}^{x}}{S_{1x}}+\frac{D_{i,j+1/2}^{y}}{S_{2y}}+\frac{D_{i,j-1/2}^{y}}{S_{1y}}\right)\\
&-C_{k+1}^{n+1}\frac{D_{i+1/2,j}^{x}}{S_{2x}}-C_{k+nx}^{n+1}\frac{D_{i,j+1/2}^{y}}{S_{2y}}=C_{k-nx}^{n}\frac{D_{i,j-1/2}^{y}}{S_{1y}}+C_{k-1}^{n}\frac{D_{i-1/2,j}^{x}}{S_{1x}} \qquad (2.41)\\
&+C_{k}^{n}\left(1+\frac{D_{i+1/2,j}^{x}}{S_{2x}}+\frac{D_{i-1/2,j}^{x}}{S_{1x}}+\frac{D_{i,j+1/2}^{y}}{S_{2y}}+\frac{D_{i,j-1/2}^{y}}{S_{1y}}\right)+C_{k+1}^{n}\frac{D_{i+1/2,j}^{x}}{S_{2x}}+C_{k+nx}^{n}\frac{D_{i,j+1/2}^{y}}{S_{2y}}
\end{aligned}$$

where $k=(j-1)\times n_x+i$, where $i=1, \ldots, n_x$, $j=1, \ldots, n_y$, and $k=1, \ldots, n_x n_y$, $S_x=h_{1x}+h_{2x}$ and $S_y=h_{1y}+h_{2y}$, $S_{1x}=S_x h_{1x}/\Delta t$, $S_{2x}=S_x h_{2x}/\Delta t$ and $S_{1y}=S_y h_{1y}/\Delta t$, $S_{2y}=S_y h_{2y}/\Delta t$. By applying the corresponding BCs at $\Delta_i/2$ (i, or j = 1, n_x or n_y), we have the following matrix form,

$$[M]_{(n_x n_y \times n_x n_y)}[C]_{(n_x n_y \times 1)} = [R]_{(n_x n_y \times 1)} \qquad (2.42)$$

where M is a band matrix with the bandwidth ($2n_x$+1) and dimension n_xxn_y, in which n_x and n_y are the numbers of meshes in x and y directions. The concentration distribution can be obtained by using band solvers.

In order to obtain the scope of validity of the model parameters (i.e., window size w_x, mesh size Δx, time step Δt, and non-uniform mesh ratio) in the numerical analysis, we first investigate the optical waveguide with following parameters: D = 4 μm²/hrs, τ = 4 μm, t =1 hour, and w_x =15 μm. Figure 2.7 shows the concentration solution of diffusion equation with a function of window size (a), uniform mesh size (b), time step(c), and non-uniform mesh ratio($\Delta x_{nx}/\Delta x_1$) (d). It is found that, due to the nature of the boundary condition, the window size should be reasonable large. The selection of the mesh size and time step depends on the size of the waveguide. In order to cope with the small size of the film strip, the non-uniform mesh has to be used. Once the scope of validity of the model parameters is identified, the diffusion equation with the different diffusion functions and boundary conditions can be easily solved, where the analytical solution of (2.30) may not be accurate enough.

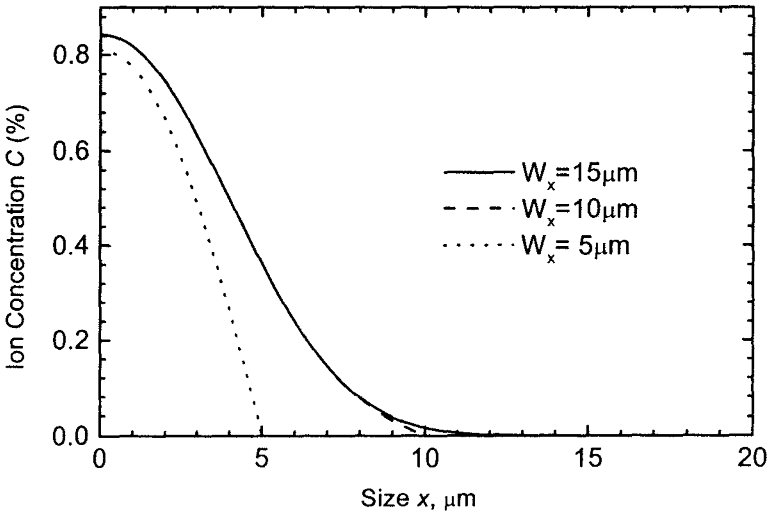

(a) A function of window size

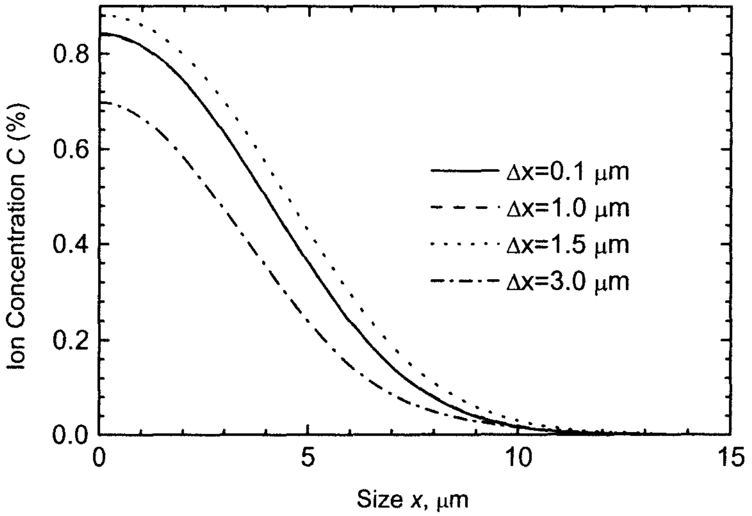

(b) A function of uniform mesh size

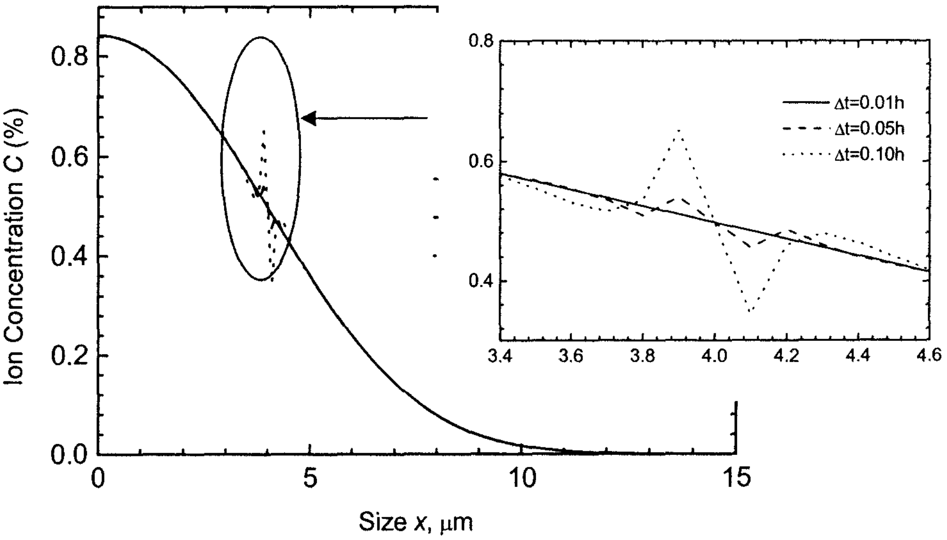

(c) A function of time step

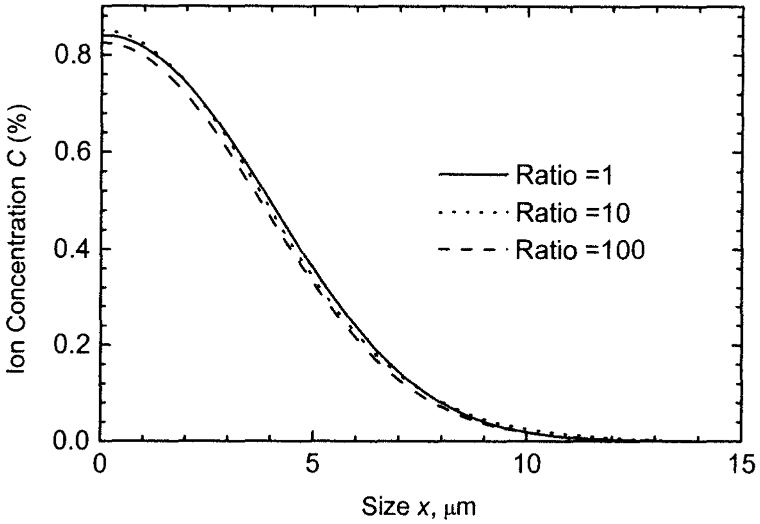

(d) A function of non-uniform mesh ratio

Figure 2.7 Concentration solution of diffusion equation with a function of window size (a), uniform mesh size (b), time step(c), and non-uniform mesh ratio (d).

2.5 Index Model of LiNbO$_3$ Optical Waveguides

After obtaining the species concentration, the corresponding transverse profiles for the ordinary and extraordinary refractive indices can be calculated accordingly,

$$\begin{aligned} n_o(x,y,\lambda) &= n_{ob}(\lambda) + \Delta n_o(x,y,\lambda) \\ n_e(x,y,\lambda) &= n_{eb}(\lambda) + \Delta n_e(x,y,\lambda) \end{aligned} \tag{2.43}$$

where $\Delta n_o(x,y,\lambda)$ and $\Delta n_e(x,y,\lambda)$ are the change of refractive indices induced by the diffusion process, and $n_o(\lambda)$ and $n_e(\lambda)$ are the bulk refractive indices. The relationships between the $C(x, y)$ and $\Delta n_{o,e}$ have been considered by several groups of researchers. It has been observed, for example, that the extraordinary index change Δn_e of Ti:LiNbO$_3$ waveguide at a fixed wavelength increases almost linearly with the titanium concentration $C(x, y)$, while the ordinary index change Δn_o only has a linear relationship with $C(x, y)$ for small values of $C(x, y)$, and becomes nonlinear at large values of $C(x, y)$ [16][17]. In order to make consistent between various models, the transverse profile (2.43) for the ordinary and extraordinary refractive indices of the $LiNbO_3$-based optical waveguides can be modified as follows,

$$\begin{aligned} n_o(x,y,\lambda) &= n_{ob}(\lambda) + \alpha_o \Delta n_o(C(x,y),\lambda) \\ n_e(x,y,\lambda) &= n_{eb}(\lambda) + \alpha_e \Delta n_e(C(x,y),\lambda) \end{aligned} \tag{2.44}$$

where α_o and α_e are adjustable fitting parameters to generalize the refractive index change. In general, the following empirical power-law relation between the species concentration and Δn_o, Δn_e has been used:

$$\Delta n_{o,e}(x,z,\lambda) = A_{o,e}(\lambda, C_s)[C(x,y)]^{\gamma_{o,e}} \tag{2.45}$$

where γ_o and γ_e are constants independent of x-axis and y-axis and C_S is the surface concentration. It is worth to note, for the optical waveguides based on the APE process, only the extraordinary refractive index is considered. In general, the above model can be simplified as follows [16],

$$\begin{aligned} \Delta n_o(x,y,\lambda) &= a_o r_o(C_o,\lambda)[\alpha_0(\lambda_r)C(x,y) + \delta n_o] \\ \Delta n_e(x,y,\lambda) &= a_e r_e(C_o,\lambda)\alpha_e(\lambda_r)C(x,y) \end{aligned} \tag{2.46}$$

where λ_r is the reference wavelength, $r_o(C_o,\lambda)$ and $r_e(C_o,\lambda)$ represent the relative wavelength dispersion of the species-induced refractive index changes. Furthermore, the model of (2.46) can be further simplified as a linear simplified model,

$$\begin{aligned} \Delta n_o(x,y,\lambda) &= a_o r_o(C_o,\lambda)\alpha_0(\lambda_r)C(x,y) \\ \Delta n_e(x,y,\lambda) &= a_e r_e(C_o,\lambda)\alpha_e(\lambda_r)C(x,y) \end{aligned} \tag{2.47}$$

where the index change is directly proportional to the species concentration. For Ti:$LiNbO_3$ waveguide, due to isotropic indiffusion, both ordinary and extraordinary refractive index changes Δn_o and Δn_e are positive and their maximal values are in a range of $10^{-2} \sim 10^{-3}$. On the other hand, for APE waveguide, due to nature of proton exchange, only extraordinary refractive index change Δn_e is positive and the diffused waveguide only supports one type of propagation modes (TE or TM). For examples, APE waveguides fabricated on *Z*-cut $LiNbO_3$ only support TM modes and APE waveguides fabricated on *X*-cut (or *Y*-cut) $LiNbO_3$ only support TE modes.

2.6 Summary

In this chapter, the general index models of bulk $LiNbO_3$ substrate and diffused $LiNbO_3$ waveguides due to titanium indiffusion and annealed proton exchange are described. The two-dimensional (2D) Fickian thermal diffusion equations related to the transverse section of optical waveguides are presented and their analytical and numerical solutions are given, which lay a solid foundation for the following chapters.

Chapter 3

Modal Properties of LiNbO$_3$ Optical Waveguides

After obtaining the refractive index distribution, the modal properties of the diffused waveguides are solely determined. In this chapter, the two-dimensional (2D) wave equations based on anisotropic media and its corresponding analytical and numerical solutions are described. Then the general simulation flow chat for mode solvers is presented and some modal properties such as modal profile and effective index are calculated. Finally, the effect of model parameters on the coupling loss (or overlap integral) with standard single mode fiber (SMF) are investigated.

3.1 Two Dimensional (2D) Wave Equation

Throughout this paper, a Cartesian coordinate system (x, y, z), as shown in Figure 3.1, and a time propagation dependence of $\exp[j(\omega t\text{-}k_z z)]$ are used, where ω is the angular frequency, k_z is the z component of the wave vector (i.e., $k_z = kn_{\text{eff}}$), and n_{eff} is the modal index or effective index. In general, the Maxwell's equations of the electric field ***E*** and magnetic field ***H*** in the frequency domain can be expressed as follows,

$$\begin{aligned} \nabla \times E &= -j\omega\mu_0 H \\ \nabla \times H &= j\omega\tilde{\varepsilon}_r\varepsilon_0 E \end{aligned} \tag{3.1}$$

where ε_0 and μ_0 are the permittivity and permeability of free space, respectively. The relative dielectric constant $\tilde{\varepsilon}_r = \tilde{n}^2$ is defined by (1.1) or has the following general form,

$$\tilde{\varepsilon}_r = \begin{pmatrix} n_{xx}^2 & n_{xy}^2 & 0 \\ n_{yx}^2 & n_{yy}^2 & 0 \\ 0 & 0 & n_{zz}^2 \end{pmatrix} \tag{3.2}$$

where n_{xx} (or n_x), n_{yy} (or n_y), n_{zz} (or n_z) are the refractive indices along x, y, z, respectively. n_{xy} and n_{yx} are the refractive indices due to the material anisotropy of the LiNbO$_3$ material. For the isotropic material, $n_{xx} = n_{yy} = n_{zz} = n$ and $n_{xy} = n_{yx} = 0$.

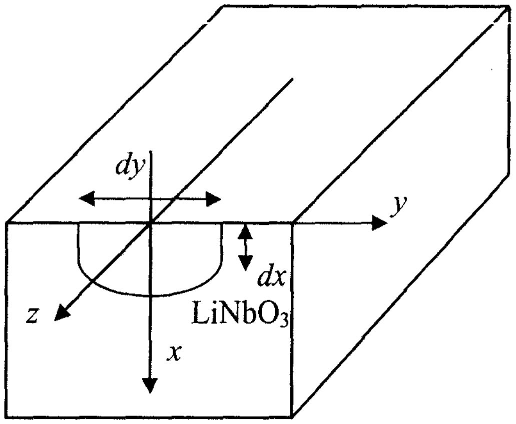

Figure 3.1 The Cartesian coordinate system of the diffused optic waveguide

By considering the uniform nature of the optical waveguide along z, the solutions of the above wave equations (or so-called the modal solutions) with the appropriate boundary conditions take the following forms for the electric field $\boldsymbol{E}$:

$$E = (\hat{x}E_x + \hat{y}E_y + \hat{z}E_z)e^{-jkn_{eff}z} \tag{3.3}$$

where k ($= 2\pi/\lambda$) is the propagation constant of free space and n_{eff} is the modal effective index at wavelength λ, and E_x/E_y and E_z are modal field patterns related to transverse and longitudinal components of the electric field $\boldsymbol{E}$, respectively. From the above equations, the full-vectorial wave equations for the transverse electric fields in anisotropic optical waveguides are directly deduced and expressed in simple matrix form [19],

$$\begin{pmatrix} P_{xx} & P_{xy} \\ P_{yx} & P_{yy} \end{pmatrix}\begin{pmatrix} E_x \\ E_y \end{pmatrix} = (kn_{eff})^2\begin{pmatrix} E_x \\ E_y \end{pmatrix} \tag{3.4}$$

where the operators are defined as:

$$P_{xx}E_x = n_{xx}^2k^2E_x + \frac{\partial}{\partial x}\left[\frac{1}{n_{zz}^2}\frac{\partial}{\partial x}\left(n_{xx}^2E_x\right)\right] + \frac{\partial^2E_x}{\partial y^2}$$

$$P_{yy}E_y = n_{yy}^2k^2E_y + \frac{\partial}{\partial y}\left[\frac{1}{n_{zz}^2}\frac{\partial}{\partial y}\left(n_{yy}^2E_y\right)\right] + \frac{\partial^2E_y}{\partial x^2}$$

$$P_{xy}E_y = n_{xy}^2k^2E_y + \frac{\partial}{\partial x}\left[\frac{1}{n_{zz}^2}\frac{\partial}{\partial y}\left(n_{yy}^2E_y\right)\right] - \frac{\partial^2 E_y}{\partial y \partial x}$$

$$P_{yx}E_x = n_{yx}^2k^2E_x + \frac{\partial}{\partial y}\left[\frac{1}{n_{zz}^2}\frac{\partial}{\partial x}\left(n_{xx}^2E_x\right)\right] - \frac{\partial^2 E_x}{\partial x \partial y}$$

where we note that the above full-vector wave equations are exact without any approximation and consider the polarization dependence and the polarization coupling, and both waveguide geometry and material anisotropy contribute to polarization coupling. If the polarization coupling is weak (i.e., the index difference is very small, $\sim 10^{-2}$) and become negligible as in many practical optical waveguides, such that $P_{xy} \approx P_{yx} \approx 0$, the above full-vector equations reduce to two decoupled semi-vector wave equations,

$$P_{xx,yy}E_{x,y} = \left(kn_{eff}\right)^2 E_{x,y} \qquad (3.5)$$

If the waveguide is weakly guiding, even the polarization dependence can be ignored (i.e., $P_{xx} \approx P_{yy}$). The wave equations of (3.5) are further reduced to a single well-known scalar Helmholtz wave equation,

$$\nabla_T{}^2 E_{x,y} + k^2n^2E_{x,y} = k^2 n_{eff}{}^2 E_{x,y} \qquad (3.6)$$

where ∇_T (i.e., $\hat{y}\partial/\partial y + \hat{x}\partial/\partial x$) is the transverse gradient operator.

For some of LiNbO$_3$-based waveguides, where the width of the strip is very large and the refractive index $n(x,y)$ is only the function of x, the semi-vector equations of (3.5) are further simplified to two decoupled one dimensional (1D) wave equations for the electrical fields,

$$P_{xx}E_x = n_{xx}^2k^2E_x + \frac{d}{dx}\left[\frac{1}{n_{zz}^2}\frac{d}{dx}\left(n_{xx}^2E_x\right)\right]$$

$$P_{yy}E_y = n_{yy}^2k^2E_y + \frac{d^2E_y}{dx^2} \qquad (3.7)$$

where $P_{xy} = P_{yx} = n_{xy} = n_{yx} = 0$ was used. These decoupled wave equations for the TE and TM modes can be solved through the field E_y and E_x, respectively. It is noted that the similar wave equations for magnetic fields H_x and H_y can be deduced and E_y/H_x and E_x/H_y for are governed by the same one dimensional (1D) wave equation.

Again, if the waveguide is weakly guiding, even the polarization dependence can be ignored. The wave equations of (3.6) are further reduced to a single well-known scalar Helmholtz wave equation:

$$\frac{d^2\Phi}{dx^2} + k^2(n^2 - n_{eff}^2)\Phi = 0 \tag{3.8}$$

where Φ is the scalar field (i.e., E_x, E_y, E_z, H_x, H_y, or H_z).

3.2 Analytical and Numerical Solutions

Based on the above theoretical formulas, by solving the governing equations for the transverse electric or magnetic fields under the full-vector or semi-vector/scalar assumptions for the 1D and 2D LiNbO$_3$ diffused waveguides, the dispersion curves of the optical waveguides can obtained. In general, LiNbO$_3$ diffused waveguides can be simulated by two kinds of methods: simple and intuitive analytical approaches (e.g., ray tracing and WKB method) and time-intensive rigorous numerical approaches (e.g., the finite difference method). For the 2D LiNbO$_3$ diffused waveguides, the analytical or approximate solutionss, although they gain some physical insight into LiNbO$_3$ diffused techniques, may only have for some specific structures. Due to their complicated index profiles, modal properties of the LiNbO$_3$ diffused waveguides can be calculated generally by employing accurate and versatile numerical methods. In this thesis, a rigorous and versatile finite difference method (FDM) [20] is utilized to solve the wave equations by employing popular perfectly matched layer (PML) boundary conditions [21].

3.2.1 Analytical solution

A graded index waveguides are usually fabricated by metal-diffusion (i.e., Ti) and ion-exchange (i.e., proton) techniques discussed previously. By utilizing some approximate methods such as the effective index method (EIM) for 2D index distribution of graded optical waveguides, the 1D equivalent graded index profile along the depth direction can be obtained. The modal properties of corresponding waveguides can be obtained by some well-known approximate approaches such as Wentzel-Kramers-Brillouin (WKB) method. Here we introduce the WKB method briefly.

The wave equation of (3.8) for the 1D graded index waveguide is rewritten with the electrical field $\Phi = H_y$ for TM mode and $\Phi = E_y$ for TE mode,

$$\begin{aligned} &\frac{d^2E_y}{dx^2} + k^2[n^2(x) - n_{eff}{}^2]E_y = 0 \\ &\frac{d^2H_y}{dx^2} + k^2[n^2(x) - n_{eff}{}^2]H_y = 0 \end{aligned} \tag{3.9}$$

where n_{eff} is the effective index of the mode.

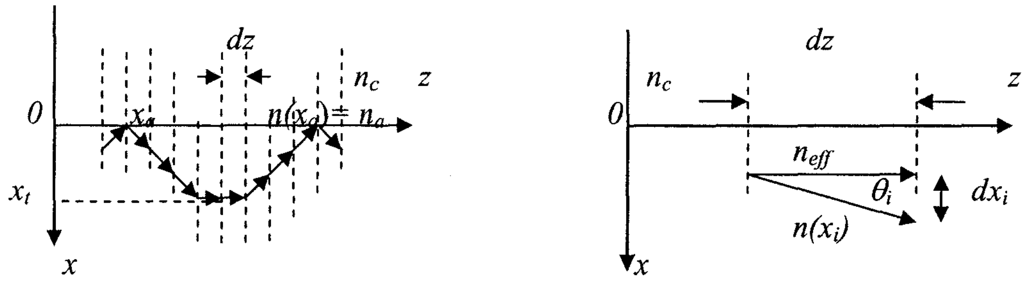

(a) Whole domain (b) The *i*th segment.

Figure 3.2 The ray-tracing picture of mode in 1D graded index waveguide: (a) whole domain, (b) the *i*th segment.

By dividing whole domain into small regions and utilizing the ray-approximation through small segment as shown in Figure 3.2, a ray trajectory of the mode in a graded index waveguide experiences a total internal reflection (TIR) at the guiding-cover interface ($x = x_a$) and curves through the guided region with a turning point ($x = x_t$). In the *i*th segment, the length dx_i along x is $dz\ tan(\theta_i)$ and the phase shift along x is $dx_i\ k_x(x_i)$, where $\theta_i = cos^{-1}(n_{eff} / n(x_i))$, $k_x(x_i) = k\sqrt{n^2(x_i) - n_{eff}{}^2}$, and $n(x_i)$ is a average value of index in the *i*th segment. When $n_{eff} = n(x_i)$ or $\theta_i = 0$, the ray trajectory turns back to the guided region. Similar to the step index waveguide, the phase matching condition for guided modes is that the total transverse phase shift of the round trip is an integer multiple of 2π,

$$2k\int_{x_t}^{x_a}\sqrt{n^2(x)-n_{eff}^{\,2}}\,dx = m2\pi + 2\phi_a + 2\phi_t \qquad (3.10)$$

where n_a is the peak surface index, $k_0 = 2\pi/\lambda$, $\phi_a = \tan^{-1}(r_a$ sqrt$[(n_{eff}^2(\mathrm{m})-n^2_c)/(n^2_a - n_{eff}{}^2(\mathrm{m}))])$ with $r_a = 1$ for TE modes and $r_a = (n_a/n_c)^2$ for TM modes, and $\phi_t = \pi/4$ if the variation of index at the turning point is sufficiently slow for both TE and TM modes. If we assume that $\phi_a = \pi/2$ for the guiding-cover interface and $\phi_t = \pi/4$ for the graded index region, we have

$$k\int_{x_t}^{x_a}\sqrt{n^2(x)-n_{eff}^{\,2}}\,dx = (m+\frac{2+p}{4})\pi$$

or

$$\int_{x_t}^{x_a}\sqrt{n^2(x)-n_{eff}^{\,2}}\,dx = (m+\frac{2+p}{4})\frac{\lambda}{2} \qquad (3.11)$$

where $m = 0, 1, 2, \ldots$ mode order and $p = 0$ for the double side (or symmetrical) diffused waveguide and $p = 1$ for single side diffused waveguide (i.e., one side with step index as shown in Figure 3.2). Because the index of $n(\mathrm{x})$ changes monotonically, the above equation in general can be solved numerically by trial and error. Once the mode order m (and p) is selected, a guess n_{eff} and x_a, x_t is made between n_a and n_s (suppose $n_s > n_c$), where n_s is the refractive index of the substrate. By comparing both sides of the equation of (3.11), the next possible n_{eff} is obtained. The process is repeated until convergence is obtained or no solution (i.e., cut-off) is found. For the modal profiles, the WKB method predicts the oscillatory field distribution in the guiding region where $n(\mathrm{x}) > n_{eff}$ and exponentially decaying fields where $n(\mathrm{x}) < n_{eff}$. For example, the modal profiles for the single-side diffused waveguide ($p = 1$) are following,

$$\begin{aligned}
E_y &= A\exp(\gamma_c x), \quad x < x_a \\
E_y &= \frac{B}{\sqrt{k_s(x)}}\cos(\frac{\pi}{4} - K(x)), \quad x_a < x < x_t \qquad (3.12)\\
E_y &= \frac{B}{2\sqrt{\gamma_s(x)}}\exp(-\Gamma_s(x)x), \quad x > x_t
\end{aligned}$$

where $k(x)=k\sqrt{n^2(x)-n_{eff}^2}$, $\gamma_c(x)=k\sqrt{n_{eff}^2-n_c^2}$, $\gamma_s(x)=k\sqrt{n_{eff}^2-n_s^2}$, $K(x)=\int_{x_t}^{x_a}k(x)dx$,

and $\Gamma(x)=\int_{x_B}^{x}\gamma_s(x)dx$.

3.2.2 Numerical solution

In this section, a rigorous and versatile finite difference method (FDM) [20] is utilized to solve the wave equations by employing popular perfectly matched layer (PML) boundary conditions [21]. Due to the simplicity and easy implementation, the FDM method is one of the most commonly used numerical methods for the boundary-value eigen-value problem. It is based on a semi-local approximation of the partial derivative through low-order Taylor series expansions. By employing the same formulas discussed in chapter 2, corresponding finite difference terms in the above wave equations can be obtained easily. Furthermore, all functions under the partial derivatives in the full-vector eigen-value equations of (3.4), (3.5), and (3.6) are continuous and they are directly discretized by using the central difference approximations without any extra treatment at the dielectric interface of the waveguide. For example, the finite difference expressions of wave equations of (3.4) for electric fields can be expressed as follows [22],

$$P_{xx}E_x=\frac{T_x^{i+1,j}E_x^{i+1,j}-T_x^{i,j}E_x^{i,j}+T_x^{i-1,j}E_x^{i-1,j}}{\Delta x^2}+n_{i,j}^2k^2E_x^{i,j}+\frac{E_x^{i,j+1}-2E_x^{i,j}+E_x^{i,j-1}}{\Delta y^2}$$

$$P_{yy}E_y=\frac{T_y^{i,j+1}E_y^{i,j+1}-T_y^{i,j}E_y^{i,j}+T_y^{i,j-1}E_y^{i,j-1}}{\Delta y^2}+n_{i,j}^2k^2E_y^{i,j}+\frac{E_y^{i+1,j}-2E_y^{i,j}+E_y^{i-1,j}}{\Delta x^2}$$

$$P_{xy}E_y=\frac{1}{4\Delta x\Delta y}\begin{bmatrix}\left(\dfrac{n_{i+1,j+1}^2}{n_{i+1,j}^2}-1\right)E_y^{i+1,j+1}-\left(\dfrac{n_{i+1,j-1}^2}{n_{i+1,j}^2}-1\right)E_y^{i+1,j-1}-\\ \left(\dfrac{n_{i-1,j+1}^2}{n_{i-1,j}^2}-1\right)E_y^{i-1,j+1}+\left(\dfrac{n_{i-1,j-1}^2}{n_{i-1,j}^2}-1\right)E_y^{i-1,j-1}\end{bmatrix}$$

$$P_{yx}E_x = \frac{1}{4\Delta x\Delta y}\begin{bmatrix} \left(\dfrac{n_{i+1,j+1}^2}{n_{i,j+1}^2}-1\right)E_x^{i+1,j+1} - \left(\dfrac{n_{i+1,j-1}^2}{n_{i,j+1}^2}-1\right)E_x^{i+1,j-1} - \\ \left(\dfrac{n_{i-1,j+1}^2}{n_{i,j-1}^2}-1\right)E_x^{i-1,j+1} + \left(\dfrac{n_{i-1,j-1}^2}{n_{i,j-1}^2}-1\right)E_x^{i-1,j-1} \end{bmatrix} \tag{3.13}$$

where

$$T_x^{i\pm1,j} = \frac{2n_{i\pm1,j}^2}{n_{i\pm1,j}^2+n_{i,j}^2},\quad T_y^{i,j\pm1} = \frac{2n_{i,j\pm1}^2}{n_{i,j\pm1}^2+n_{i,j}^2}$$

$$T_x^{i\pm1,j} = \frac{2n_{i,j}^2}{n_{i+1,j}^2+n_{i,j}^2}+\frac{2n_{i,j}^2}{n_{i-1,j}^2+n_{i,j}^2},\quad T_y^{i,j\pm1} = \frac{2n_{i,j}^2}{n_{i,j+1}^2+n_{i,j}^2}+\frac{2n_{i,j}^2}{n_{i,j-1}^2+n_{i,j}^2}$$

where the uniform meshes $\Delta x/\Delta y$, and isotropic index are used for the sake of simplicity.

In order to facilitate numerical solution within a finite computation domain, proper numerical boundary conditions must be used. In this work, we utilize the popular perfectly matched layer (PML) boundary conditions [21] at the edge of the computation window to reduce the computation effort without sacrifice for accuracy. By substituting the above finite difference expressions into the wave equation of (3.4), a system of the linear equations is obtained:

$$M\begin{bmatrix} E_x \\ E_y \end{bmatrix} = \left(kN_{eff}\right)^2\begin{bmatrix} E_x \\ E_y \end{bmatrix} \tag{3.14}$$

where k is the propagating constant in free space, N_{eff} is the complex modal effective index, and M is a band matrix with the bandwidth $(4N_x+6)$ and dimension $(2N_x\times N_y)$, in which N_x and N_y are the numbers of meshes in x and y directions. For the semi-vectorial and scalar cases, due to the decoupled wave equations, the band matrix M is simplified a matrix with the bandwidth $(2N_x+1)$ and dimension $N_x\times N_y$. The effective indices and mode profiles can be obtained by using some eigen-value solvers such as the shifted inverse power method, the Lanczos method, and the Arnoldi method.

3.2.3 Flow chat of simulation

Once modal profiles (i.e., electric fields Ex/Ey) and modal index (i.e., effective index n_{eff}) are solved, other modal properties of the $LiNbO_3$-based optical waveguides such as magnetic fields and confinement factor are readily obtained. Flow chat of simulation for $LiNbO_3$ optical waveguides is given in Figure 3.3.

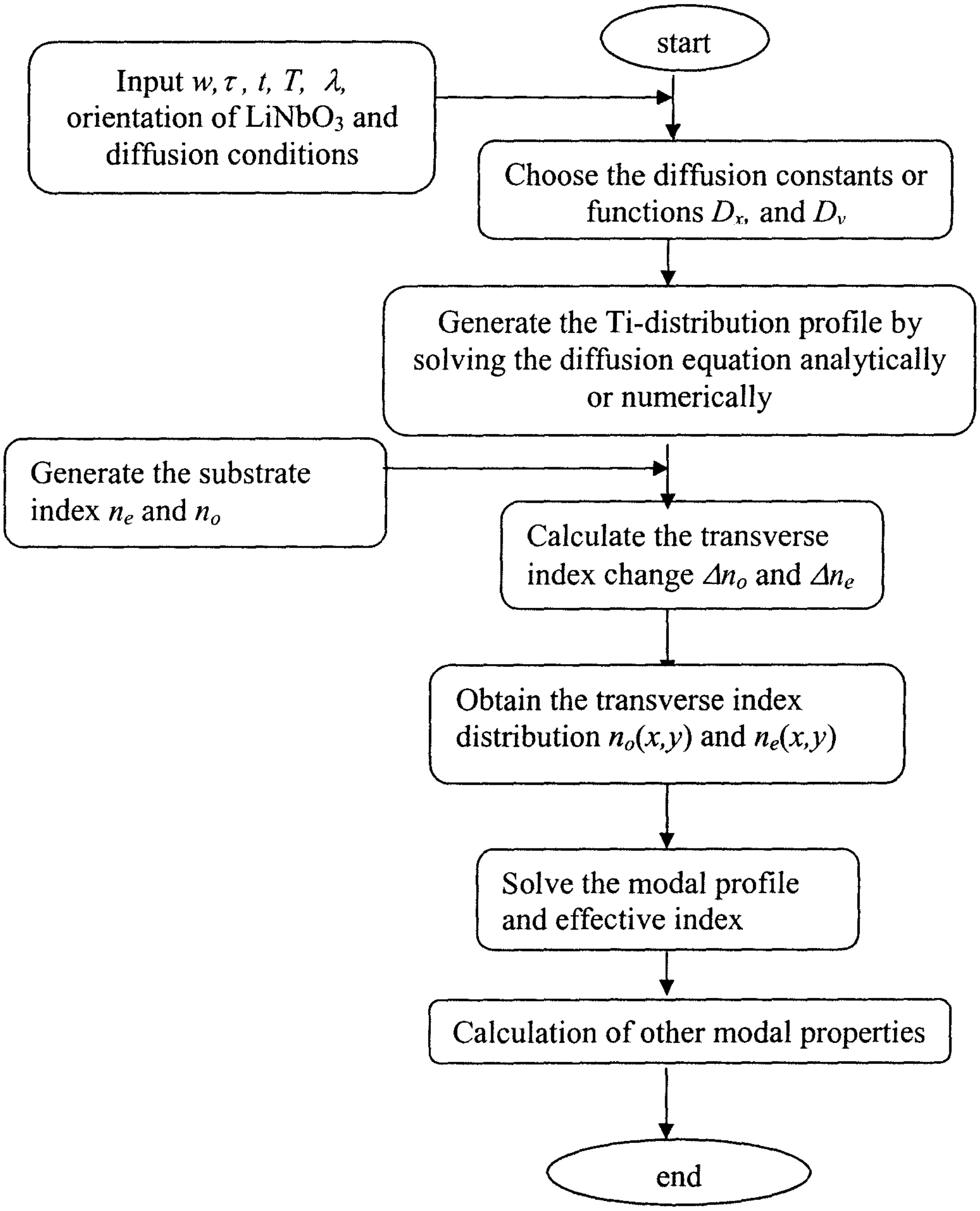

Figure 3.3 Flow chat of simulation for $LiNbO_3$ optical waveguides

3.3 Modal Properties of $LiNbO_3$ Optical Waveguides

In the following calculation, the optical waveguides based on Titanium in-diffusion are investigated, which have the following parameters: w = 7μm and τ = 90 nm with six hours Ti-ion diffusion at the temperature of 1050 °C. Figure 3.4 shows the calculated optical modal profile for both TE and TM modes. As predicted, the TM mode has stronger confinement than the TE mode. Once the effective index n_{eff} and mode profile $E(x)$ are obtained, other modal properties such as dispersion, confinement factor, mode effective area, and far-field with the relation of the design parameters can be obtained. For example, Figure 3.5 shows the effective indices of optical waveguide with a function of film width (a) and film thickness (b) of the Ti strip.

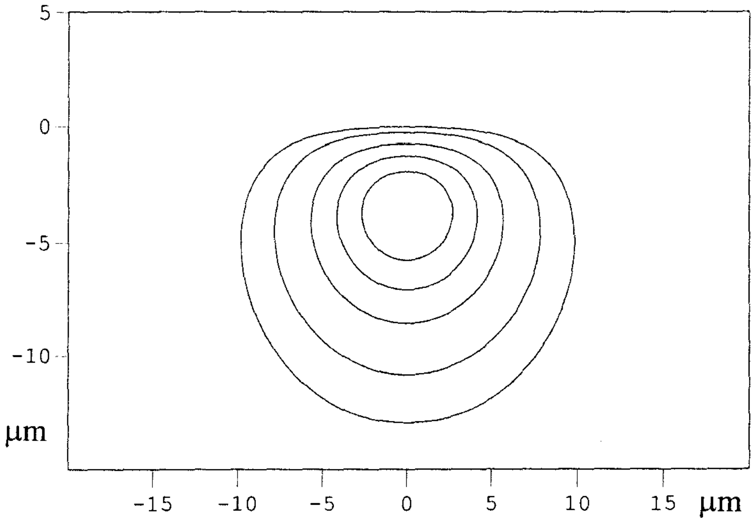

(a) TE mode

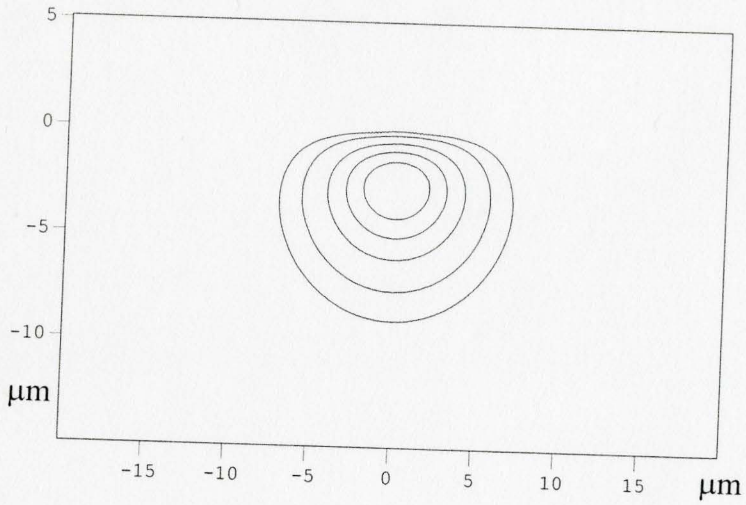

(b) TM mode,

Figure 3.4 Optical waveguide mode profiles: (a) TE mode, and (b) TM mode

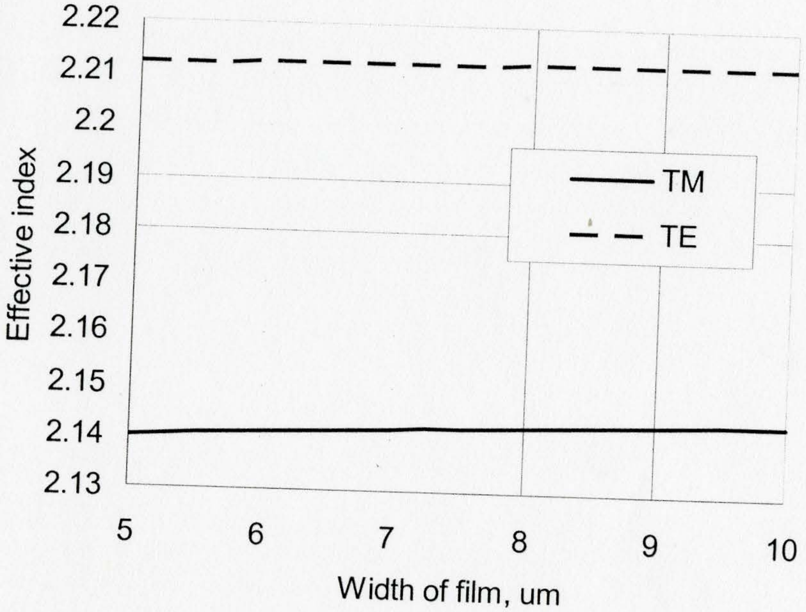

(a) A function of film width *w*

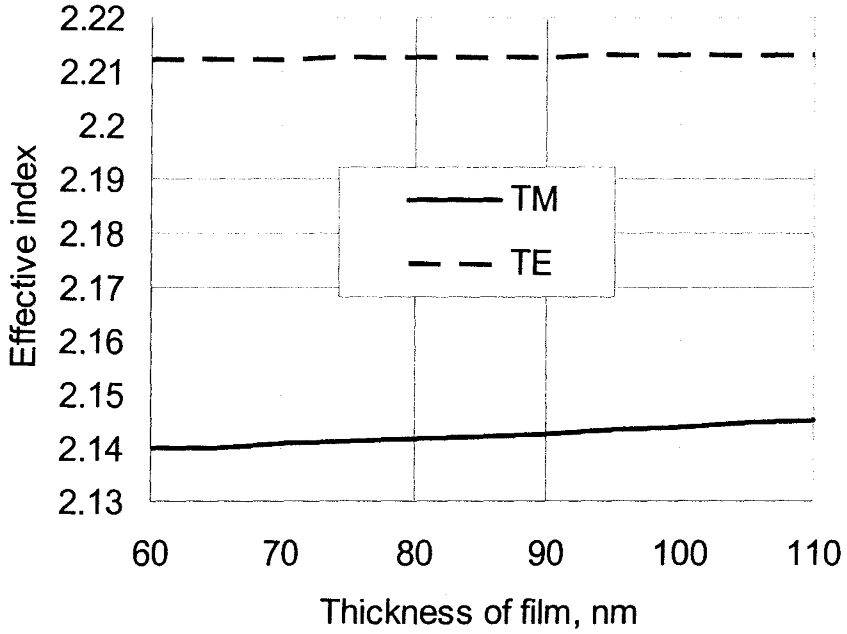

(b) A function of film thickness τ

Figure 3.5 Optical waveguide modal indices with a function of film width (a) and film thickness (b)

3.4 Coupling Loss

For the calculation of the coupling loss between the optical waveguide and standard SMF optical fiber, which is another important parameter in design of weakly-guided $LiNbO_3$-based optical waveguide, a overlap integral between two related modes can be utilized to calculate the coupling loss L_f,

$$L_f = \frac{1}{4}\int\left(E \times h^* + e^* \times H\right)\cdot \hat{z}dxdy \qquad (3.15)$$

where the superscript * represent a complex conjugate, ***E*** and ***H*** are modal profiles of the optical waveguide and ***e*** and ***h*** are modal profiles of the optical fiber.

Through the overlap integral of (3.15), the effects of the various parameters such as the buffer thickness, Ti-strip size, and diffusion conditions on the coupling loss can be investigated. Here the SMF optical fiber used has the following parameters: radius of 4.1 μm and $\Delta = 0.35\%$. In order to maintain the low coupling loss, the modal profile of the optical waveguide should have similar mode spot size (or mode field diameter) with one of the optical fiber. Figure 3.6 shows the coupling loss between the modal profiles of *Z*-cut LiNbO$_3$ waveguide and standard SMF fiber for different Ti-strip thickness and widths at a wavelength of 1.55 μm.

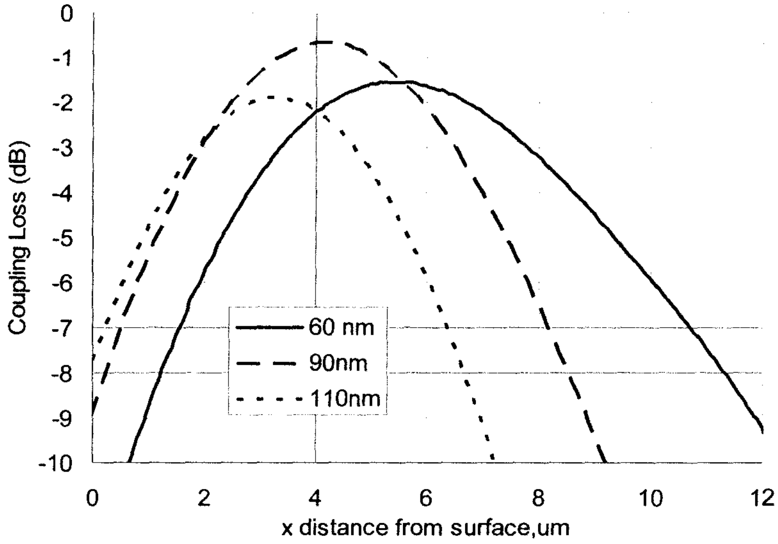

(a) Different Ti-strip thickness τ, TM

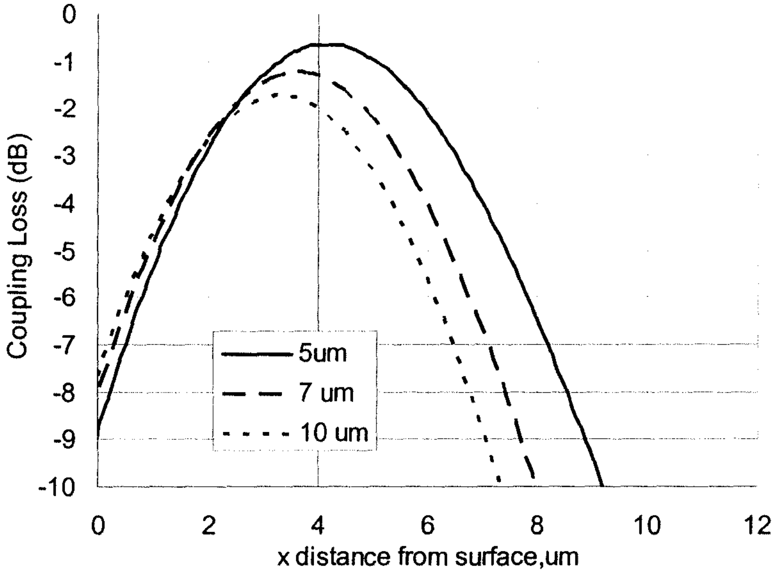

(b) Different Ti-strip width w, TM

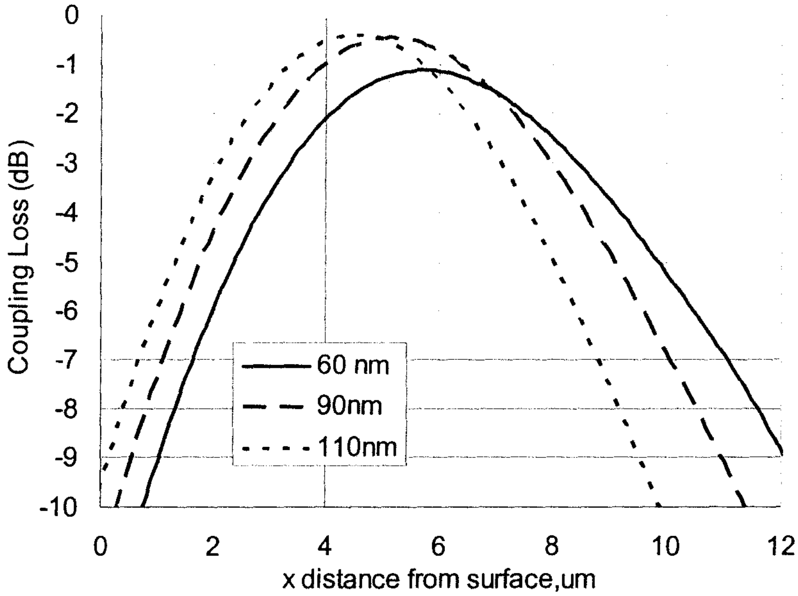

(c) Different Ti-strip thickness τ, TE

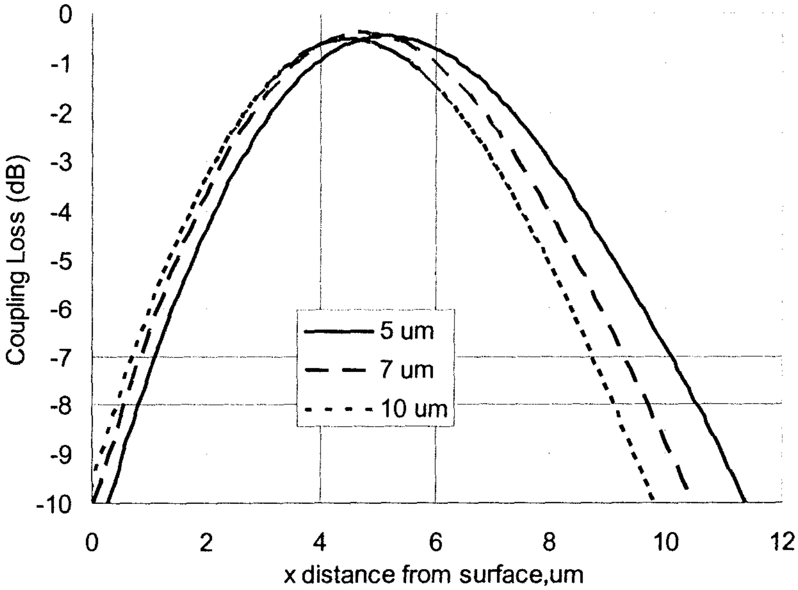

(d) Different Ti-strip width w, TE

Figure 3.6 Coupling loss between the Z-cut LiNbO$_3$ waveguide and standard SMF fiber as a function of vertical displacement from surface

3.5 Summary

In this chapter, by linking the relation of the design and fabrication parameters with modal properties of the $LiNbO_3$ waveguides, a comparative study on modeling and characterization of diffused optical waveguides is presented. Then, by applying a rigorous finite difference method, the modal properties of the diffused waveguides are solved and the modal properties are directly linked to some design and fabrication parameters (e.g., width and thickness of the strip film). Finally, some related issues such as the coupling loss with the standard fiber are discussed.

Chapter 4

Modeling and Design of Ti:LiNbO$_3$ Optical Waveguides

In this chapter, the material index, and model properties of Ti:LiNbO$_3$ optical waveguides are summarized and corresponding simulation flow chat is presented. Based on the modeling results, the corresponding Ti:LiNbO$_3$ optical waveguides were made in McMaster University.

4.1 Material Properties of Ti:LiNbO$_3$ Waveguides

Titanium indiffusion is one of the most widespread fabrication techniques for the LiNbO$_3$-based optical waveguides and the Ti:LiNbO$_3$-based optical waveguides have been intensively researched for more than four decades. Due to some unique features, such as easy fabrication, they are most widely used. In this technique, titanium and lithium within the diffusion region are exchanged and a graded-index distribution is realized during the thermal diffusion process. Since the indices within the diffusion region are usually slightly higher than those in the surrounding area, the weakly guided diffused waveguides are fabricated. The detailed fabrication process of Ti:LiNbO$_3$-based optical waveguides is described in Appendix B.

In general, the controlling parameters of the fabrication of Ti:LiNbO$_3$ waveguides are the width w and thickness τ of the deposited Ti-strip as shown in Figure 4.1. The diffusion process parameters of Ti:LiNbO$_3$ waveguides in the diffusion process are the followings: temperature T (around 1000°C), time t (about several hours), and ambient A (e.g., wet oxygen-like atmosphere or gas flow condition through a high temperature diffusion furnace).

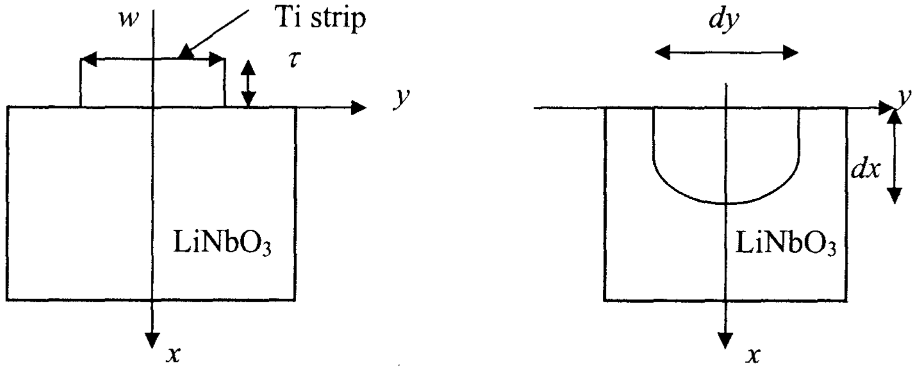

(a) Before diffusion (b) After diffusion

Figure 4.1 The schematic view of Ti:LiNbO$_3$ optical waveguides

As shown in Figure 4.1(a), the Ti-strip is sputtered on the bulk LiNbO$_3$ substrate (i. e., $-\tau < x < 0$, $-w/2 < y < w/2$). For the sake of simplicity, we assume that the Ti-strip is embedded in LiNbO$_3$ substrate (i. e., $0 < x < \tau$, $-w/2 < y < w/2$) and constant diffusion coefficients D_x and D_y are used. Hence the Ti-concentration distribution $C(x, y, t)$ can be obtained analytically by solving 2D Fickian diffusion equation as discussed previously [i. e., (2.30)],

$$C(x,y,t) = C_0 F(x)G(y);\ x \geq 0 \qquad (4.1)$$

and

$$F(x) = \frac{1}{2}[erf(\frac{\tau - x}{d_x}) + erf(\frac{\tau + x}{d_x})]$$

$$G(y) = \frac{1}{2}[erf(\frac{w/2 - y}{d_y}) + erf(\frac{w/2 + y}{d_y})]$$

where the error function $erf(y) = \frac{2}{\sqrt{\pi}}\int_0^y \exp(-u^2)du$ is used (see Appendix C), C_0 is the initial Ti-concentration, which can be derived from the law of conservation of the matter (see Appendix C). The parameters $d_x = 2\sqrt{D_x t}$ and $d_y = 2\sqrt{D_y t}$, as shown in Figure 4.1(b), are the diffusion lengths along the x-axis and the y-axis, respectively, for a diffusion time t. D_x and D_y are the diffusion coefficients are also called the bulk and surface diffusion constants, respectively. The surface Ti-concentration C_s is defined the concentration at the center of the waveguide surface and has a relation with initial Ti-concentration C_0: $C_s = C_0 erf(\tau/d_x) erf(w/2d_x)$. Overall, except the above-mentioned controlling parameters, the physical (or experimental) parameters required to be specified are the following fabrication parameters: C_0, D_x, and D_y, which depend on the crystal cut, temperature T, and environment A, and can be extracted from the experimental results.

For most of Ti:LiNbO3 optical waveguides with a thin thickness of the Ti-strip (i., e., $\tau << d_x$), as demonstrated by (2.32), the solution (4.1) can be simplified as follows [28] [29][31],

$$C(x,y,t) = C_0^{'} f(x) G(y); \; x \geq 0 \tag{4.2}$$

and

$$f(x) = F(x)/(\frac{2\tau}{d_x\sqrt{\pi}}) = \exp(-\frac{x^2}{d_x^2})$$

$$G(y) = \frac{1}{2}[erf(\frac{w/2-y}{d_y}) + erf(\frac{w/2+y}{d_y})]$$

where $C_0^{'} = 2\tau C_0/(d_x\sqrt{\pi})$ and the surface Ti-concentration $C_s = C_0^{'} erf[w/(2d_y)]$. By setting C_0 equal to one, $C_0^{'} = 2\tau/d_x\sqrt{\pi}$ is called the normalized initial coefficient.

For some cases of Ti-LiNbO3 optical waveguides with large width of the Ti-strip (i., e. $W >> d_y$), as demonstrated by (2.34), the solution (4.1) can be simplified,

$$C(x,y,t) = C_0 \; F(x) = C_s F(x)/erf(\tau/d_x) \tag{4.3}$$

and

$$F(x) = \frac{1}{2}[erf(\frac{\tau-x}{d_x}) + erf(\frac{\tau+x}{d_x})]$$

where the surface Ti-concentration $C_s = C_0 erf(\tau/d_x)$.

Finally, if Ti:LiNbO3 optical waveguides have large width and thin thickness of the Ti-strip, the solution (4.2) and (4.3) can be further simplified,

$$C(x, y, t) = C_0^{'} f(x); \qquad x \geq 0 \tag{4.4}$$

and

$$f(x) = F(x)/(\frac{2\tau}{d_x\sqrt{\pi}}) = \exp(-\frac{x^2}{d_x^2})$$

where the surface Ti-concentration $Cs = C_0^{'} = 2\tau/(d_x\sqrt{\pi}) \; C_0$.

Usually, the diffusion coefficients D_x and D_y are given approximately by an Arrhenius law [16],

$$D_i = D_0^i e^{-E_0^i/k_B T} = D_0^i e^{-T_0^i/T} \tag{4.5}$$

where D_0^i ($i = x$, y) is the diffusion constant, which is proportional to the jump distance and the jump frequency of the diffusion atoms in the crystal, and E_0^i(i. e.,kT_0^i , $i = x$, y) is the activation energy along i (i. e., x, y) direction in eV, which produced by the surrounding ions or atoms of the crystal. The constant k_B is the Boltzmann's constant and T is the diffusion temperature in Kevin (K). Some typical values of D_0^i, E_0^i, and T_0^i of *Z*-cut Ti:LiNbO$_3$ optical waveguides are presented in Table 4.1.

Table 4.1 Some typical values of diffusion constant and activation energy

Atmosphere	D_0^x, cm^2/s	D_0^x, μm^2/h	E_0^x, eV	T_0^x, K x10^{-4}	D_0^y, cm^2/s	D_0^y, μm^2/h	E_0^y, eV	T_0^y, K x10^{-4}
Dry air [29]	0.378	1.36x10^{11}	2.95	3.42	7.37x10^{-7}	2.65 x10^{5}	1.48	1.72
Dry Ar [16]	0.180	5.0x10^{9}	2.60	3.02	9.93x10^{-4}	1.35 x10^{8}	2.22	2.58

As mentioned previously, the surface Ti-concentration can be calculated as long as the initial Ti-concentration is given. For example, by choosing C_0 = 70.72 mass % [3] for the *Z*-cut LiNbO$_3$ waveguide, the surface Ti-concentration C_s in mass % can be calculated within ±6% of the experimental data [16] as shown in Table 4.2.

Table 4.2 The surface Ti-concentration for *Z*-cut LiNbO$_3$ waveguide

T(°C)	τ, μm	D_x, μm^2/hr	τ/d_x	C_s, sim. [3]	C_s, exp. [16]
1050	0.03	0.6232	0.0035	0.2793	0.29
1000	0.07	0.2544	0.0080	0.6384	0.60
1000	0.07	0.2544	0.0093	0.7421	0.80
1000	0.15	0.2544	0.0200	1.5958	1.49
1000	0.15	0.2544	0.0243	1.9387	1.95
1050	0.185	0.6232	0.0150	1.1969	1.22
1000	0.200	0.2544	0.0243	1.9387	1.89

Once the initial conditions and corresponding parameters of the diffusion process are given, by using some analytical and numerical approaches, the diffusion equation with the different diffusion functions and boundary conditions can be easily solved. For example, by using the following parameters [3][30]: w = 10 μm, τ = 0.05 μm, t = 6 hrs,

T = 1050°, λ =1.55 μm, A = dry air, and C_0 =70.72%, D_x = 0.792 μm^2/hrs, D_y = 0.504 μm^2/hrs for Z-cut and C_0 = 53.33%, D_x = 0.504 μm^2/hrs, D_y = 10.8 μm^2/hrs for Y-cut Ti:LiNbO$_3$ waveguide, where D_x and D_y are calculated by (4.5) with D_0 = 3.47x10^{-2}, 2.50 x10^{-5} cm^2/s and E = 2.45, 1.54 eV for Y-cut waveguide [30]. The corresponding Ti-concentration distributions with a function of x and y of Y-cut and Z-cut Ti:LiNbO$_3$ waveguides are shown in Figure 4.2. Also some parametric study can be realized naturally. For example, for the Z-cut Ti:LiNbO$_3$ waveguide with following parameters [3][30]: w = 10 μm, τ = 0.05 μm, t = 6 hrs, T = 1050°, λ =1.55 μm, A = wet air, and C_0 =70.72%, D_x = 0.792 μm^2/hrs, D_y = 0.504 μm^2/hrs for Z-cut, the corresponding Ti-concentration distributions with a function of x and y are shown in Figure 4.3.

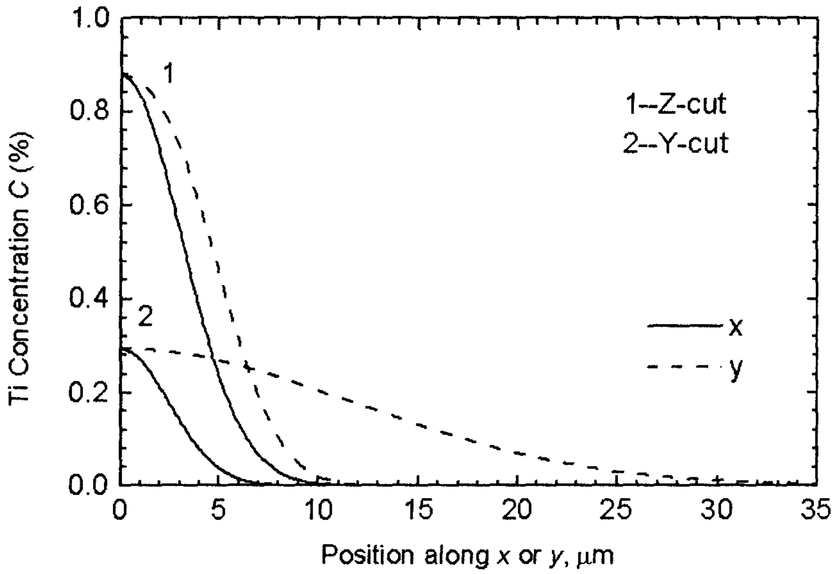

Figure 4.2 Ti-concentration distribution with a function of x and y of Y-cut and Z-cut Ti:LiNbO$_3$ waveguide with following parameters: width of metal 10 μm, thickness of metal 0.05 μm, diffusion time 6hrs, diffusion temperature 1050 °C, C_0 =53.33% or 70.72% at dry air ambient.

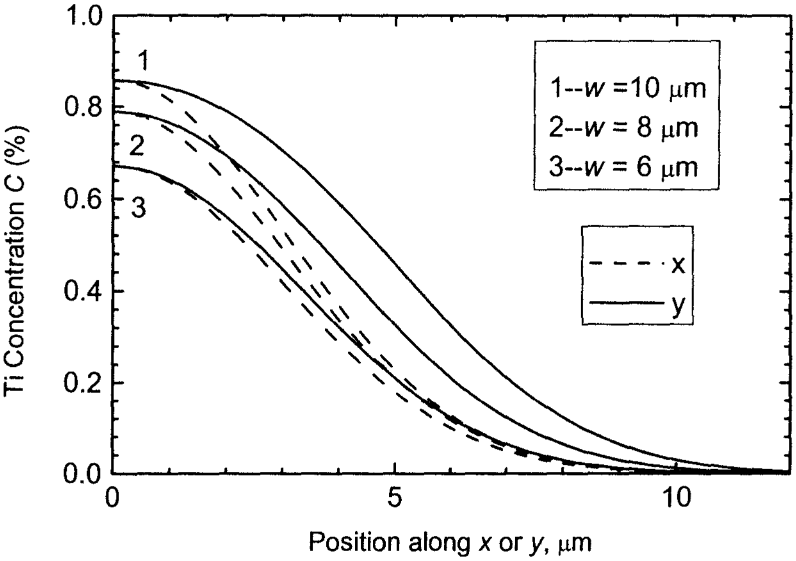

(a) Different width w of the Ti-strip

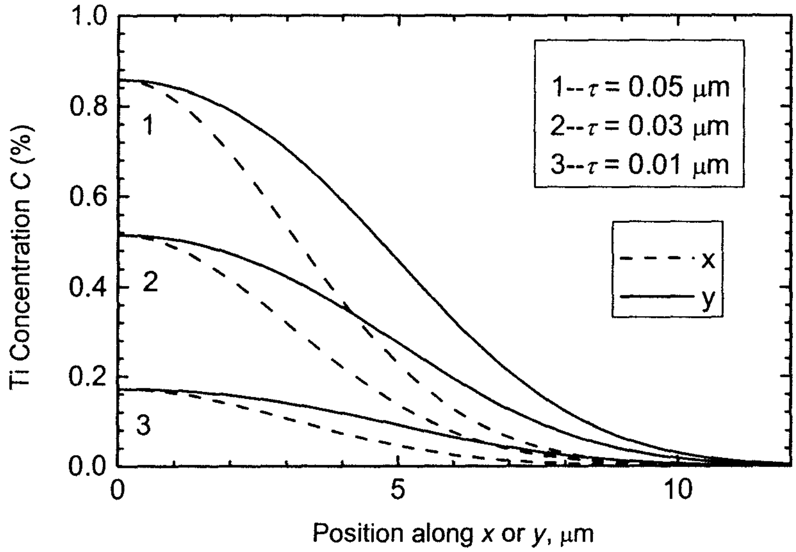

(b) Different thickness τ of the Ti-strip

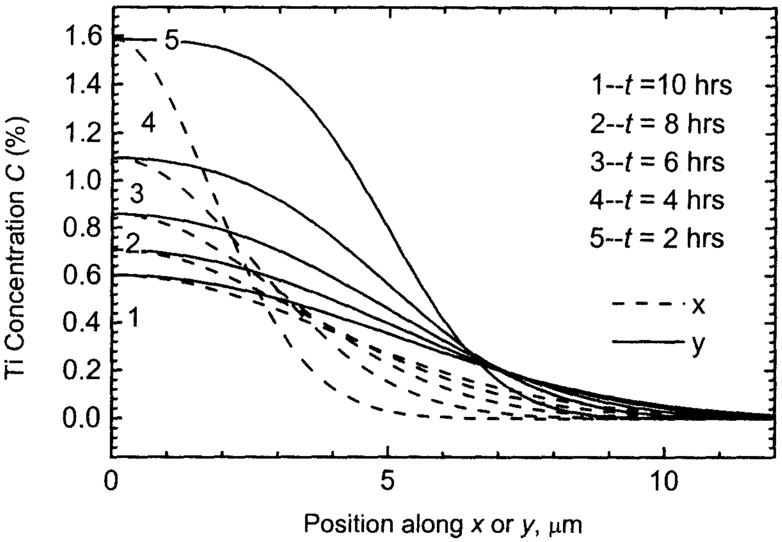

(c) Different diffusion time t

Figure 4.3 Ti-concentration distribution with a function of x and y of Z-cut Ti:LiNbO$_3$ waveguide with following parameters: width of metal 10 μm, thickness of metal 0.05 μm, diffusion time 6hrs, diffusion temperature 1050 °C, C_0 =70.72% at wet O_2 ambient.

In most cases of Ti:LiNbO$_3$ waveguides, the analytical solution of the diffusion equation agrees well with the numerical solution. However, for some cases of Ti:LiNbO$_3$ waveguides, the analytical solution of (2.32) may not be accurate enough. For example, by considering the fact that the diffusion coefficient is much larger close to the surface due to the nature of the activation energy, the diffusion coefficient D becomes depth dependent [24],

$$D(x)=D_0\,[1+A exp(-x/x_0)];\ x\geq 0 \qquad (4.6)$$

where $D(x)$ can be further approximately if $A \gg 1$ and x_0 is small,

$$D(x) = D_1 = D_0\,[1+A];\ x_0 > x \geq 0$$

$$D(x) = D_2 = D_0\,; \qquad x_{max} > x \geq x_0 \qquad (4.7)$$

where $D(x)$ is a step-like function ($D_1 \gg D_2$). The Ti-concentration distribution $C(x,y,t)$ can be obtained by solving the diffusion equation numerically. Figure 4.4 shows the Ti-concentration distributions with different Ti-strip widths at following parameters: t = 100 hrs, T = 1000 °C, C_0 =53.33mass % [26].

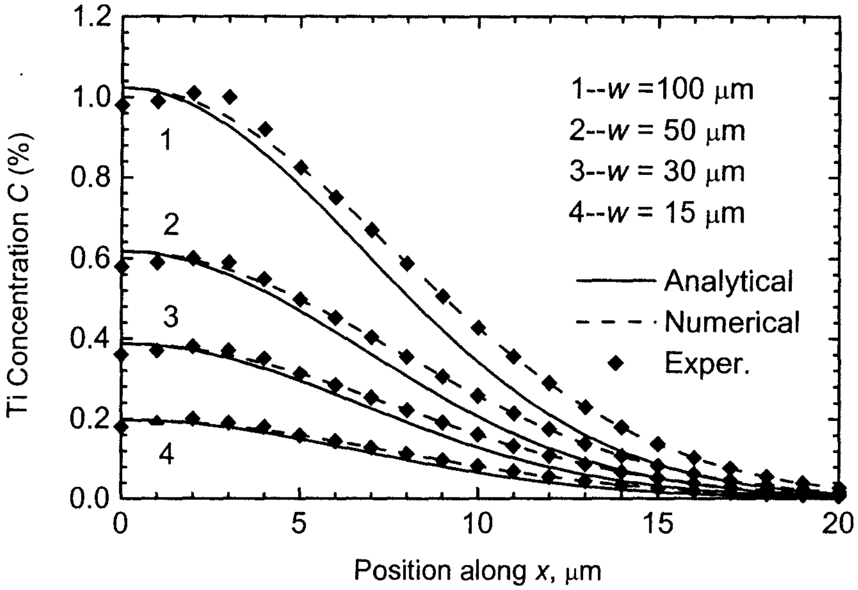

Figure 4.4 Ti-concentration distributions of Ti:LiNbO$_3$ waveguide for different Ti-strip widths

4.2 Index Properties of Ti:LiNbO$_3$ Waveguides

After obtaining the Ti-concentration distribution, the transverse profile for the extraordinary refractive indices of the Ti-indifussion process can be rewritten from (2.44),

$$\begin{aligned} n_o(x,y,\lambda) &= n_{ob} + \alpha_o \Delta n_o(C(x,y),\lambda) \\ n_e(x,y,\lambda) &= n_{eb} + \alpha_e \Delta n_e(C(x,y),\lambda) \end{aligned} \tag{4.8}$$

where α_o and α_e are adjustable fitting parameters to generalize the refractive index change. The relationships between the $C(x,y)$ and $\Delta n_{o,e}$ have been considered by several groups of searchers and are not consistent. For Ti:LiNbO$_3$ waveguide, it has been observed that the extraordinary index change Δn_e at a fixed wavelength increases almost linearly with the titanium concentration, while the ordinary index change Δn_o does not. By adding an offset index δn_o for the ordinary index, the index changes of the ordinary and extraordinary refractive indices can be expressed simply as a linear function of (2.46)[16] [26] (*Model* 1),

$$\begin{aligned} \Delta n_o(x,y,\lambda) &= r_o(C_s,\lambda)[\alpha_0(\lambda_r)C(x,y)+\delta n_o] \\ \Delta n_e(x,y,\lambda) &= r_e(C_s,\lambda)\alpha_e(\lambda_r)C(x,y) \end{aligned} \tag{4.9}$$

where λ_r = 0.6328 μm is the reference wavelength, C_s is the surface Ti concentration, $r_o(C_s,\lambda)$ and $r_e(C_s,\lambda)$ represent the relative wavelength dispersion of the Ti-induced refractive index changes. In order to accomplish the differences between research groups due to their own sample preparation, fabrication, and calibration procedures, the adjustable parameters $a_0(\lambda_r)$ and $a_e(\lambda_r)$ are introduced, which are in the vicinity of unity and can be obtained by fitting calculations to the measurement results. At the reference wavelength of λ_r = 0.6328 μm, $\alpha_e = dn_e/dc$ is approximately a constant and the values of $\alpha_o = dn_o/dc$ and δn_o change as Ti-concentration C (mol %). Table 4.3 shows some typical values of α_o, α_e, and δn_o change as Ti-concentration C (mol %).

Table 4.3 Typical values of α_o, α_e, and δn_o change as Ti-concentration C (mol %)

Year/Ref	$\alpha_o/\delta n_o$, $0<C<0.5$	$\alpha_o/\delta n_o$,$0.5<C<1.1$	$\alpha_o/\delta n_o$, $C>1.1$	α_e	Note
1989 [26]	0.85/0	0.65/0.0001	0.35/0.00043	0.76	
1984 [31]	0.65/0	0.65/0	N/A	0.65	r_o=r_e*
1983 [32]	0.89/0	0.47/0	0.32	0.764	

Note: * $r = r_o = r_e$= 0.86344 - 0.06193/λ^2 + 0.06393/λ^4 – 0.00690/λ^6.

By further considering nonlinear relationship between titanium concentration $C(x,y)$ and the ordinary index change Δn_o, the ordinary and extraordinary index changes Δn_o, Δn_e at a wavelength of λ have the following form [25][27] (*Model* 2),

$$\begin{aligned} \Delta n_o(x,y,\lambda) &= r_o(\lambda)[\alpha_0(\lambda_r)C(x,y)]^\gamma \\ \Delta n_e(x,y,\lambda) &= r_e(\lambda)\alpha_e(\lambda_r)C(x,y) \end{aligned} \tag{4.10}$$

where $r_o(\lambda)$ and $r_e(\lambda)$ represent the relative wavelength dispersion of the Ti-induced refractive index changes. The adjustable fitting parameters have the following values: $\alpha_0(\lambda_r) = 6.5\text{x}10^{-5}$ (or $1.3\text{x}10^{-25}$ cm^3), $\alpha_e(\lambda_r) = 6.0\text{x}10^{-3}$ (or $1.2\text{x}10^{-23}$ cm^3), and $\gamma = 0.55$ at the reference wavelength of λ_r = 0.6328 μm, which are extracted from the experimental data for the *Y*-cut Ti:LiNbO$_3$ waveguide [26]. The wavelength dispersion terms $r_o(\lambda)$ and $r_e(\lambda)$ are adopted [25],

$$\begin{aligned} r_o(\lambda) &= 0.67\lambda^2/(\lambda^2-0.13) \\ r_e(\lambda) &= 0.839\lambda^2/(\lambda^2-0.0645) \end{aligned} \qquad (4.11)$$

where λ is the wavelength in micrometers (μm) with $r_o(\lambda_r) = 0.992$ and $r_e(\lambda_r) = 1.0$.

In general, the following empirical power-law relation between the Ti-concentration and index changes Δn_o, Δn_e has been used [3][16] (*Model* 3):

$$\Delta n_{o,e}(x,y,\lambda) = A_{o,e}(\lambda, C_s)[C(x,y)]^{\gamma_{o,e}} \qquad (4.12)$$

where γ_o and γ_e are constants independent of *x*-axis and *y*-axis and C_S is the surface concentration, and

$$A_{o,e}(\lambda, C_s) = \left[\frac{2C_0}{\sqrt{\pi}}\right]^{-\gamma_{o,e}} [B'_{o,e}(\lambda) + \{B''_{o,e}(\lambda)\frac{\sqrt{\pi}}{2C_0}\}C_s] \qquad (4.13)$$

with the wavelength dispersion of $B'_{o,e}(\lambda)$ and $B''_{o,e}(\lambda)$ in the range $0.6 \le \lambda\ (\mu m) \le 1.6$ can be approximated by the following polynomials [3][16],

$$B'_o = 0.0653 - 0.0315\lambda + 0.00709\lambda^2$$

$$B''_o = 0.478 + 0.464\lambda - 0.0348\lambda^2$$

$$B'_e = 0.385 - 0.430\lambda + 0.171\lambda^2$$

$$B''_e = 9.13 + 3.85\lambda - 2.49\lambda^2$$

C_0 =70.72 mass %, $\gamma_o = 0.500$, and $\gamma_e = 0.765$ for the *Z*-cut LiNbO3.

C_0 =53.33 mass % $\gamma_o = 0.561$, and $\gamma_e = 0.877$ for the *Y*-cut LiNbO3.

$$C_s = erf\left(\frac{w}{2\sqrt{D_x t}}\right) erf\left(\frac{\tau}{2\sqrt{D_y t}}\right) C_0$$

By using the above formula, it is found that the lateral profile is about two-and-half broader for the *Y*-cut waveguide than the *Z*-cut waveguide, and the surface Ti-concentration C_S in the *Y*-cut waveguide is less than that of *Z*-cut waveguide by the same amount. It is worth to note that C_0 is the Ti initial concentration of the Ti strip ($-\tau \le x \le 0$) in LiNbO$_3$ waveguide at $t = 0$. Usually C_0 is dependent on the diffusion temperature on the ambient condition (the sputtering technique and the crystal cut). Since it is a complicated procedure from the diffusion temperature and ambient condition to get Ti initial concentration C_0, usually C_0 is extracted from experimental concentration profiles. For examples, for certain diffusion temperature and ambient condition, the values of C_0 have been found to be 53.33 mass % for *Y*-cut $LiNbO_3$ waveguide and 70.72 mass% for *Z*-cut waveguides [3].

By following formulas of (4.8) to (4.13), the index distribution of *Z*-cut Ti:$LiNbO_3$ can be obtained as shown in Figure 4.5 with the following parameters [3]: $\lambda =$ 0. 6238 μm, $C_0 = 70.72$ mass%, $w = 10$ μm, $\tau = 0.06$ μm, $T = 1050$ °C, $t = 6$ hrs at wet O_2 ambient ($\alpha_o = 0.500$, $\alpha_e = 0.810$, $B'_o = 0.048$, $B''_o = 0.632$, $B'_e = 0.191$, $B''_e = 10.53$). By comparing refractive indices with experimental results, it is found that the Model 3 of the index change due to diffusion agrees well with the experimental data. It is also found that the index difference of the extraordinary index is larger than one of the ordinary index. Thus, for the *Z*-cut waveguide, the TM mode will be more strongly confined in the waveguide than the TE mode, which is in agreement with the experimental results [3]. It is interesting to note that, for *Z*-cut Ti:$LiNbO_3$ waveguide, there is a fixed point C_{eo} of the Ti concentration with $\Delta n_o = \Delta n_e$, in which $\Delta n_o > \Delta n_e$ if $C < C_{eo}$, and $\Delta n_o < \Delta n_e$ if $C > C_{eo}$.

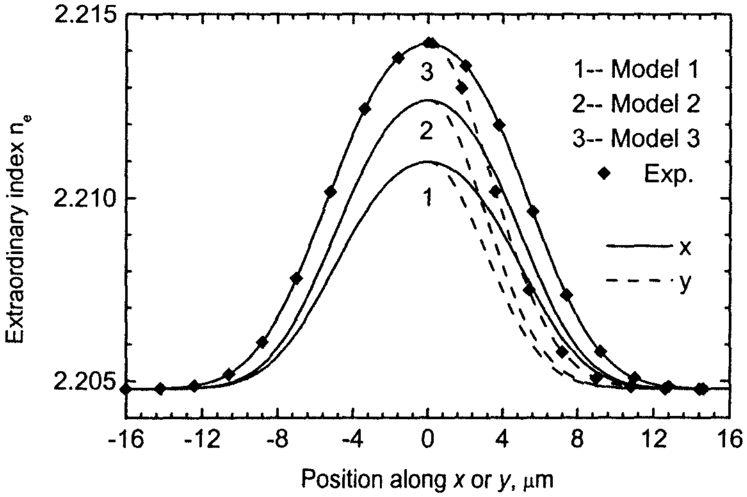

(a) The ordinary and extraordinary refractive index n_e

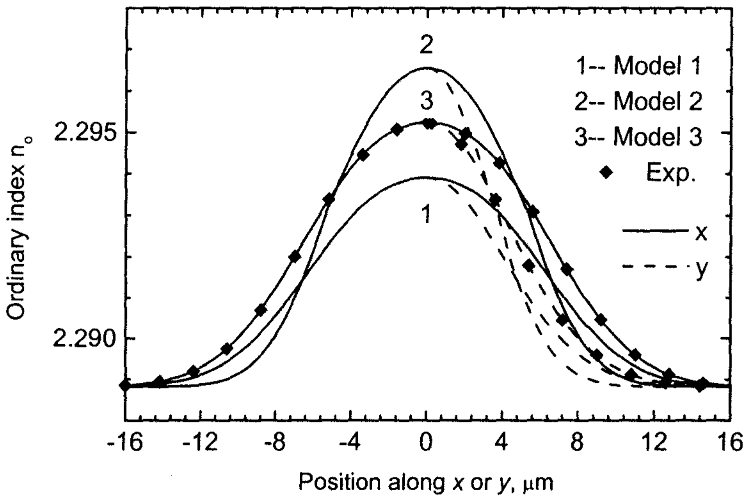

(b) The ordinary refractive index n_o

Figure 4.5 Index distribution of Z-cut LiNbO$_3$ waveguide

4.3 Modal Properties of Ti:LiNbO$_3$ Waveguides

After getting the index distribution of the Ti:LiNbO$_3$ optical waveguides, the modal properties are readily solved by the methods discussed in Chapter 3. The overall simulation flow chat of Ti:LiNbO$_3$ waveguides involving material and modal properties is shown in Figure 4.6. Once modal profiles (i.e., electric fields Ex/Ey) and modal index (i.e., effective index n_{eff}) are solved, other modal properties of the LiNbO$_3$-based optical waveguides such as magnetic fields, bending loss, coupling loss with the standard single mode fiber, and confinement factor are easily obtained. In our current work, the Z-cut Ti:LiNbO3 waveguides with T = 1050°C, τ = 0.11 μm, w = 6.0 -10.0 μm, t =3, 4 hrs are used. Figure 4.7 shows typical electric fields Ex and Ey of TM and TE modes with the mesh size $\Delta x = \Delta y = 0.1$ μm. Table 4.4 show the corresponding effective indices of Z-cut Ti:LiNbO3 waveguide at T=1050°C, t = 4 hrs, τ=0.11 μm and w = 8, 9, 10 μm.

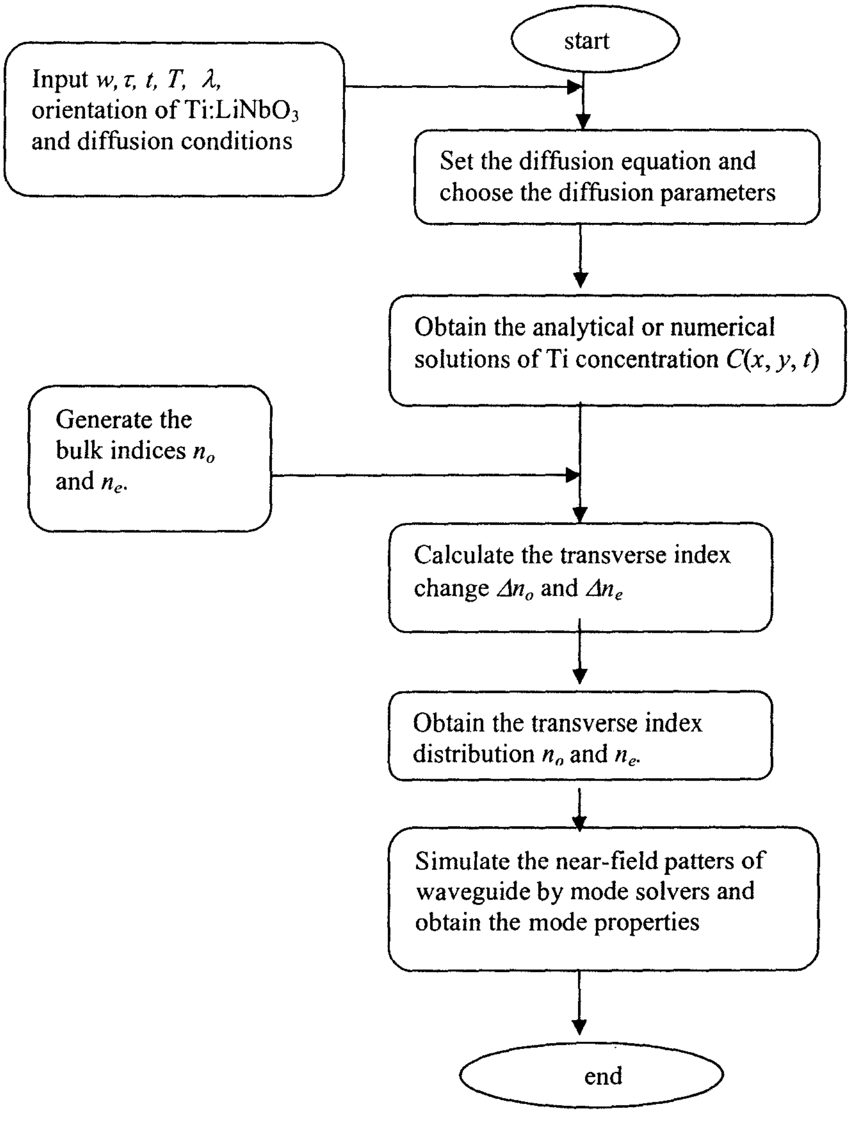

Figure 4.6 Schematic diagram of simulation of Ti:LiNbO$_3$ index profile

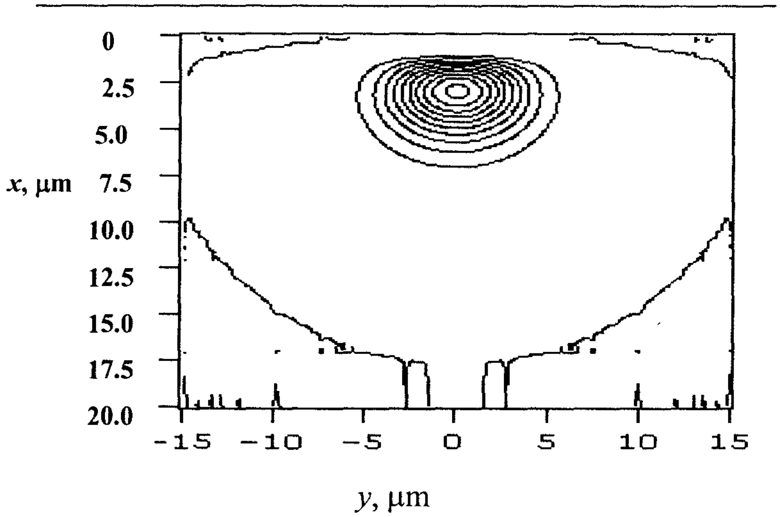

(a) *E*x of t TM mode (contour level: 0.5 from 0 to 5.0)

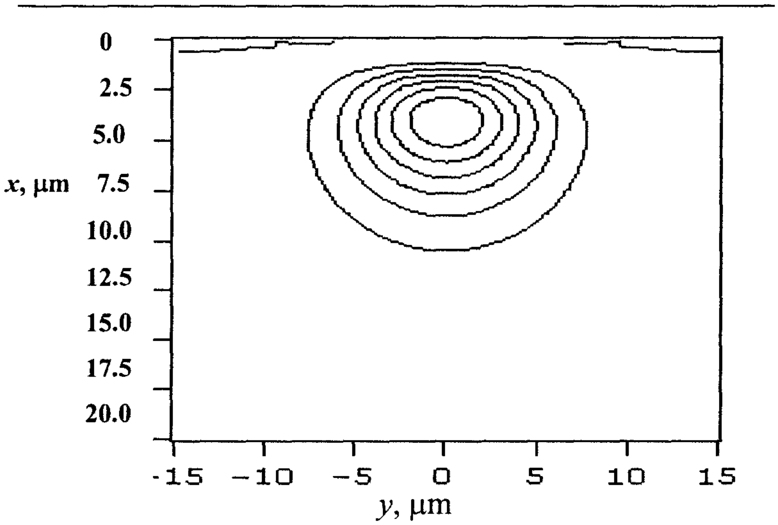

(b) *E*y of TE mode (contour level: 0.5 from 0 to 3.2)

Figure 4.7 Electric fields of *Z*-cut Ti:LiNbO3 waveguide at T = 1050°C, τ = 0.11 μm, w = 9.0 μm, and t = 4 hrs: (a) *E*x of TM mode and (b) *Ey* of TE mode.

Table 4.4 Effective indices of *Z*-cut Ti:LiNbO3 waveguide at T=1050°C, t = 4 hrs

w, μm	τ, μm	n_{TE}	n_{TM}
8	0.11	2.21295	2.14702
9	0.11	2.21313	2.14797
10	0.11	2.21328	2.14868

4.4 Design and Fabrication of Ti:LiNbO$_3$ optical waveguides

In order to verify the model and gain some physical insight of guiding waveguides, some *Z*-cut Ti:LiNbO$_3$ waveguides are fabricated in McMaster University. Here we describe design, fabrication, and measurement results of the Ti:LiNbO$_3$ waveguides.

4.4.1 Design of *Z*-cut Ti:LiNbO$_3$ waveguides

Once the relationship between the modal properties and process parameters is built, it is ready to design the Ti:LiNbO$_3$ waveguides. For the sake of simplicity, the *Z*-cut Ti:LiNbO$_3$ waveguides are selected. By following the simulation procedure as shown in Figure 4.6, the modal fields of the *Z*-cut Ti:LiNbO$_3$ waveguides with different Ti-strip dimensions and fabrication conditions can be calculated. Table 4.5 shows some typical fabrication conditions of the *Z*-cut Ti:LiNbO$_3$ waveguides.

Table 4.5 Fabrication conditions of current work and other published examples of *Z*-cut Ti:LiNbO$_3$ waveguide.

Year[Ref]	Wavelength, λ(μm)	Ti thickness, τ (μm)	Diffusion temperature, T(°C)	Diffusion time, t(h)	note
Current work	1.55, 0.633	0.11	1050	3,4	w = 6-10μm
1974 [23]	0.633	0.05	960	6	
1978 [29]	0.633	0.04	950-1050	5	
1979 [27]	1.15	0.05	1000	10	
1980 [30]	1.15	0.05	1000,1030,1050	5	Dry air
1987[16]	0.633-1.523	0.03-0.21	1000-1050	9	Dry O$_2$ /Ar

4.4.2 Fabrication of *Z*-cut Ti:LiNbO$_3$ waveguides

By using the same Ti-strip patterns, the several optical waveguides under different diffusion conditions are fabricated. Figure 4.8 shows the Ti Patterns before thermal diffusion. Figure 4.9 and Figure 4.10 show Ti patterns after thermal diffusion with thermal diffusion condition: $T = 1050$°C, $t = 4$ hours.

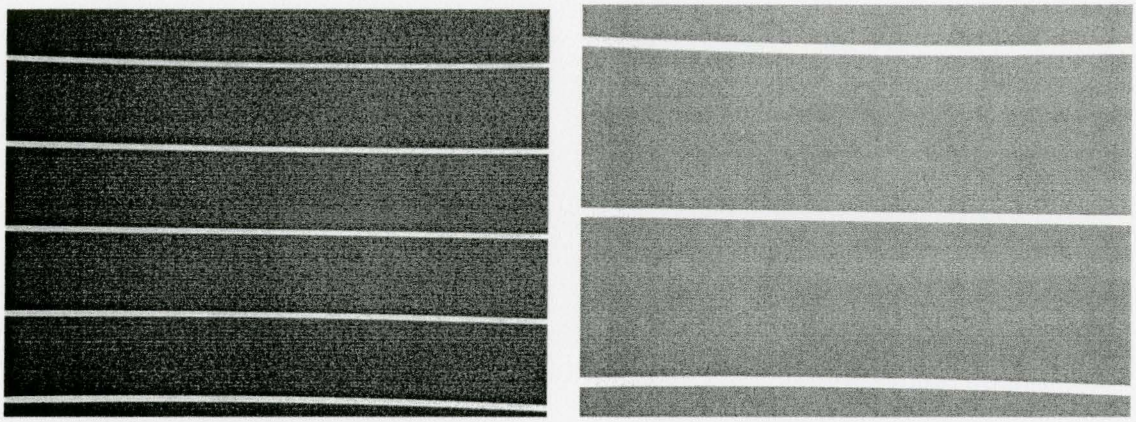

(a) X100 (a) X1000

Figure 4.8 Ti Patterns before thermal diffusion

(a) X100

Figure 4.9 Ti patterns after thermal diffusion with thermal diffusion condition: $T = 1050$°C, $t = 4$ hours, atmosphere: argon and oxygen flow

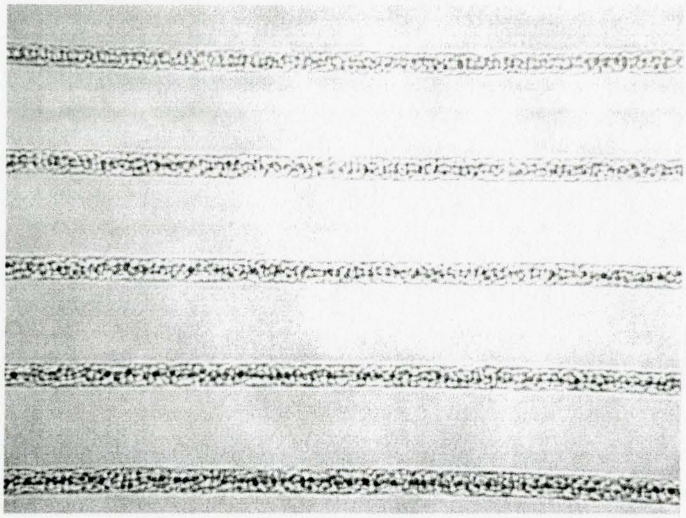

(a) X100

Figure 4.10 Ti Patterns after thermal diffusion with thermal diffusion condition: $T = 1050$ ° C, $t = 4$ hours, atmosphere: airflow

From Figure 4.8 to Figure 4.10, it is found that the diffusion atmosphere is crucial for manufacturing the Ti-indiffusion optical waveguides. It is observed that, in airflow ambient, there exists severe Li-outdiffusion and waveguides fabricated suffers high loss. On the other hand, in argon and oxygen flow ambient, there exists little Li-outdiffusion and waveguides fabricated have low loss.

4.4.3 Measurements of Z-cut Ti:LiNbO$_3$ waveguides

The experimental setup for measuring near-field pattern is shown in Figure 4.11. In this setup, an amplified spontaneous emission broad band source (BBS) with 1.55 μm central wavelength and an attenuator for controlling the source power are utilized. The connection between the single mode fiber and Ti:LiNbO$_3$ waveguide is through butt coupling. The output near-field pattern of Ti:LiNbO$_3$ waveguide is amplified by a 10X objective lens with a numerical aperture of 0.25 and captured by an Infrared camera. The measurement results of the Infrared camera are collected and analyzed through a video grabber card by the BeamPro Analysis Software [33].

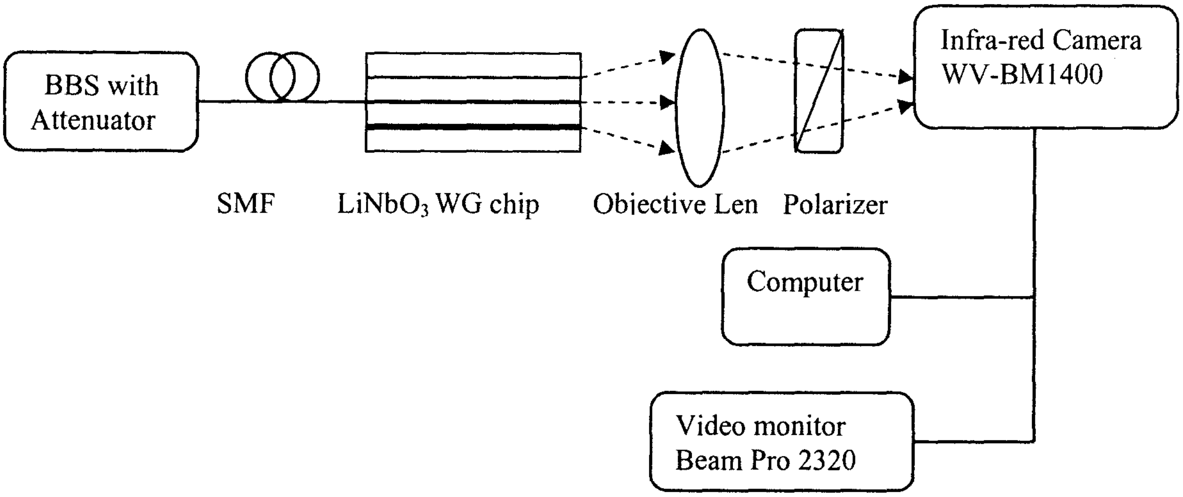

Figure 4.11 The experimental setup for measuring near-field pattern

By using different Ti-strip patterns, the several optical waveguides under different diffusion conditions are fabricated. Figure 4.12 shows the measured near-field profiles of Ti:LiNbO$_3$ waveguide with $t = 4$ hrs, $T = 1050$ °C, $\tau = 0.11$ μm, Pin = 1 mW, and $w = 10$ μm (a), 9 μm (b), 8 μm (c). Figure 4.13 shows the measured near-field profiles of Ti:LiNbO$_3$ waveguide with $t = 3$ hrs, $T = 1050$ °C, $\tau = 0.11$ μm, Pin = 1 mW, and $w = 10$ μm (a), 9 μm (b), 6 μm (c). In both figures, the resolutions along x (vertical axis) and y (horizontal axis) directions are 0.018 μm. All fields are measured at a wavelength of 1.55 μm, except one of Figure 4.13 (c) at a wavelength of 0.633 μm.

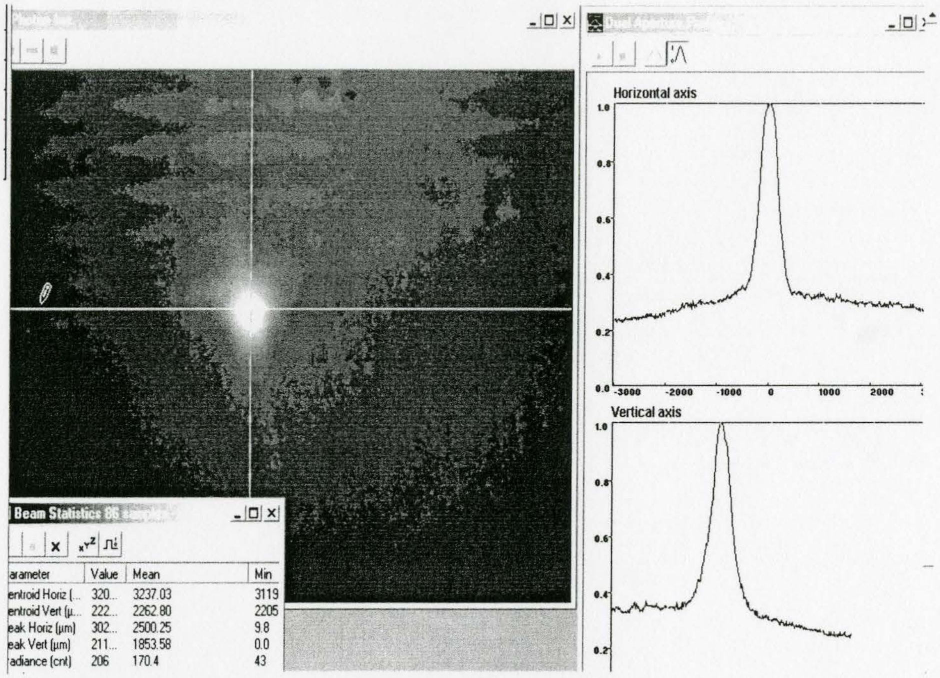

Beam Statistics 86

arameter	Value	Mean	Min
entroid Horiz (...	320...	3237.03	3119
entroid Vert (µ...	222...	2262.80	2205
eak Horiz (µm)	302...	2500.25	9.8
eak Vert (µm)	211...	1853.58	0.0
adiance (cnt)	206	170.4	43

(a) $w = 10$ µm

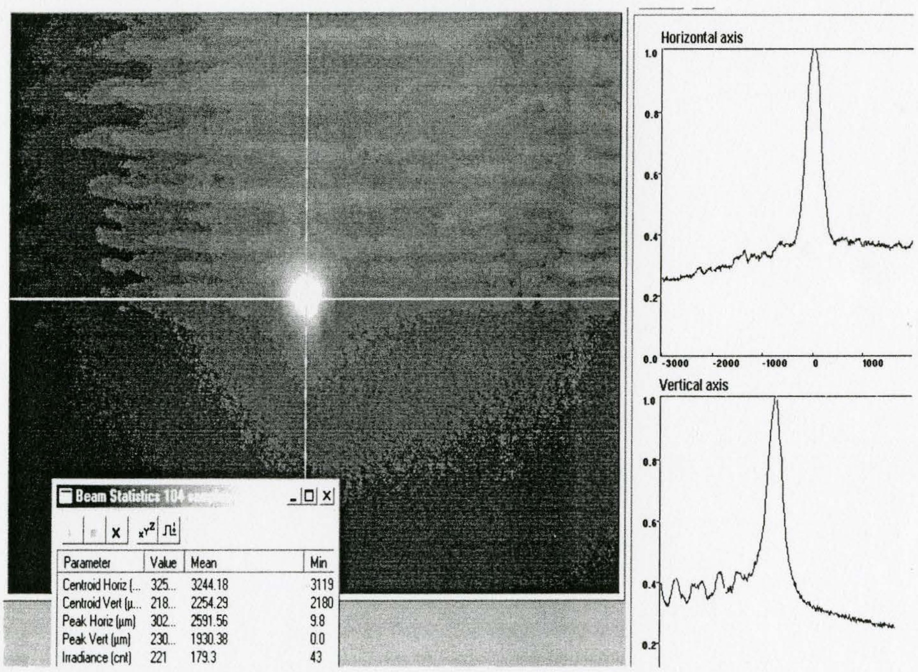

Beam Statistics 104

Parameter	Value	Mean	Min
Centroid Horiz (...	325...	3244.18	3119
Centroid Vert (µ...	218...	2254.29	2180
Peak Horiz (µm)	302...	2591.56	9.8
Peak Vert (µm)	230...	1930.38	0.0
Irradiance (cnt)	221	179.3	43

(b) $w = 9$ µm

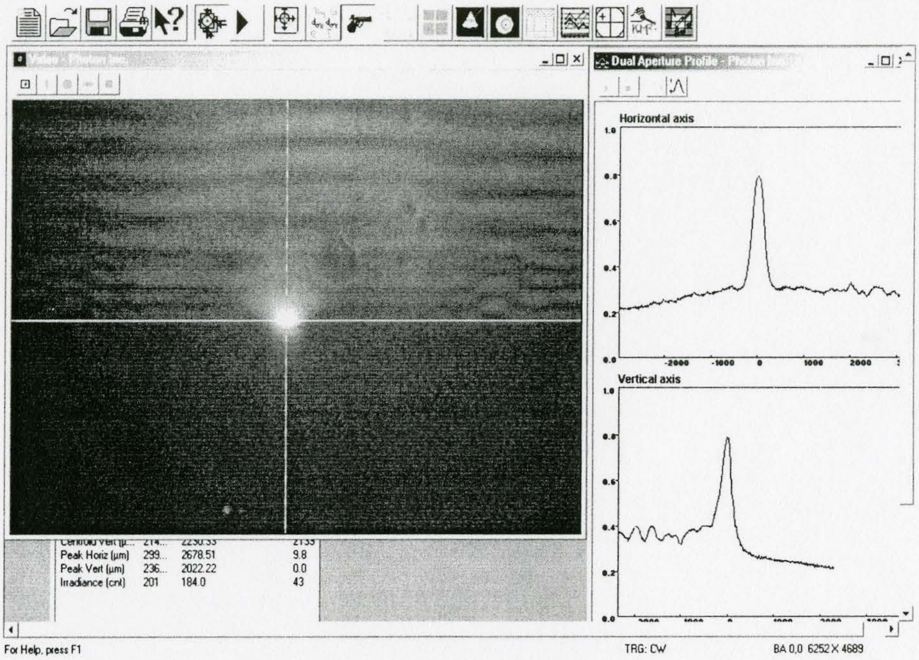

```
Centroid Vert (µ...   214...   2230.33   2133
Peak Horiz (µm)       299...   2678.51   9.8
Peak Vert (µm)        236...   2022.22   0.0
Irradiance (cnt)      201      184.0     43
```

For Help, press F1

TRG: CW

BA 0,0 6252 X 4689

(c) w =8 μm

Figure 4.12 Measured near-field profiles of Ti:LiNbO$_3$ waveguide with t = 4 hrs, T = 1050 °C, τ = 0.11 μm, and w = 10 μm (a), 9 μm (b), 8 μm (c).

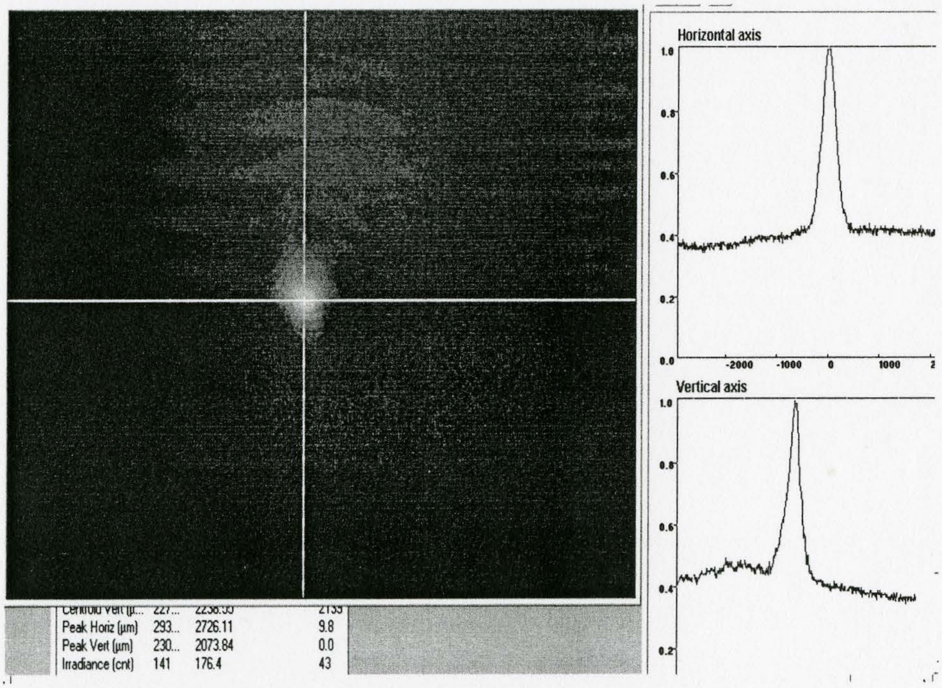

```
Centroid Vert (µ...   227...   2238.55   2133
Peak Horiz (µm)       293...   2726.11   9.8
Peak Vert (µm)        230...   2073.84   0.0
Irradiance (cnt)      141      176.4     43
```

(a) w = 10 μm

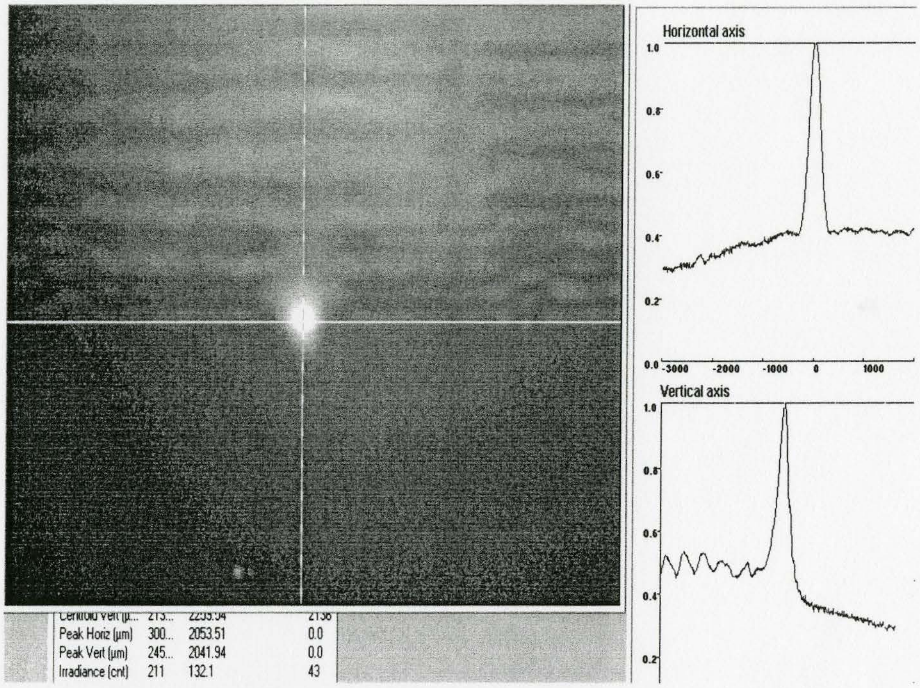

Peak Horiz (µm)	300...	2053.51	0.0
Peak Vert (µm)	245...	2041.94	0.0
Irradiance (cnt)	211	132.1	43

(b) $w = 9$ μm

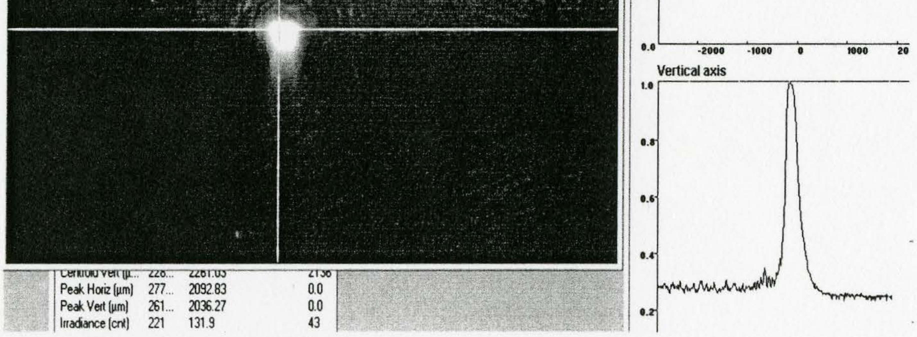

Peak Horiz (µm)	277...	2092.83	0.0
Peak Vert (µm)	261...	2036.27	0.0
Irradiance (cnt)	221	131.9	43

(c) $w = 6$ μm

Figure 4.13 Measured near-field profiles of Ti:LiNbO$_3$ waveguide with t = 3 hrs, T = 1050 °C, τ = 0.11 μm, and w = 10 μm (a), 9 μm (b), 6 μm (c).

From Figure 4.12 to Figure 4.13, as expected, due to the symmetrical nature along y (horizontal axis) direction, the peak positions of the measured fields along y direction are always located at the center of the waveguide (i.e., $y = 0$). However, on the other hand, due to the different Ti strip widths and fabrication conditions, the asymmetrical strengths of the species concentration (or index distribution) along x direction are different so that the peak positions of the measured fields along $x$direction are different, as shown clearly in Figure 4.14, where the different $Ti:LiNbO_3$ waveguides with $T = 1050$ °C, $t = 4$ hrs, and $\tau = 0.11$ μm are measured. Figure 4.15 show the normalized near-field profiles of $Ti:LiNbO_3$ waveguide with $T = 1050$ °C along x direction (a) and y direction(b). In order to compare the modal profiles, the peak positions of modal profiles along x direction are moved to $x = 0$. It is found that measured near-field profiles along y direction (horizontal axis) are Gassian-like and the measured near-field profiles along x direction (vertical axis) are not. In order to compare the modal profile, the simulation and measured results of the normalized near-field profiles of $Ti:LiNbO_3$ waveguide with $T = 1050$ °C, $t = 4$ hrs, $w = 9$ μm, and $\tau = 0.11$ μm are shown in Figure 4.16. From Figure 4.16, the simulation results of the normalized near-field profiles along y direction agree well with measured results. However, there are some discrepancies between the simulation and measured results of the normalized near-field profiles along x direction ($C_0 = 70.72\%$, $D_x = 0.7884$, $D_y = 0.612$). Those may be caused by the measurement setup and accuracy of the equipment.

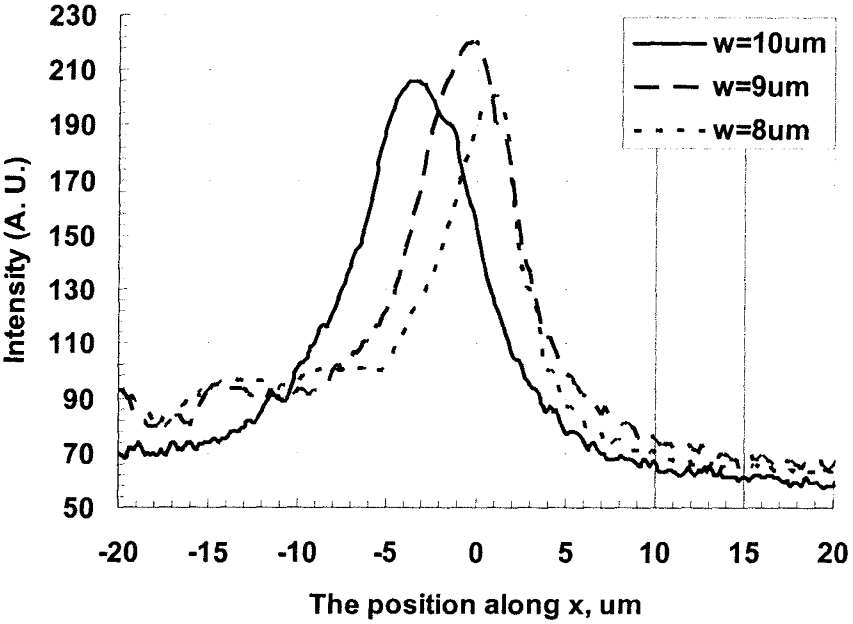

Figure 4.14 Measured near-field profiles of Ti:LiNbO3 waveguide with T = 1050 °C, t = 4 hrs, and τ = 0.11 μm along x direction (vertical axis).

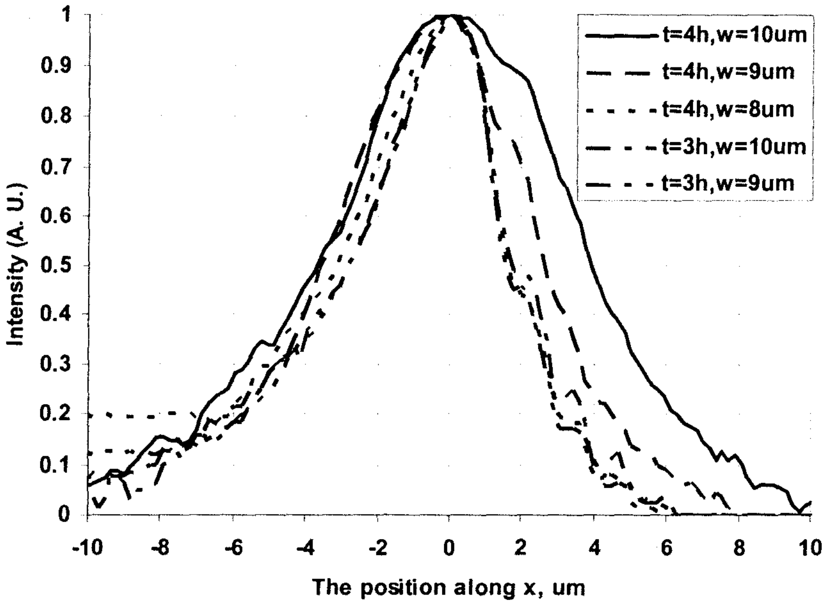

(a) Along x direction (vertical axis)

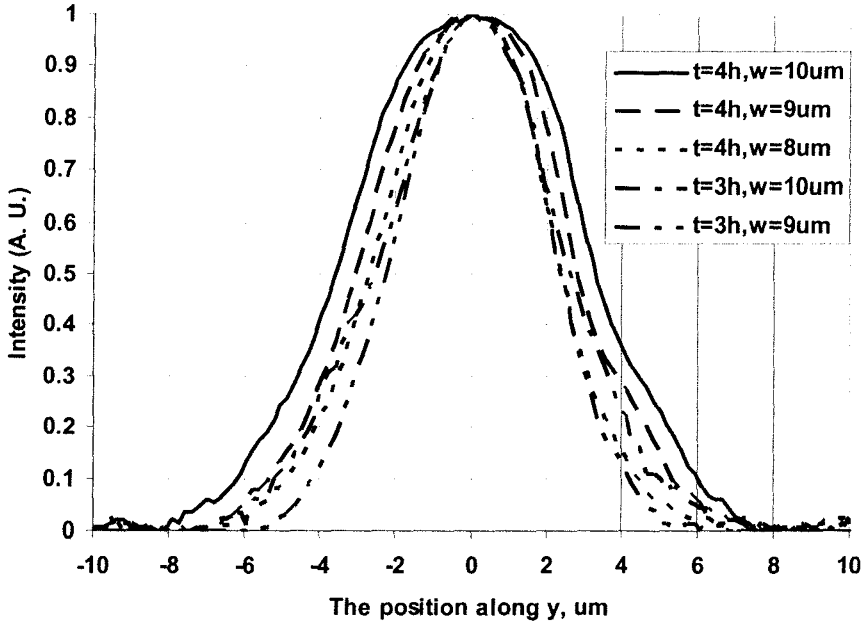

(b) Along y direction (horizontal axis)

Figure 4.15 Normalized near-field profiles of Ti:LiNbO$_3$ waveguide with T = 1050 °C, and $\tau = 0.11$ µm along x direction (a) and y direction(b).

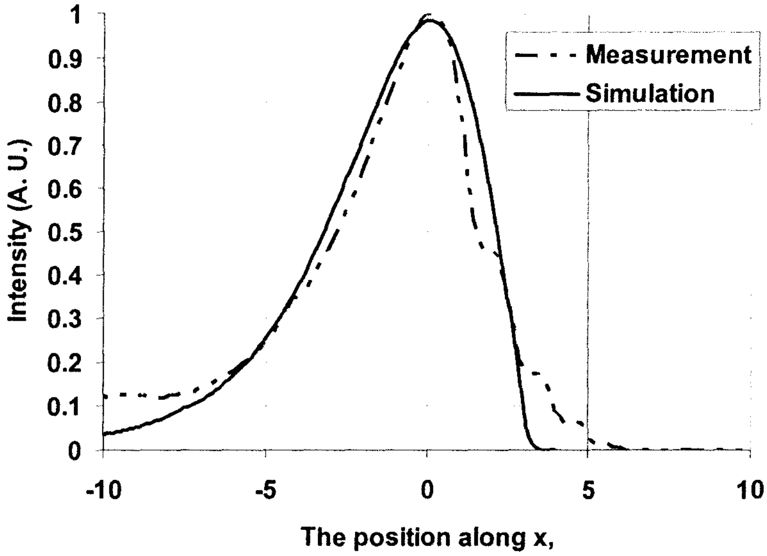

(a) Along x direction (vertical axis)

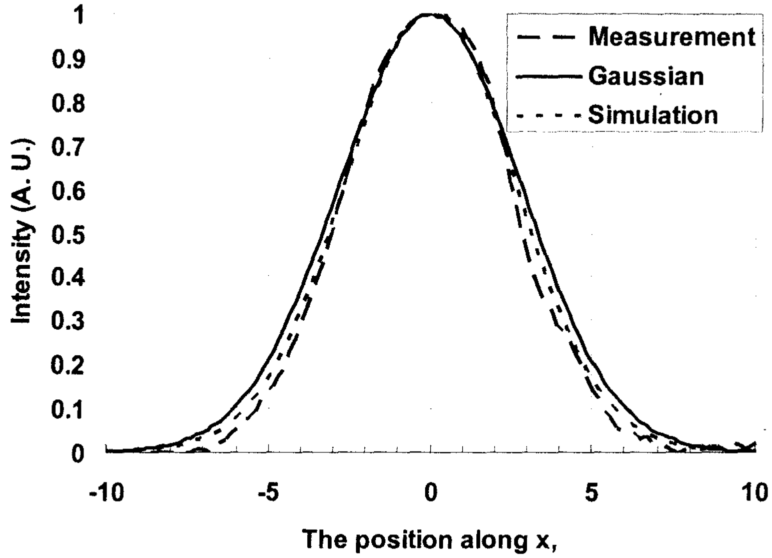

(b) Along *y* direction (horizontal axis)

Figure 4.16 Normalized near-field profiles of Ti:LiNbO$_3$ waveguide with T = 1050 °C, t = 4 hrs, and w = 9 μm, and τ = 0.11 μm along x direction (a) and y direction(b).

4.5 Summary

In this chapter, the material, index, and model properties of Ti:LiNbO$_3$ optical waveguides are summarized and corresponding simulation flow chat is presented. Detailed design, fabrication, and measured results of Ti:LiNbO$_3$ optical waveguides are presented.

Chapter 5

Modeling and Design of APE $LiNbO_3$ Optical Waveguides

As one of the well-known lithium niobate ($LiNbO_3$)-based optical waveguides, the material, index, and modal properties of annealed proton exchanged (APE) $LiNbO_3$-based optical diffused waveguides are described in this chapter. Also design, fabrication, and measured results of APE $LiNbO_3$-based waveguides are given.

5.1 Material Properties of APE $LiNbO_3$ Waveguides

Annealed proton exchanged (APE) $LiNbO_3$ process is an effective technique for the formation of low-loss and high nonlinearity optical waveguides. In this technique, the two-step proton-exchange and thermal annealing process are used. During the stage of proton exchange process, a step-like hydrogen (H^+) profile is retained at relatively low temperature. Then the annealing process at higher temperature produces a highly graded profile. Typical fabrication procedures for APE $LiNbO_3$ waveguides are shown in Appendix B. The related fabrication parameters of the whole APE process: opening width w, exchange temperature T_1, exchange time t_1 of proton exchange process, and thickness τ (diffusion depth), annealing temperature T, annealing time t of thermal annealing process.

5.1.1 Proton exchange (PE) process

The $LiNbO_3$ optical waveguide based on the proton-lithium exchange process was proposed in 1982 [34]. This technique consists in immersing Z-cut or X-cut $LiNbO_3$ substrates into a molten bath of benzonic acid at a fixed temperature between 122 °C (melting point of benzonic acid) and 249 °C (boiling point of benzonic acid) for a given period of time. The index distribution has a step-like profile at the end of exchange process and its depth for the guiding layer depends on the process temperature and time. Overall, the PE process is a low temperature process which creates a high index increase

($\Delta n_e \approx 0.12$ at $\lambda = 0.633$ μm) in the extraordinary refractive index and a slight index decrease ($\Delta n_o \approx -0.04$ at $\lambda = 0.633$ μm) in the ordinary refractive index [35][36]. Due to the nature of the high index change, the PE LiNbO$_3$ optical waveguides have found some applications such as grating beam splitters, polarization strippers, modulators, and birefringence controllers [37].

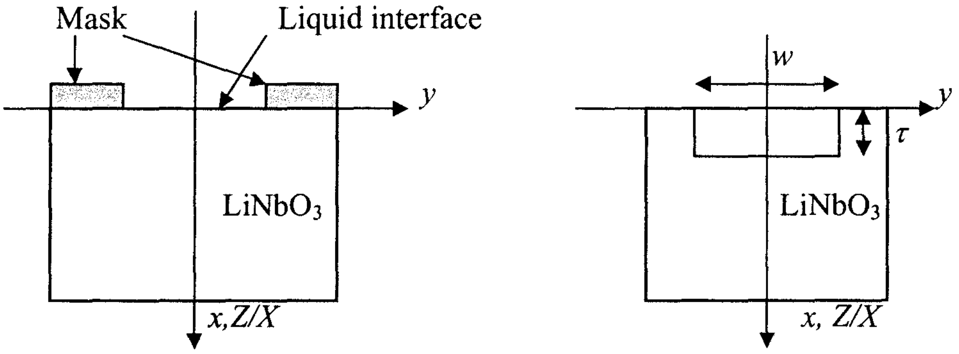

(a) Before PE process (b) After PE process

Figure 5.1 The schematic view of Z-cut or X-cut PE LiNbO$_3$ waveguides

For the Z-cut or X-cut PE LiNbO$_3$ waveguides as shown in Figure 5.1, the index increase in x direction is a step-like profile with the index increase of Δn_e and the depth of τ. This step-like profile is verified by modeling the diffusion profile of the 1D proton change nonlinear diffusion (or inter self-diffusion)equation [39],

$$\frac{\partial C}{\partial t} = D_1 \frac{\partial}{\partial x}\left(\frac{1}{1-\alpha C}\frac{\partial C}{\partial x}\right) \qquad (5.1)$$

where $\alpha = 1 - D_1/D_{1a}$, D_1 is the diffusion coefficient for protons (H$^+$), D_{1a} is the diffusion coefficient for lithium (Li$^+$) ions, and C is the concentration of protons. Because the rate of proton diffusion in is much less than that of the lithium ions diffusing out (e. g., $D_{1a} = 1.62$ μm^2/h and $D_1 = 0.08$ μm^2/h at 200 °C, or $\alpha = 1$), the solution of the above diffusion equation is a step-like function. The dependence of D_1 on temperature T_1 is given by Arrhenius' Law:

$$D_1(T_1) = D_{10}\exp(-E_{10}/k_B T_1) = D_{10}\exp(-T_{10}/T_1) \qquad (5.2)$$

where $D_1(T_1)$ is a diffusion coefficient of the PE process, which depends on the PE temperature T_1 in Kevin (K), D_{10} is the diffusion constant in μm^2/h, E_{10} is the activation energy in eV, and k_B the Boltzmann's constant. The values of the diffusion constant and activation energy are related to the substrate materials, the substrate orientation and the proton source. Some typical values for D_{10}, E_{10}, and T_{10} for proton exchange in Z-cut LiNbO$_3$ using benzoic acid as the proton source are presented in Table 5.1 (here, 150 °C $< T_1 <$ 249°C, and 5 min $< t_1 <$ 5h). By utilizing D_{10}, E_{10}, and T_{10}, for example, the PE diffusion coefficients of Z-cut LiNbO$_3$ with the benzoic acid for different temperatures T_1 can be easily calculated as shown in Table 5.2.

By assuming that the PE diffusion coefficient $D_1(T_1)$ is a constant at the process temperature of T_1, the exchanged depth τ can be obtained analytically by solving the 1D diffusion equation,

$$\tau = 2\sqrt{D_1(T_1)t_1} \qquad (5.3)$$

where T_1 is the PE process temperature and t_1 is the exchange time in the PE process. For the Z-cut LiNbO$_3$ using benzoic acid as the proton source as shown in Table 5.1, E_{01} = 0.974 eV, D_{10}= 1.84×10^9 μm^2/h [39]. From (5.2) and (5.3), the exchanged depth can be rewritten as follows,

$$\tau = \overset{8.57}{\cancel{8.85}} \times 10^4 \sqrt{t_1 \exp(\underset{1.1302\,e4}{\cancel{-5.65\times10^3}} / T_1)}\text{, μm} \qquad (5.4)$$

where T_1 is the PE process temperature in K and t_1 is the exchange time in hour.

Table 5.1 Some typical values for D_{10}, E_{10}, and T_{10} for proton exchange in Z-cut LiNbO$_3$ using benzoic acid

PE Atmosphere	D_{10}, μm^2/h	E_{10}, eV	T_{10}, K	Ref
Benzoic acid	1.84×10^9	0.974	1.1302x10^4	[39]

Table 5.2 The PE diffusion coefficients of *Z*-cut LiNbO$_3$ using benzoic acid

T_1 , °C	$D_1(T_1)$, μm^2/h, Calculated	$D_1(T_1)$, μm^2/h, Experiment [39]
180	0.027243	0.027
200	0.078163	0.081
220	0.205888	0.207

5.1.2 Thermal annealing process

Due to the nature of the high index change and a dead layer, optical waveguides with the PE process suffer high loss and instability. In order to restore the second order nonlinearity and instability, the annealing process is generally needed. Annealing at higher temperature of near 400°C rapidly produces a highly graded profile. The thermal annealing process can lower surface index, allow for tailoring the modal shape, and restore the second order nonlinearity. The graded hydrogen (H$^+$) profile, with lower concentration, extends far deeper than the original exchange depth. The diffusion of the diffused waveguide during the annealing process can be modeled by the 2D thermal diffusion equation of (2.9),

$$\frac{\partial C}{\partial t}=\frac{\partial}{\partial x}(D_x\frac{\partial C}{\partial x})+\frac{\partial}{\partial y}(D_y\frac{\partial C}{\partial y}) \qquad (5.5)$$

where $C(x, y, t)$ is the hydrogen concentration distribution, D_x and D_y are the diffusion coefficients along the *x*-axis and *y*-axis, respectively. As shown in Figure 5.2, the controlling parameters of the fabrication of APE LiNbO3 waveguides during the annealing process are the annealing temperature *T* and annealing time *t*.

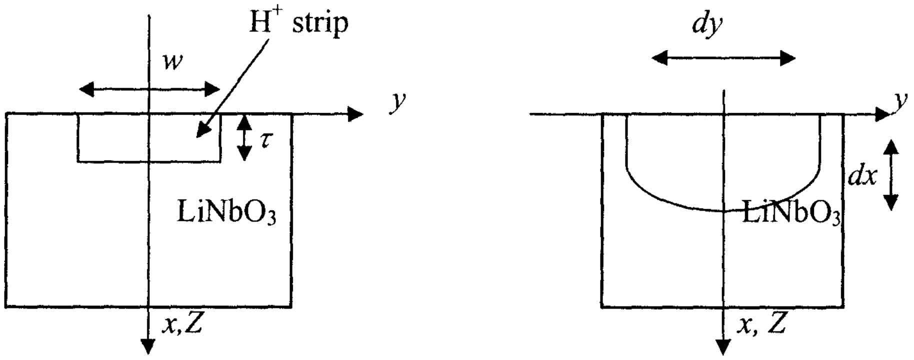

(a) Before annealing process (b) After annealing process

Figure 5.2 The schematic view of *Z*-cut APE $LiNbO_3$ waveguides

First, we introduce the analytical solution (2.30) of proton change linear diffusion equation of (5.6) in the hydrogen diffusion process with constant diffusion coefficients. From Ref [17], it is understood that, as shown in Figure 5.2a, hydrogen diffusion from the PE layer is governed by the initial conditions of a thin surface layer with a constant amount of diffusant and no out-diffusion of H from crystal during the annealing process. In other words, due to the nature of the thin PE layer (or $w >> \tau$, $G(y, t) = 1$ in 2.19), only 1D diffusion equation along x direction is considered here. The initial condition $C(x, t)$ of H concentration is given as follows,

$$C(x, 0) = C_0 \quad \text{for } 0 < x < \tau \tag{5.6}$$

and

$$C(x, 0) = 0 \quad \text{for } x > \tau \tag{5.7}$$

where C_0 is the initial H surface concentration after the PE process (before the annealing process). With the condition of the zero H flow from the surface, as discussed in Chapter 2, the boundary condition of H concentration is given by

$$\left.\frac{\partial C(x,t)}{\partial x}\right|_{x=0} = 0 \tag{5.8}$$

where $C(x, t)$ is the H concentration in μm^{-3} at the distance x in μm and diffusion time t in hour. From (2.31), the solution of diffusion equation of (5.5) is given by

$$C(x,t) = \frac{C_0}{2}\left[erf\left(\frac{\tau + x}{2\sqrt{Dt}}\right) + erf\left(\frac{\tau - x}{2\sqrt{Dt}}\right)\right] = C_0 F(x,t) \tag{5.9}$$

where function $F(x, t)$ and error function *erf*() are defined in Appendix C, and C_0 is the H initial concentration at $t = 0$, and D is the diffusion coefficients along the x-axis. When $\tau << \sqrt{Dt}$, the above equation reduces to Gaussian function,

$$C(x,t) = \frac{C_0 \tau}{\sqrt{\pi D t}} \exp\left(\frac{-x^2}{4Dt}\right) = \frac{Q_0}{\sqrt{\pi D t}} \exp\left(\frac{-x^2}{4Dt}\right) \tag{5.10}$$

where $Q_0 = C_0\tau$ is the amount of H per μm^2 in the PE layer. It is found that the Gaussian function is suitable for analyzing the thin H depth profiles in Z-cut APE LiNbO$_3$ waveguides. However, an order of magnitude difference between calculated Gaussian function and measured profile exists at a depth of 10τ [17].

In order to obtain a better fit between calculated concentration function and measured profile, two separate Gaussian function method for low H concentration tail and high H concentration surface is proposed in Ref [17]. By introducing the interstitial diffusion coefficient D_i and initial H concentration C_{0i} for low H concentration substrate region, the substitutional diffusion coefficient D_s and initial H concentration C_{0s} for high H concentration surface region, where $C_0 = C_{0i} + C_{0s}$, the sum of two Gaussian functions fit easily the measured profile,

$$C(x,t) = C_i(x,t) + C_s(x,t) \tag{5.11}$$

where

$$C_i(x,t) = \frac{C_{0i}}{2}\left[erf\left(\frac{\tau + x}{2\sqrt{D_i t}}\right) + erf\left(\frac{\tau - x}{2\sqrt{D_i t}}\right)\right]$$

$$C_s(x,t) = \frac{C_{0s}}{2}\left[erf\left(\frac{\tau + x}{2\sqrt{D_s t}}\right) + erf\left(\frac{\tau - x}{2\sqrt{D_s t}}\right)\right]$$

In the solution of two Gaussian functions of (5.11), constant amount of H in the annealing process is assumed. In fact, the flowing wet oxygen acts as a constant source C_{0w} of H at the PE surface and additional term of H concentration of (5.11) is needed. For the constant source C_{0w}, the boundary condition at the surface ($x = 0$) is given by

$$C_w(0, t) = C_{0w} \quad \text{for } t > 0 \tag{5.12}$$

By considering the fact that the hydrogen (H) due to the wet oxygen annealing enters the PE samples primarily as an interstitial species [17], the solution of the 1D diffusion equation from a constant source is given as the following,

$$C_w(x,t) = C_{0w} erfc\left(\frac{x}{2\sqrt{D_i t}}\right) \tag{5.13}$$

where the function *erfc*() is the complementary error function defined in Appendix C. The overall expression of the H concentration in the APE $LiNbO_3$ waveguides is obtained,

$$C(x,t) = C_i(x,t) + C_s(x,t) + C_w(x,t) \tag{5.14}$$

From the above solution of (5.14), two different diffusion mechanisms are represented: a finite layer diffusion source of the PE region and a constant surface diffusion source from the water vapor. This expression also involves two species of interstitial H and substitutional H, each having a different diffusivity. The interstitial H enters the samples from wet oxygen annealing as well as during PE. The substitutional H enters the crystal only through the PE. The substitutional H is the most important H component because it forms crystal bonds and alters the extraordinary refractive index. For example, the best-fit values of the diffusivities $D_s \cong 5.0\times10^{-12} cm^2/s$ and $D_i \approx 1.4\times10^{-11} cm^2/s$ (or $D_i \approx 3D_s$) for the *Z*-cut APE $LiNbO_3$ waveguides are nearly constant over the full range of annealing times from 6 to 180 minutes. So are the best-fit values for the *X*-cut APE $LiNbO_3$ waveguides: $D_s \approx 3.4\times10^{-12} cm^2/s$ and $D_i \approx 1.3\times10^{-11} cm^2/s$ (or $D_i \cong 3D_s$) [17].

Figure 5.3 shows the hydrogen concentration distribution with a function of x of *Z*-cut APE $LiNbO_3$ waveguide with following parameters: $\lambda = 0.6328$ μm, $T = 400$°C, $\tau = 0.65$ μm, $t = 2.25$ hrs (or 135 min) [17]. From Figure 5.3, it is found that interstitial H diffuses faster than the substitutional H and interstitial H is the main contributor deep into the crystal. Near the surface (or small x), the substitutional H dominates. Figure 5.4 shows comparison of the hydrogen concentration of *Z*-cut APE $LiNbO_3$ waveguide solved by analytical and numerical methods.

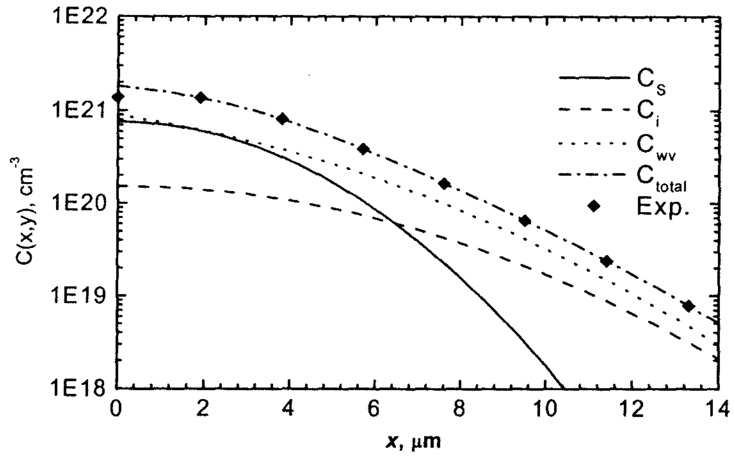

Figure 5.3 The hydrogen concentration distribution with a function of x of Z-cut APE LiNbO3 waveguide with following parameters: annealed time 2.25 hrs, annealed temperature 400 °C [17].

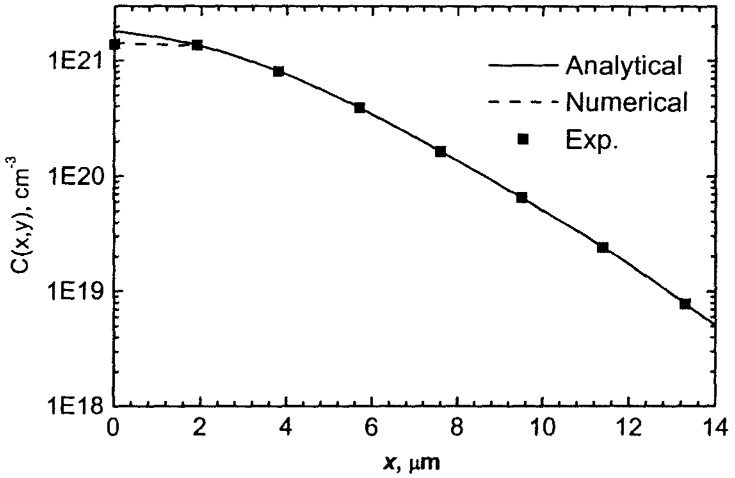

Figure 5.4 Comparison of the hydrogen concentration of Z-cut APE LiNbO3 waveguide solved by analytical and numerical methods with following parameters: annealed time 2.25 hrs, annealed temperature 400 °C [17].

Overall, the controlling parameters for the fabrication of the APE $LiNbO_3$ waveguide are the initial pattern parameters (w, C_0), the $LiNbO_3$ substrate parameters such as composition of Li, the crystal cut, and material dispersion $n_b(\lambda)$, and the diffusion process (t_1, T_1, A_1; τ, t, T, A). Once the $LiNbO_3$ substrate, mask geometry, and diffusion conditions are determined, the APE $LiNbO_3$ waveguides are formulated.

5.2 Index Properties of APE $LiNbO_3$ Waveguides

As we know, the extraordinary refractive index depth profile in the PE $LiNbO_3$ is approximately a step function. With the annealing process, the index depth profile becomes highly graded. The empirical models between the induced index change and the hydrogen concentration at certain wavelengths are obtained by several research groups. By fitting the parameters within a wavelength range from 0.633μm to 1.55 μm, a novel combined model of the index change Δn_e is proposed.

5.2.1 Proton exchange (PE) process

The extraordinary refractive index depth profile in the PE $LiNbO_3$ is a step-like function, which depends on the process time and temperature. Through some experimental results, a Sellmeier expression can be obtained [40],

$$\Delta n_e = \sqrt{a_1 + \frac{a_2}{\lambda^2 - a_3^2}} \tag{5.15}$$

where a_1, a_2, and a_3 are fitting parameters and λ is a wavelength in micron unit. For the PE waveguides, $a_1 = 7.43\times10^{-3}$, $a_2 = 2.64\times10^{-3}$, $a_3 = 0.336$ [40]. For the APE waveguides, $a_1 = 3.43\times10^{-3}$, $a_2 = 1.10\times10^{-3}$, and $a_3 = 0.326$.

5.2.2 Annealed PE (APE) process

We can model the diffusion of the refractive index when annealed with the following initial conditions [17],

$$n_e(x,0) = n_e \quad for\ 0 < x < \tau \tag{5.16}$$

and

$$n_e(x,0) = n_{eb} \quad for\ x > \tau \tag{5.17}$$

where n_{eb} is the extraordinary refractive index of the bulk LiNbO$_3$ crystal and n_e is the index of the PE layer. So we label it as *Model* 1,

$$n_e(x,t) = n_{eb} + \frac{\Delta n_e}{2}\left(erf\left(\frac{(\tau + x)}{2\sqrt{D_n t}}\right) + erf\left(\frac{(\tau - x)}{2\sqrt{D_n t}}\right) \right) = n_{eb} + \alpha C(x,t) \qquad (5.18)$$

where $\Delta n_e = n_e - n_{eb}$ is the initial change for the PE crystal, α is the scaling factor in (H ions per cm^3)$^{-1}$, and D_n is the index diffusivity with the similar level of substitutional diffusivity (or $D_n \approx D_s$). For example, for the *Z*-cut PE LiNbO$_3$ waveguides, n_{eb} = 2.204 at λ = 0.6328 μm, and $n_e(x,t) - n_{be} = \alpha C(x,t)$ with $\alpha = 1.85\times10^{-23}$. For the *X*-cut PE LiNbO$_3$ waveguides, where $n_e(x,t) - n_{be} = \alpha C(x,t)$ with $\alpha = 3.9\times10^{-23}$.

In general, the index models of APE LiNbO$_3$ waveguides can be obtained by fitting the measuring results with certain wavelengths and fabrication parameters. Through those empirical models, the relations between the index change Δn_e and the hydrogen concentration at certain wavelengths are obtained by several research groups. For example, the index change Δn_e at a wavelength of 0.633μm, 0.807μm, 1.55 μm is given by [41][42][43] (*Model 2*),

$$\Delta n_e(x,y,C,\lambda = 0.633\ \mu\text{m}) = \begin{cases} 0.2115\, C(x,y), & C < 0.05 \\ 0.0669\, C(x,y) + 0.00724, & 0.05 \le C < 0.16 \\ 0.235\, C(x,y) - 0.0197, & 0.16 \le C < 0.55 \\ 0.0676\, C(x,y) + 0.0724, & C \ge 0.55 \end{cases} \qquad (5.19)$$

$$\Delta n_e(x,y,C,\lambda = 0.807\ \mu\text{m}) = \begin{cases} 0.184C(x,y), & C < 0.05 \\ 0.0582C(x,y) + 0.0063, & 0.05 \le C < 0.16 \\ 0.2044C(x,y) - 0.0171, & 0.16 \le C < 0.55 \\ 0.0588C(x,y) + 0.063, & C \ge 0.55 \end{cases} \qquad (5.20)$$

$$\Delta n_e(x,y,C,\lambda = 1.55\ \mu\text{m}) = \begin{cases} 0.158C(x,y), & C < 0.05 \\ 0.05C(x,y) + 0.0054, & 0.05 \le C < 0.16 \\ 0.176C(x,y) - 0.0147, & 0.16 \le C < 0.55 \\ 0.051C(x,y) + 0.054, & C \ge 0.55 \end{cases} \qquad (5.21)$$

By fitting the parameters within a wavelength range from 0.633μm to 1.55 μm, a novel combined model of the index change Δn_e is obtained,

$$\Delta n_e(x,y,\lambda)=\begin{cases}(0.1310\lambda^2-0.3438\lambda+0.3761)C, & C<0.05\\ (0.0425\lambda^2-0.1111\lambda+0.1202)C+ & \\ (0.004569\lambda^2-0.01198\lambda+0.01299), & 0.05\le C<0.16\\ (0.1501\lambda^2-0.3919\lambda+0.4230)C- & \\ (0.0128\lambda^2-0.0333\lambda+0.0357), & 0.16\le C<0.55\\ (0.0437\lambda^2-0.1135\lambda+0.1219)C+ & \\ (0.0457\lambda^2-0.1198\lambda+0.1299), & C\ge 0.55\end{cases} \tag{5.22}$$

where λ is the operating wavelength from 0.633μm to 1.55 μm. Figure 5.5 shows the comparison of index change Δn_e of Z-cut APE LiNbO$_3$ waveguide with following parameters: $\lambda = 0.6328$ μm, $T = 400$°C, $\tau = 0.65$ μm, and $t = 1.5$ hrs. From Figure 5.5, it is found that both models agree with the measured results well.

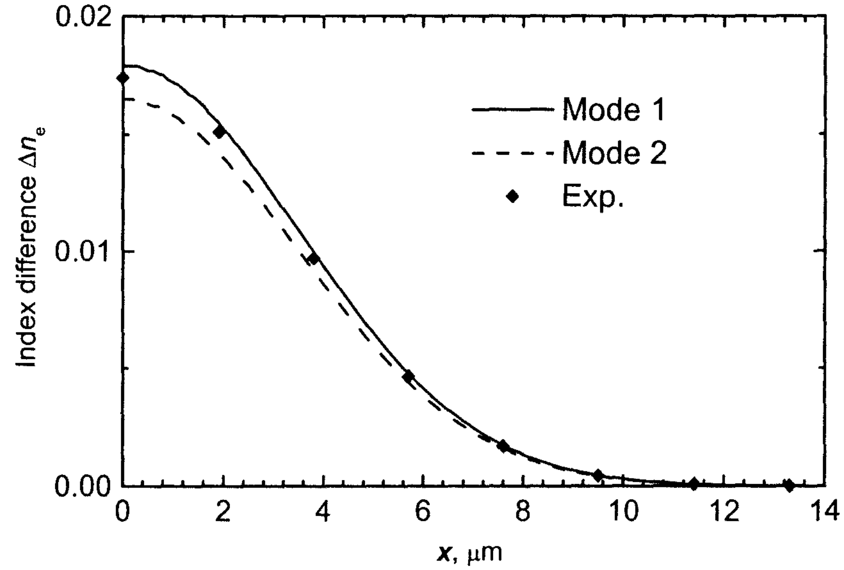

Figure 5.5 Comparison of index change Δne of Z-cut APE LiNbO$_3$ waveguide with following parameters: $\lambda = 0.6328$ μm, $T = 400$°C, τ= 0.65 μm, $t = 1.5$ hrs, and exp. results [17]

5.3 Modal Properties of APE LiNbO$_3$ Waveguides

After getting the index distribution of the APE LiNbO$_3$ optical waveguides, the modal properties are readily solved by the methods discussed in Chapter 3. The overall simulation flow chat of APE LiNbO$_3$ waveguides involving material and modal properties is shown in

Figure 5.6. Once modal profiles (i.e., electric fields *E*x/*E*y) and modal index (i.e., effective index n_{eff}) are solved, other modal properties of the LiNbO$_3$-based optical waveguides such as magnetic fields and confinement factor are easily obtained. In our current work, the *Z*-cut APE LiNbO$_3$ waveguides with $T = 350°\mathrm{C}$, $t = 6.25 \sim 9.75$ hrs, $T_l = 200°\mathrm{C}$, $t_l = 1.92$ hrs, $w = 6.0$ μm are used. Figure 5.7 shows typical electric fields *E*x of TM mode with the mesh size $\Delta x = \Delta y = 0.2$ μm, where $t = 6$ hrs.

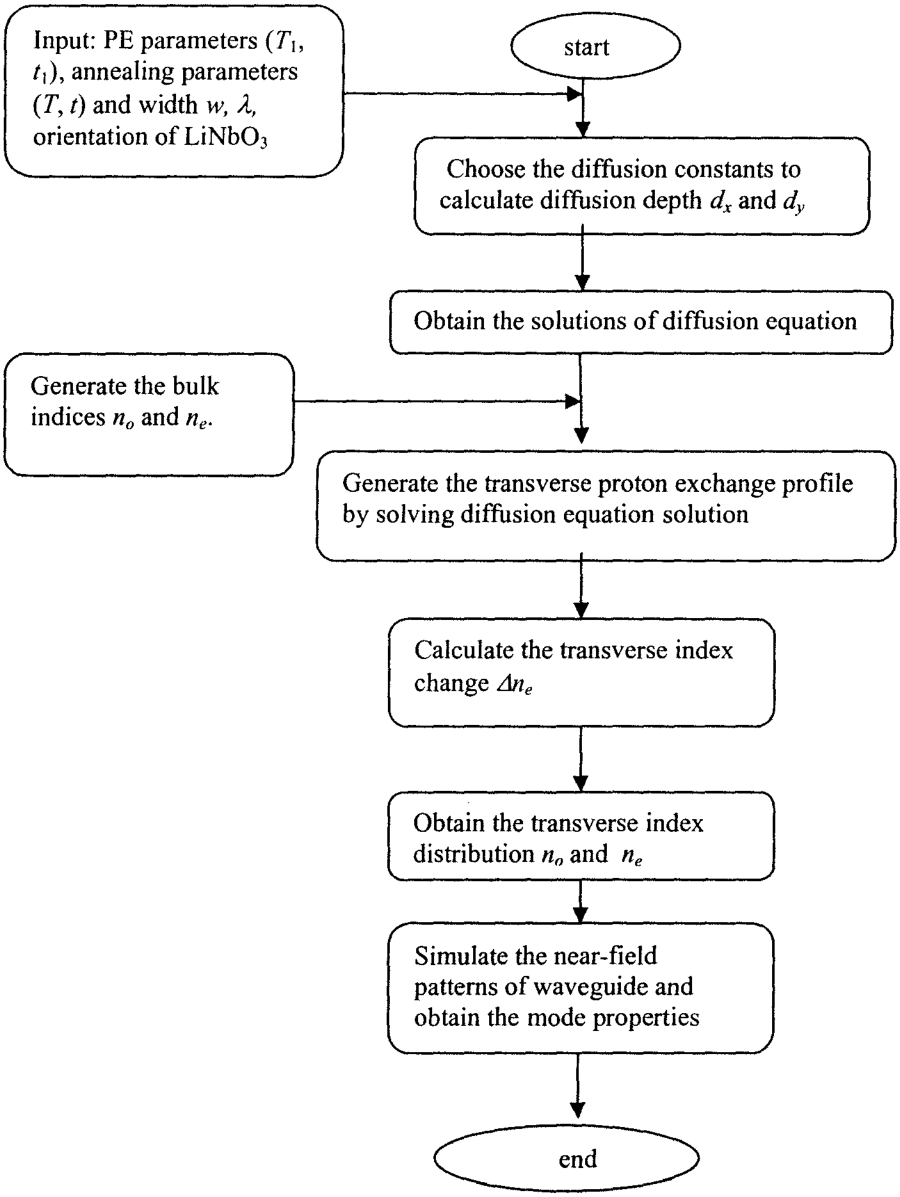

Figure 5.6 Flow chat of simulation of APE $LiNbO_3$ index profile

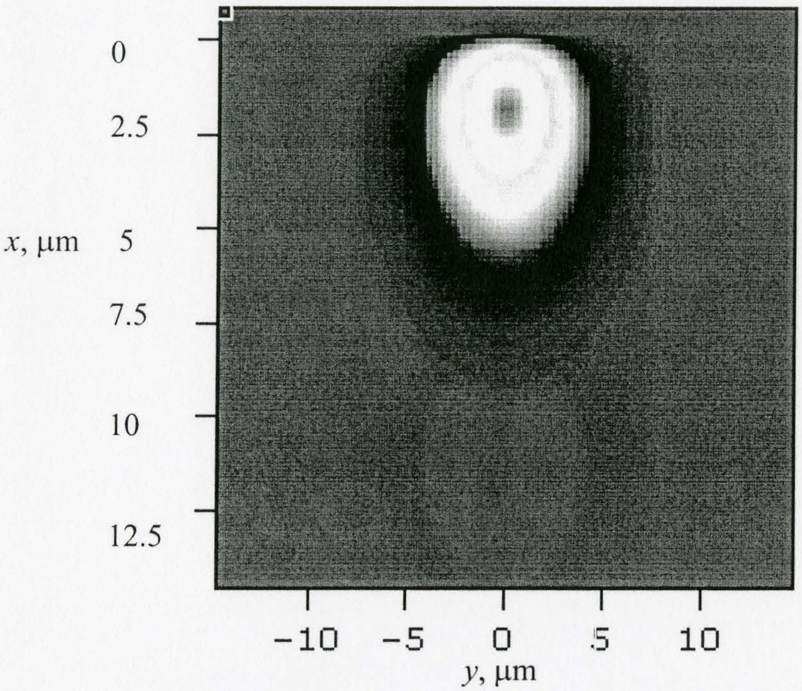

Figure 5.7 Electric field *E*x of TM mode of *Z*-cut APE $LiNbO_3$ waveguide with

$T_l = 200$ °C, $t_l = 2$ hrs, w = 6μm, $T = 350$ °C, $t = 6$ hrs

5.4 Design and Fabrication of APE $LiNbO_3$ waveguides

In order to verify the model and gain some physical insight of guiding waveguides, some *Z*-cut APE $LiNbO_3$ waveguides are fabricated in McMaster University [45]. Here we describe fabrication and measurement results of the APE waveguides. By comparing with the measured results, the modal properties of APE waveguides are obtained through anisotropic mode solvers discussed in Chapter 2.

5.4.1 Design of *Z*-cut APE $LiNbO_3$ waveguides

Like Ti:$LiNbO_3$ waveguides, once the relationship between the modal properties and process parameters is built, it is ready to design the APE $LiNbO_3$ waveguides. For the sake of simplicity, the *Z*-cut APE $LiNbO_3$ waveguides are selected. By following the simulation procedure as shown in

Figure 5.6, the modal fields of the *Z*-cut APE $LiNbO_3$ waveguides with different fabrication conditions can be calculated. Table 5.3 shows the fabrication conditions of the *Z*-cut APE $LiNbO_3$ waveguides [45].

Table 5.3 Fabrication conditions of APE in *Z*-cut $LiNbO_3$ waveguides

Sample No	λ(μm)	*w* (μm)	Mask film	Proton exchange		Annealing		
				T_1 (°C)	t_1 (hrs)	Gas	*T* (°C)	*t* (hrs)
current work	1.55	6	Cr	200	2.0	air	350	6.00
[45]	1.55	6	Cr	200	1.92	air	350	6.25, 6.75, 7.25, 7.75, 8.25, 9.25, 9.75

Note: *w*--width of mask opening, T_1--PE temperature, t_1--PE duration, *T*--annealing temperature, *t*--annealing duration

From Table 5.3 in the proton exchange process, the dicing pieces with 6 μm opening width are put into the benzoic acid for 1.92 hrs at 200°C. In the thermal annealing process, the mask-removing pieces are put into a quartz tube furnace with air atmosphere at 350°C. The annealing time is from 6.25 to 9.75 hrs.

5.4.2 Fabrication of *Z*-cut APE $LiNbO_3$ waveguides

As discussed in Appendix C, the fabrication procedure of APE waveguides consists of three steps: a photolithography process, the proton exchange (PE) process, and the annealing process. In the photolithography process, 3-inch *Z*-cut $LiNbO_3$ substrate is patterned by 1-μm thickness positive photoresist PR1808. The mask film is a 50-nm thickness chromium film.

Figure 5.8 shows optical microscope photographs of the waveguide channel pattern: (a) Central part of the waveguide array sample, and (b) typical waveguide after lift off.

(a) Central part of the waveguide array sample(×50)

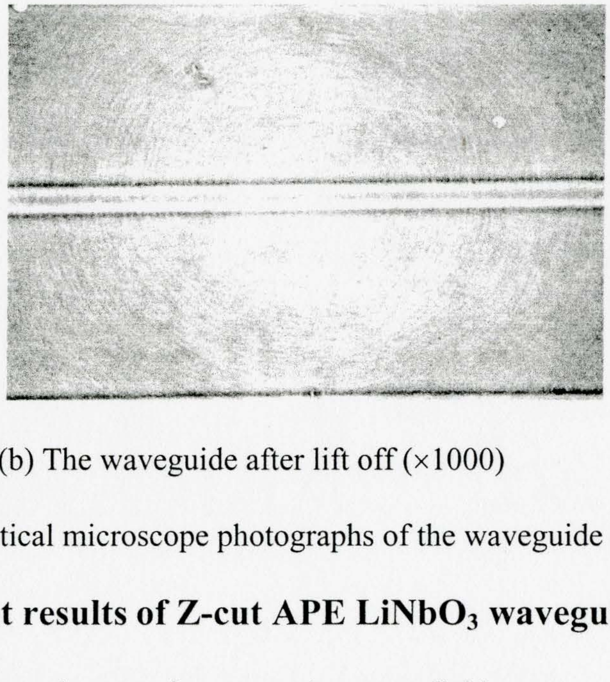

(b) The waveguide after lift off (×1000)

Figure 5.8 Optical microscope photographs of the waveguide channel pattern

5.4.3 Experiment results of Z-cut APE $LiNbO_3$ waveguides

The experimental setup for measuring near-field pattern and loss is shown in Figure 5.9 [45]. In this setup, a broad band source (BBS) with 1.55 μm central wavelength and a attenuator for controlling the source power are utilized. The connection between the single mode fiber and APE $LiNbO_3$ waveguide is through butt coupling. The output near-field pattern of APE $LiNbO_3$ waveguide is amplified by a 10X objective lens with a numerical aperture of 0.25 and captured by a CCD camera. The measurement results of the CCD camera are collected and analyzed through a video grabber card by the BeamPro Analysis Software [33]. The resolutions along x (vertical axis) and y (horizontal axis) directions are 0.48 μm.

Figure 5.10 shows the measured insertion loss of the 2-cm long waveguide with a function of the annealing time. From Figure 5.10, the lowest insertion loss is around 4 dB, in which the annealing time is 7.75 hrs.

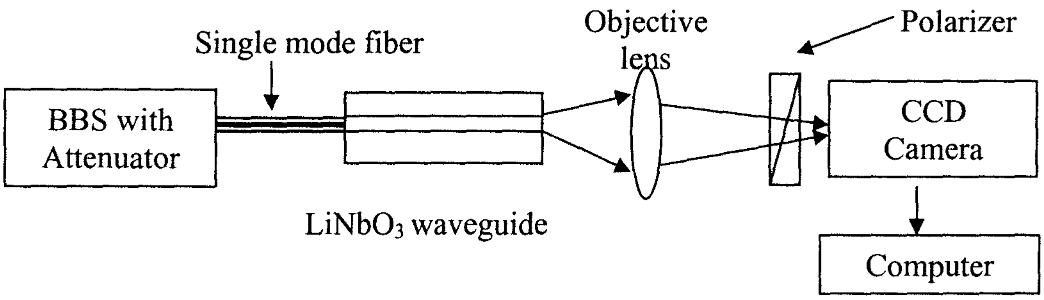

Figure 5.9 The experimental setup for measuring near-field pattern and loss [45]

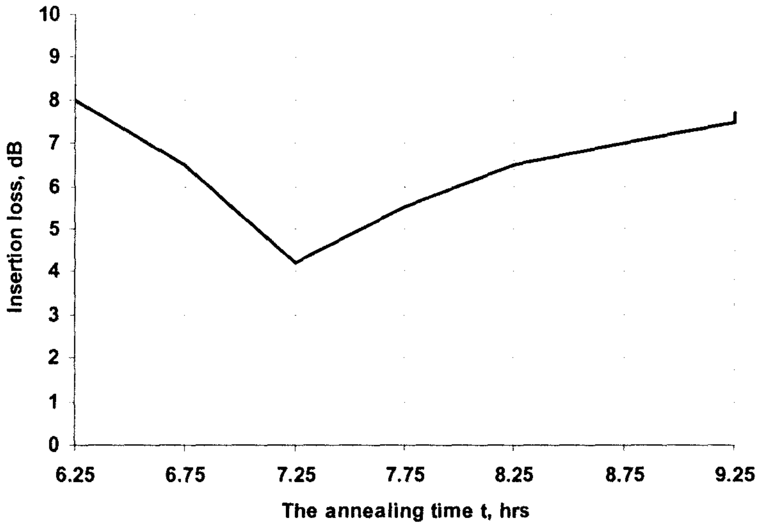

Figure 5.10 Measured waveguide insertion loss of the 2-cm long waveguide with a function of the annealing time [45].

Figure 5.11 shows the measured near-field profiles of corresponding 6-μm wide waveguide (i.e., proton exchange for 1.92 hrs at 200°C and thermal annealing for 7.75 hrs at 350°C). As expected, the measured near-field profiles along *y* direction (horizontal axis) are symmetrical and the peak positions are fixed at $y = 0$. However, due to the different annealing time, the peak positions of the measured near-field profiles along *x* direction (vertical axis) are different. Figure 5.12 show the normalized near-field profiles of APE $LiNbO_3$ waveguide with $T = 350$ °C along *x* direction (a) and *y* direction (b). It is found that measured near-field profiles along *x* and *y* directions are Gassian-like.

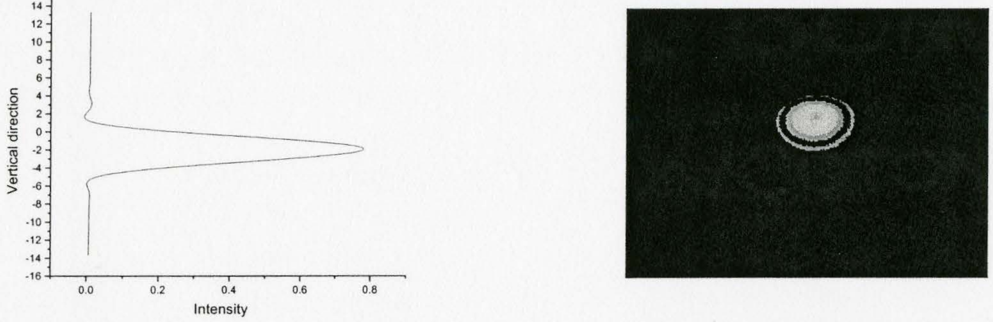

(a) The vertical (*x*) direction

(b) 2D near-field profile

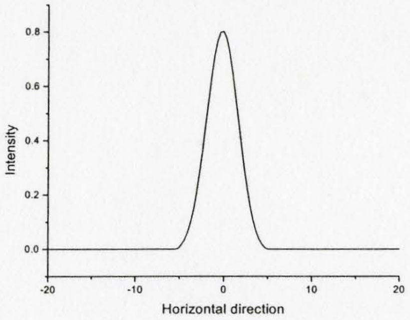

(c) The horizontal (*y*) direction

Figure 5.11 Measured near-field profiles for 6 μm wide waveguide after proton exchange for 1.92 hrs at 200°C and annealing for 7.75 hrs at 350°C: (a) The vertical (*x*) direction, (b) 2D near-field profile, and (c) The horizontal (*y*) direction [45].

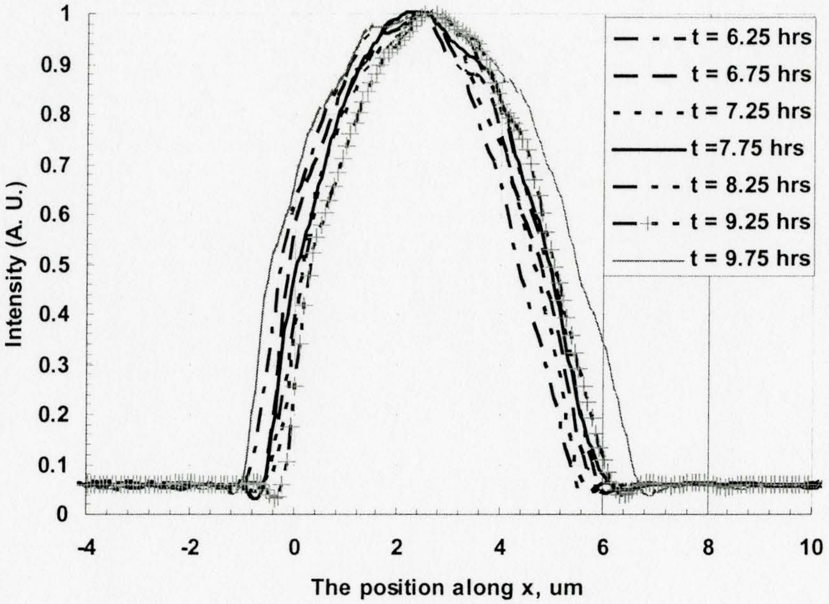

(a) The vertical (x) direction

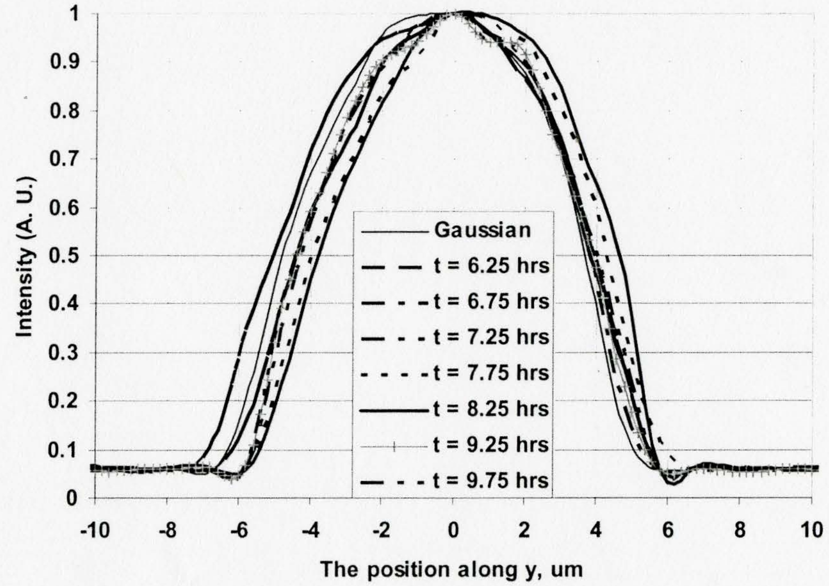

(b) The horizontal (y) direction

Figure 5.12 Normalized near-field profiles for 6 μm wide APE waveguide at $T = 350^{\circ}$C: (a) The vertical (x) direction, (b) The horizontal (y) direction.

In order to compare the modal profile, the simulation and measured results of the normalized near-field profiles of Z-cut APE $LiNbO_3$ waveguide with T_l = 200°C, t_l = 1.92 hrs, T = 350°C, t = 7.25 hrs, and w = 6.0 μm are shown in Figure 5.13. From Figure 5.13, the simulation results of the normalized near-field profiles along x and y direction both agree well with measured results(C_0 = 100.0%, D_x = 1.8628, D_y = 1.5479).

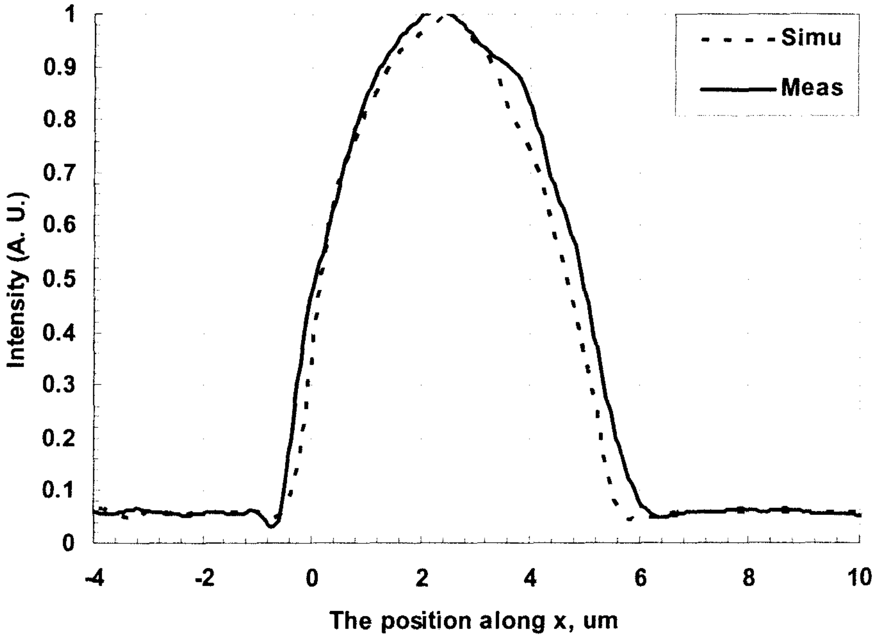

(a) The vertical (x) direction

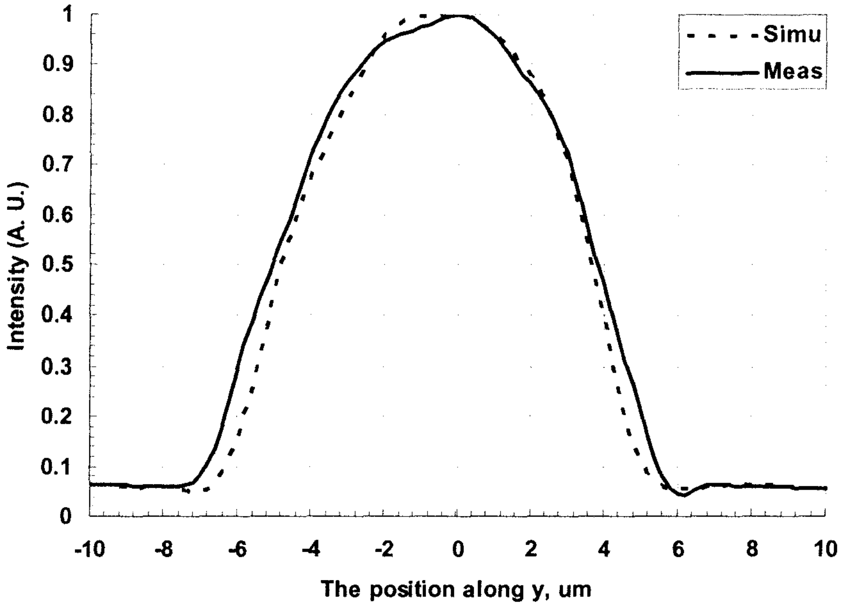

(b) The horizontal (y) direction

Figure 5.13 Measured and simulated near-field profiles for 6 μm wide APE waveguide with T_l = 200°C, t_l = 1.92 hrs, T = 350°C, t = 7.25 hrs, and w = 6.0 μm: (a) The vertical (x) direction, (b) The horizontal (y) direction.

5.5 Summary

In this chapter, the material, index, and model properties of APE $LiNbO_3$ optical waveguides are summarized and corresponding simulation flow chat is presented. Detailed design, fabrication, and measured results of APE $LiNbO_3$ optical waveguides are presented.

Chapter 6

Characteristics of Ti:LiNbO$_3$ and APE LiNbO$_3$ Waveguides

The refractive index distribution of the optical waveguide determines its optical properties such as mode profile, effective index, single-mode condition, optical loss, and coupling loss, which we discussed in the previous chapters. In this chapter, we start to reconstruct the refractive index distribution of the optical waveguides by using the measurement results of modal properties such as mode profile and effective index. First, theoretical principles are reviewed and their simulation flow chats are presented. Then applications to different diffusion techniques such as Ti:LiNbO$_3$ and APE LiNbO$_3$ waveguides are discussed. Finally, simulation results are given.

6.1 Characteristics of LiNbO$_3$ Optical Waveguides

The refractive index profile is one of the most important properties of an optical waveguide. As long as the refractive index of the optical waveguide is known, the modal properties of the waveguide such as the propagation loss, cut-off wavelength, and modal profile can be easily determined. The main task to design the optical waveguide, by adjusting the design and control parameters used in the fabrication process, is to modify and optimize the index profile to meet some specific requirements such as low loss, modal spot size, single-mode operation, and low coupling loss. Therefore, it is very important to establish an efficient method for measuring the index distribution profile as a function of waveguide design and fabrication process parameters.

Various methods are developed to determine the refractive index distribution of waveguides, which have been categorized into two groups: indirect or direct methods (including modal index and near-filed) as shown in Figure 6.1[52]. In the indirect method, the index profile is calculated from the species concentration profile, which can be obtained by using secondary ion mass spectrometry (SIMS) technique. It also requires knowing in advance the relation between the species concentration and refractive index variations. In the direct method, the index profile is directly calculated from the measured optical properties such as modal profile and modal index. Again, the index profile of the optical waveguide can be obtained by using direct reverse method and the iterative simplex method. Here some direct methods, based on mode effective index and near-field mode profile, are introduced briefly.

$$\text{Characteristics of waveguides}\left\{\begin{array}{l}\text{Compositional method: SIMS}\\ \text{Effective index}\left\{\begin{array}{l}\text{Reverse method: IWKB}\\ \text{Simplex: FDM}\end{array}\right.\\ \text{Near field}\left\{\begin{array}{l}\text{Reverse method}\\ \text{Simplex: FDM}\end{array}\right.\end{array}\right.$$

Figure 6.1 Simple classification of characteristics of waveguides

6.1.1 Direct method based on effective index

The direct method based on effective index of the guided modes was proposed by White [47] to predict the shape of the index profile of the optical diffused waveguide. It assumes that the index profile changes monotonically or symmetrically. For weakly guiding waveguide, the optical field strength E(x,y) is described by the 1D scalar wave equation of (3.8), which is rewritten as follows,

$$\frac{d^2}{dx^2}E(x)+\left[k^2(n^2(x)-n_{eff,m}{}^2)\right]E(x)=0 \qquad (6.1)$$

where k(i.e., ω/c) is the propagation constant in free space, and $n_{\text{eff},\,m}$ is the effective index of the mth guided mode and m = 0, 1, 2, ..., M-1 (M is the number of the guided modes). By assuming the one side index profile with air-surface interface (p = 1), the WKB solution of (3.11) of the wave equation of (6.1) is rewritten as follows [47],

$$\int_0^{x_m}\sqrt{n^2(x)-n_{eff,m}{}^2}\,dx=(m+\frac{3}{4})\frac{\lambda}{2} \qquad (6.2)$$

where m = 0, 1, 2, ..., M-1 and x_m is defined by $n(x_m) = n_{\text{eff},\,m}$. In order to determine the values of $x_{t,\text{m}}$ (or the index distribution $n(x)$), the above WKB solution is proceeded by a sum of integral [47],

$$\sum_{k=1}^{m} \int_{x_{k-1}}^{x_k} \sqrt{n^2(x) - n_{eff,m}{}^2}\, dx = (m + \frac{3}{4})\frac{\lambda}{2} \tag{6.3}$$

where we assume $n(x)$ is a piecewise linear function connecting the measured values of $n_{\text{eff, m}}$,

$$n(x) \approx n_{eff,k} + \frac{n_{eff,k-1} - n_{eff,k}}{x_k - x_{k-1}}(x_k - x) \tag{6.4}$$

where $x \in [\, x_{k-1},\, x_k]$. if we let $n(x)$ + $n_{\text{eff,m}}$ be replaced by a midpoint value of $[(n_{k-1} + n_k)/2] + n_{\text{eff, m}}$ for $x \in [\, x_{k-1}, x_k]$, the solution for x_k is obtained.

Originally, due to the obvious reasons, this algorithm is only accurate and efficient for highly multimode waveguide. Later, a different method for the construction of the index profiles from the measured effective indices was proposed by Chiang [48], in which a continuous effective-index function is utilized. In this method, the key step is how to construct the continuous effective-index function based on the measured modal indices. Among them, as shown in [48] [49], with considering the different combinations such as polarization (TE and TM) and external refractive indexes, the refractive index distribution with less number of modes, even for single-mode case, can be calculated accurately. For example, the following exponential index distribution is assumed [47],

$$n(x) = n_s + \Delta n \exp(-x / w), \quad x > 0; \quad = n_c, \quad x < 0 \tag{6.5}$$

where $n_s = 2.177$, $\Delta n = 0.09837$, w = 2.22726 μm, and $n_c = 1$. There are nine guided modes in this waveguides as shown in Figure 6.2. Through (6.4), it is found that there is an inverse error near $x = 0$. After using continuous effective index, through the general polynomial interpolation technique, the actual refractive index distribution is recovered exactly.

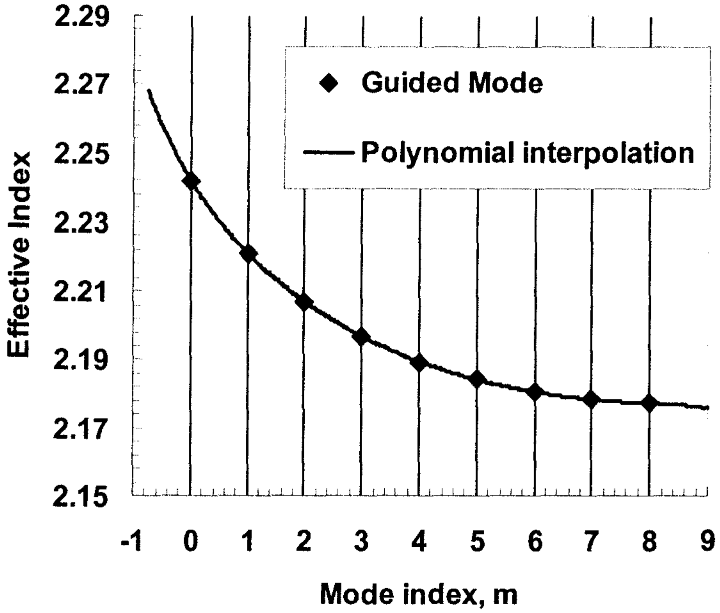

(a) Modal effective index

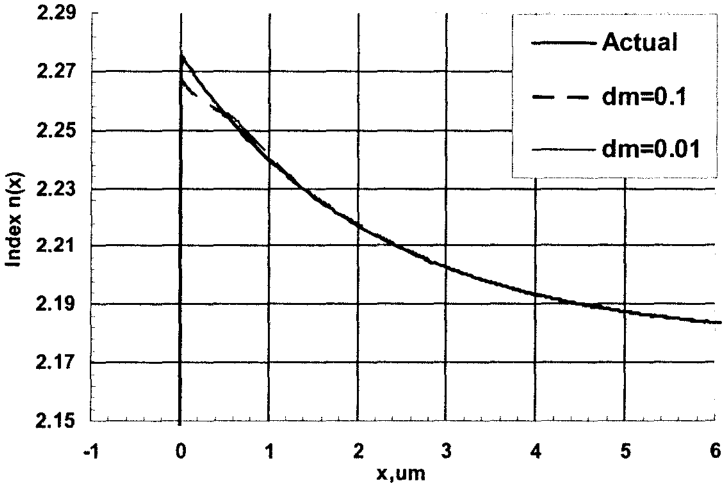

(b) Refractive index distribution

Figure 6.2 Refractive index distribution of optical graded waveguides

6.1.2 Direct reserve method based on near-field mode profile

The direct propagation-mode near-field method estimates the refractive index distribution in the optical waveguide from its mode field intensity by an inversion of the scalar wave equation directly. It requires no a priori knowledge of the shape of the refractive index distribution, and does not require the waveguide to have any kind of cross sectional symmetry. Due to the nature of the direct inversion, this technique requires that the waveguide is weakly guiding and only the fundamental mode of propagation is excited.

For weakly guiding waveguide, the optical field strength *E*(x,y) is described by the scalar wave equation of , which is rewritten as follows,

$$\nabla_T^{\,2} E(x,y) + \left\lfloor k^2(n^2(x,y) - n_{eff}^{\;2}) \right\rfloor E(x,y) = 0 \qquad (6.6)$$

where ∇_T (i.e., $\hat{y}\partial/\partial y + \hat{x}\partial/\partial x$) is the transverse gradient operator , *k*(i.e., *ω/c*) is the propagation constant in free space, and n_{eff} is the effective index. By rearranging the above equation of (6.6), we have [50],

$$n^2(x,y) = \frac{\beta^2}{k^2} - \frac{1}{k^2}\frac{\nabla_T^{\,2} E(x,y)}{E(x,y)} \qquad (6.7)$$

where $\beta = kn_{eff}$ is the propagation constant of the guiding mode. By assuming that *n*(x,y) = $n_s + \Delta n$(x,y),or n^2(x,y) ≈ $n^2_s + 2n_s\Delta n$(x,y), where n_s is the substrate index of the optical waveguide. By making the substitution for near-field intensity *I*(x,y) = E^2(x,y), we get

$$\begin{aligned} \Delta n(x,y) &= \frac{\beta^2}{2n_s k^2} - \frac{n_s}{2} - \frac{1}{2n_s k^2}\frac{\nabla_T^{\,2} E(x,y)}{E(x,y)} \\ &= \left(\frac{\beta^2}{2n_s k^2} - \frac{n_s}{2}\right) - \frac{1}{2n_s k^2}\frac{\nabla_T^{\,2}\sqrt{I(x,y)}}{\sqrt{I(x,y)}} \end{aligned} \qquad (6.8)$$

where the first two terms on the right-hand side of (6.8) are an unknown constant and expressed by C_0, which represent the refractive index away from the waveguide core to the substrate. By moving this constant term to the left-hand side of (6.8), we obtain

$$\Delta n(x,y) - C_0 = -\frac{1}{2n_s k^2}\frac{\nabla_T^{\,2} E(x,y)}{E(x,y)} = -\frac{1}{2n_s k^2}\frac{\nabla_T^{\,2}\sqrt{I(x,y)}}{\sqrt{I(x,y)}} \qquad (6.9)$$

The refractive index profile of the optical waveguide can be determined based on the measured near-field modal profile through utilizing the finite difference method. For example, for the sake of simplicity, with uniform mesh, the right-hand term of (6.9) has

$$\frac{\nabla_T^2 E(x,y)}{E(x,y)} = \frac{E_{i-1,j} + E_{i+1,j} - 2E_{i,j}}{\Delta x^2 E_{i,j}} + \frac{E_{i,j-1} + E_{i,j+1} - 2E_{i,j}}{\Delta y^2 E_{i,j}} \tag{6.10}$$

where $E(x,y) = E_{i,j}$ at corresponding positions x_i, y_j where $x_i = i\,\Delta x$, $y_j = j\,\Delta y$, and Δx, Δy are the mesh sizes along *x*, *y*, respectively. As long as the derivative term of (6.10) is calculated numerically, the refractive index distribution of the optical waveguide can be calculated from the intensity pattern of the mode profile if the constant term C_0 is measured.

From (6.9), it is found that the calculated index profile *n*(x,y) depends on the second derivative of the measured data *I*(x,y) through the inverse scalar wave equation process. In order to reconstruct the index profile *n*(x,y), the original data must have high signal-to-noise ratio (SNR) with minimum of very-high spatial frequency noise in the measured image and high resolution of the optical components of the image-detecting setup. The image noise may be introduced by misalignment of the equipments, electronic noise, quantization noise in conversion process, vibrations, and defocusing. Some of these sources may be reduced by the accurate instrument setup, taking multiple time-averaging tests, and numerical filtering techniques. In order to maximize the SNR of the intensity data *I*(x,y), the measuring system needs high quality equipments such as 12-bit CCD digital data and the optimum measurement conditions such as low operating current of laser diode and long CCD exposed time. However, due to the diffraction effects on light waves passing through an aperture, such as the objective of a microscope or a focusing lens, the problem represented from the limited resolving power of optics cannot be overcome thoroughly. On the other hand, some digital signal processing (DSP) techniques such as low-pass filter technique and neighbor averaging technique are used to further increase the SNR of the intensity data *I*(x,y).

For the neighbor averaging technique, the measuring intensity data is smoothing before the data processing through the nearest neighbor averaging technique with window width *w*(even number),

$$B_i = \begin{cases} \frac{1}{w}\sum_{j=0}^{w-1} E_{i+j-w/2}, & i = w/2,\dots,N-w/2 \\ E_i, & otherwise \end{cases} \tag{6.11}$$

where N is the number element in the array. The large size of the averaging window was chosen as long as it is below the optical resolution limit of the measuring system. In order to increase the SNR of the intensity data, the measured data are also averaged among repeating measurements up to ten.

For the low-pass filter technique, there are the following low-pass filter functions, where x is the distance from the origin, c is the cut-off value, and n defines the steepness or order of the function:

1. Ideal filter with a square cutoff function;
2. Butterworth filter with a maximally flat amplitude response defined by $1/[1+(x/c)^{2n}]$; For example, $c = 2$ μm and $n = 2$;
3. Chebyshev with an equiripple amplitude response in the passband
4. Cauer filter with an equiripple amplitude response in both passband and stopband defined by
5. Filter with an exponential cutoff function defined by $\exp[-(x/c)^n]$;
6. Finite impulse response digital filter with cutoff c and order n in the same range as others.

The digital filter procedure contains three steps:

1. Applying 1D or 2D FFT to the measued data $A(x,y)$ into $A(K_x, K_y)$.
2. Multiplying $A(K_x, K_y)$ by the low-pass filter amplitude response $H(K_x, K_y)$ such that more than 99% of signal power is within passband: $B(K_x, K_y) = A(K_x, K_y) H(K_x, K_y)$.
3. Applying 1D or 2D IFFT of $B(K_x, K_y)$ to $B(x,y)$ in the spatial domain.

In order to apply the FFT, we needs uniform mesh.

A systematical analysis of different errors such as noise, quantization, diffraction, defocusing, and nonlinearities in a real measurement setup is done in Ref [46]. Among them, the simulation error due to the noise has the largest value and is about 20% ~ 26%

when measuring typical LiNbO3 waveguide [46]. For example, a Gaussian index distribution is assumed as follows,

$$n(x) = n_s + \Delta n \exp(-(x/w)^2), \quad x > 0; \quad = n_c, \quad x < 0 \qquad (6.12)$$

where $n_s = 2.2$, w = 6.0 μm, and $n_c = 1$. Four different index differences: 5x10^{-4}, 1x10^{-3}, 3x10^{-3}, 5x10^{-3} are assumed. There exists single guided mode in this waveguides when $\Delta n < 3\text{x}10^{-3}$ as shown in Table 6.1. Figure 6.3 shows the corresponding refractive index and intensity distribution of optical graded waveguides. Figure 6.4 show the reverse the refractive index with limited mesh size and noise. From Figure 6.4, it is found that the direct reverse method based on near-field mode profile is inherently sensitive to noise and image distortion.

Table 6.1 Modal properties of assumed graded optical waveguide

Δn	5x10^{-4}	1x10^{-3}	3x10^{-3}	5x10^{-3}
n_{eff}	2.2030982158	2.2033748478	2.2048271900 2.2036129977	2.2064536585 2.2047166442
C_0 in (6.9)	9.7x10^{-5}	3.68x10^{-4}	1.826x10^{-3}	3.454x10^{-3}

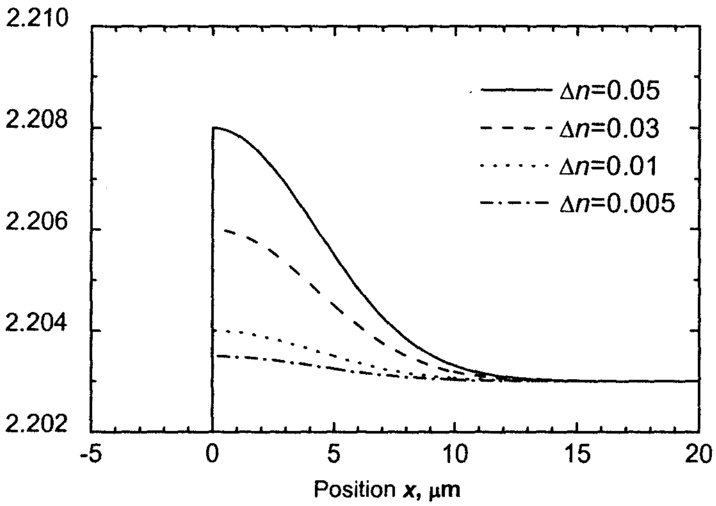

(a) Refractive index distribution

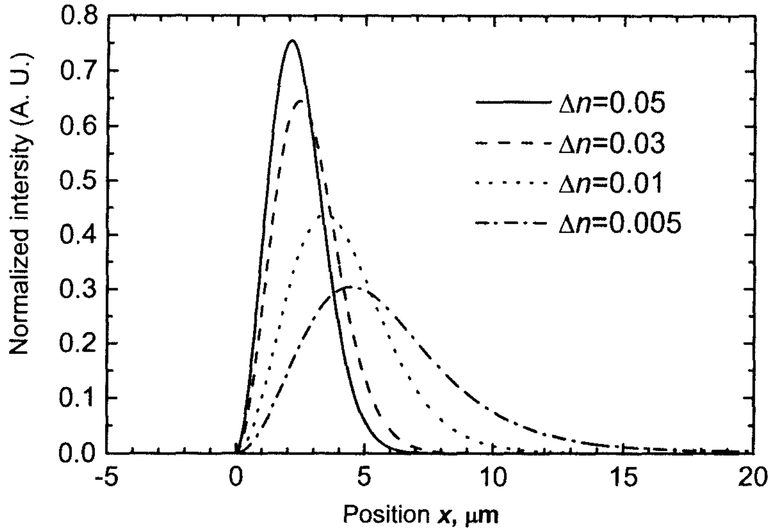

(b) Normalized intensity distribution

Figure 6.3 Refractive index and intensity distribution of optical graded waveguides

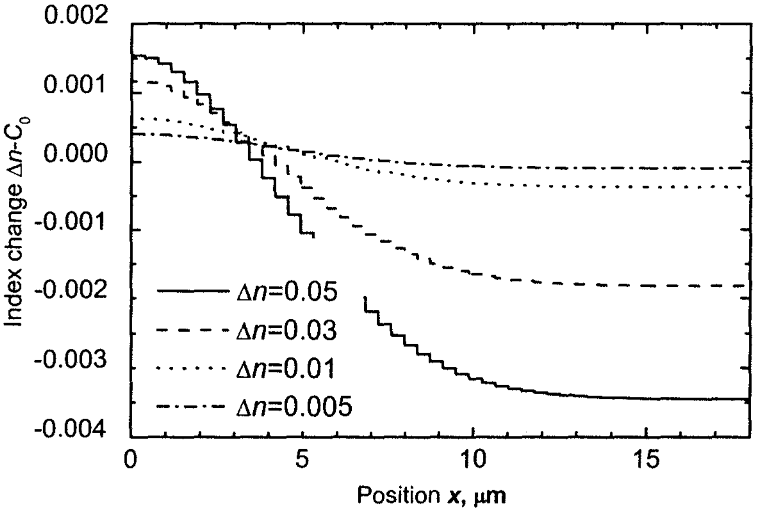

(a) Reverse index change with limited mesh size

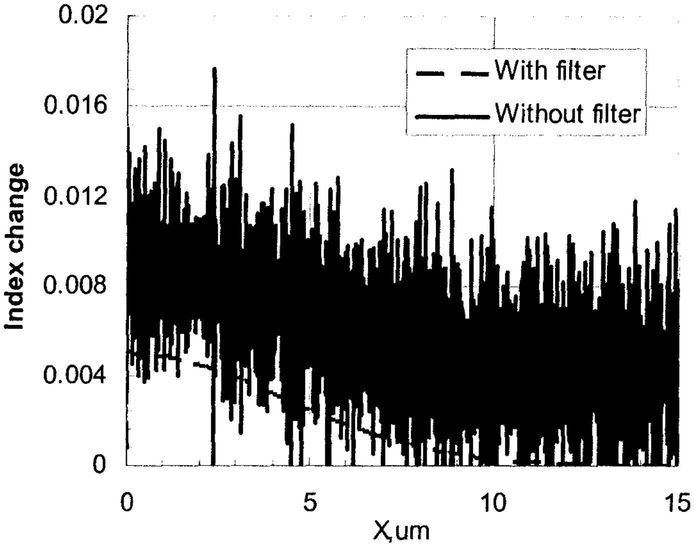

(b) Refractive index distribution for $\Delta n = 0.005$

Figure 6.4 Refractive index distribution of optical graded waveguides

6.1.3 Indirect iterative method based on near-field mode profile

As we know, quality of the calculated index profile $n(x,y)$ for the near-field direct method depends on the image noise, which consists of the very-high spatial frequency noise and resolution noise of the optical components of the image-detecting setup. As discussed in the previous chapter, some of these sources may be reduced. However, through the second-order derivation, the high spatial frequency noise components of the measured image are magnified by a factor of the order of κ^4, where κ is the spatial frequency. On the other hand, due to the diffraction effects on light waves passing through an aperture, such as the objective of a microscope or a focusing lens, the problem represented from the limited resolving power of optics cannot be overcame thoroughly.

In order to avoid the noise problems, an indirect method based on the search of the optimal index profile is proposed [52]. By comparing with measured modal profile, the best-fit numerical solution of the optical waveguide can be obtained through adjusting the waveguide parameters. The shape of the index profile and the initial values can be extracted from the detailed knowledge of the fabrication process of the waveguide or by secondary ion mass spectrometry (SIMS). The numerical solution of the waveguide profile can be calculated by the wave equation discussed in chapter 3. The Helmoltz equation of (3.6) can be written as an eigenvalue equation,

$$\nabla_T^{\,2} E(x,y) + \left[k^2 (n^2(x,y) - n_{eff}^{\,2})\right] E(x,y) = 0 \qquad (6.13)$$

where $n = n(x,y,a_1,a_2,\ldots,a_n)$, and $a_1,a_2,\ldots,a_n$ are design parameters about the maximum index variation, profile depth, and width, etc. For the eigen value problem, the FDM Algorithm discussed previously can be utilized,

$$\frac{(E_{i-1,j} + E_{i+1,j})}{\Delta x^2} + \left[(kn_{i,j})^2 - \frac{2}{\Delta x^2} - \frac{2}{\Delta y^2}\right] E_{i,j} + \frac{(E_{i,j-1} + E_{i,j+1})}{\Delta y^2} = (kn_{eff})^2 E_{i,j} \qquad (6.14)$$

where the uniform mesh sizes Δx , Δy are utilized for the sake of simplicity, and the corresponding electric modal profile E_c can be obtained.

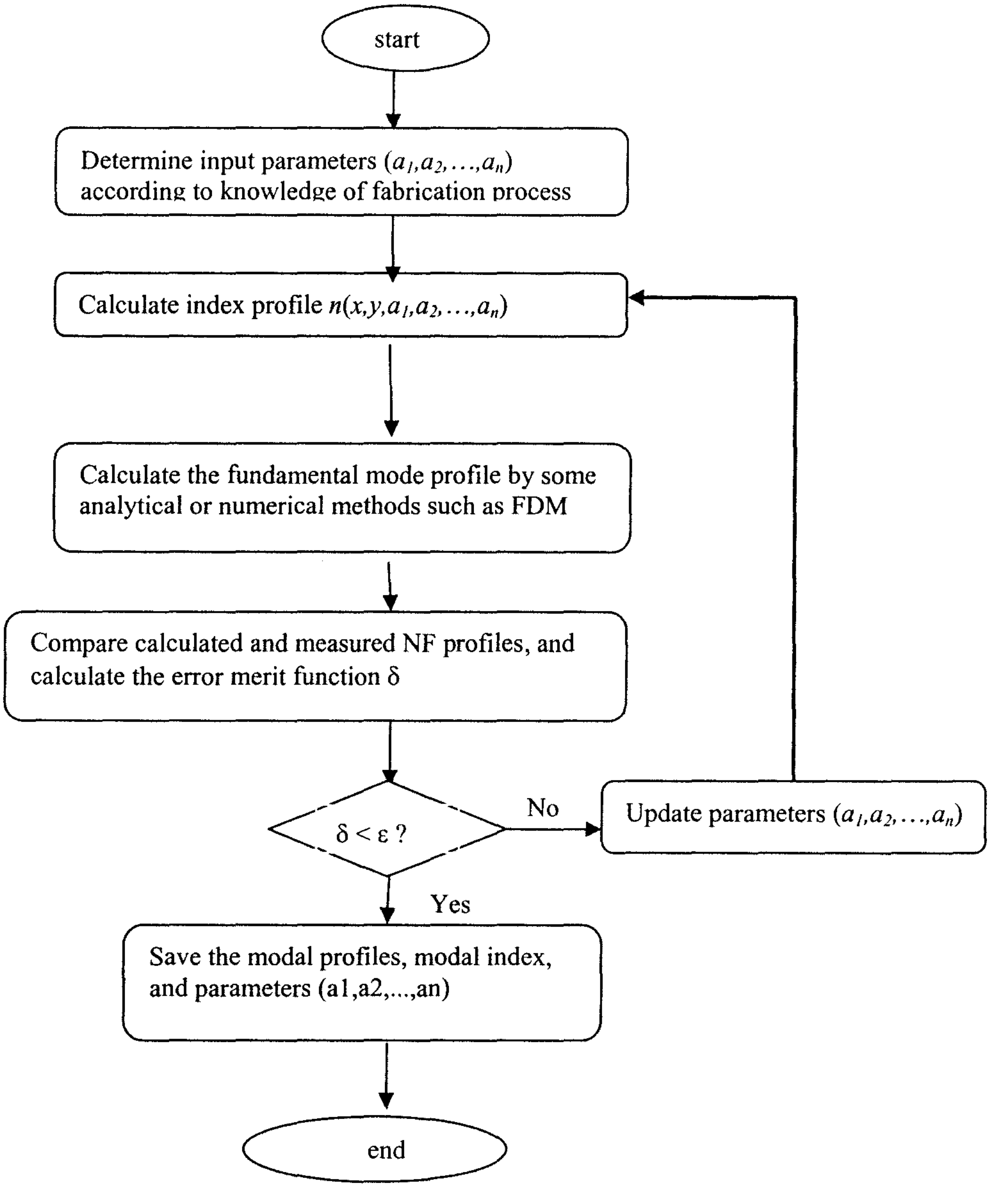

Figure 6.5 The flow chart of indirect method based on measured near-field profile

In order to minimize the difference between the measured near-field profile E_m and E_c, the error merit function is utilized,

$$\delta = \int \frac{|E_m - E_c|}{|E_c|} dxdy \tag{6.15}$$

where E_m and E_c are both normalized to their maximum value. Through some standard optimization packages, some optimal design parameters $a_1, a_2, \ldots, a_n$ can be obtained. The corresponding flow chart is shown in Figure 6.5. The advantage of the indirect method is the insensitivity of the method to the high spatial frequency noise due to the fact that the noise is averaged out by calculating the merit function. On the other hand, this indirect method suffers huge numerical work, especially for two-dimensional channel waveguides. Finally, the comparison of various direct and indirect reverse index methods is made in Table 6.2.

Table 6.2 Comparison of various direct and indirect reverse index methods

Method	Index profile in advance	sensitive to noise and image distortion	Efficiency
Direct method based on index (IWKB)	Yes	No	high
Indirect method based on index (FDM)	Yes	No	low
Direct method based on field	No	Yes	high
Indirect method based on field x (FDM)	Yes	No	low

6.2 Index Profile of Ti:LiNbO$_3$ Waveguides

By considering the nonlinearity of the video camera, the modal intensity I(x,y) can be obtained from the measured intensity I_m(x,y) of the video camera,

$$I(x,y) = I_m(x,y)^{1/\gamma} \tag{6.16}$$

where γ is the nonlinearity coefficient of the video camera. The normalized electric field intensity is calculated as

$$E(x,y) = \sqrt{fI(x,y)/I_{\max}} \tag{6.17}$$

By utilizing the measured modal profiles introduce in chapter 4, the index distributions of corresponding waveguides can be calculated. Several reverse methods are tried. The direct methods have large errors no matter what filtering methods are used.

Here the index distributions are calculated by the indirect iterative method based on measured near-field mode profiles.

For the *Z*-cut Ti:LiNbO$_3$ waveguides with T = 1050 °C, t = 4 hrs, τ = 0.11 μm, and argon flow, Figure 6.6 shows the measure results of near-fields with different widths w = 8, 9, 10 μm. Figure 6.7 shows the calculated index distribution of Z-cut Ti:LiNbO$_3$ optical waveguides. The best fitting is $\Delta n_{\max}$= 0.022, and corresponding fit error = 12.5%.

For the *Z*-cut Ti:LiNbO$_3$ waveguides with T = 1050 °C, t = 3 hrs, τ = 0.11 μm, and argon flow, Figure 6.8 shows the measure results of near-fields with different widths w = 9, 10 μm. Figure 6.9 shows the calculated index distribution of Z-cut Ti:LiNbO$_3$ optical waveguides. Again the best fitting is $\Delta n_{\max}$= 0.03, and corresponding fit error = 10.5%.

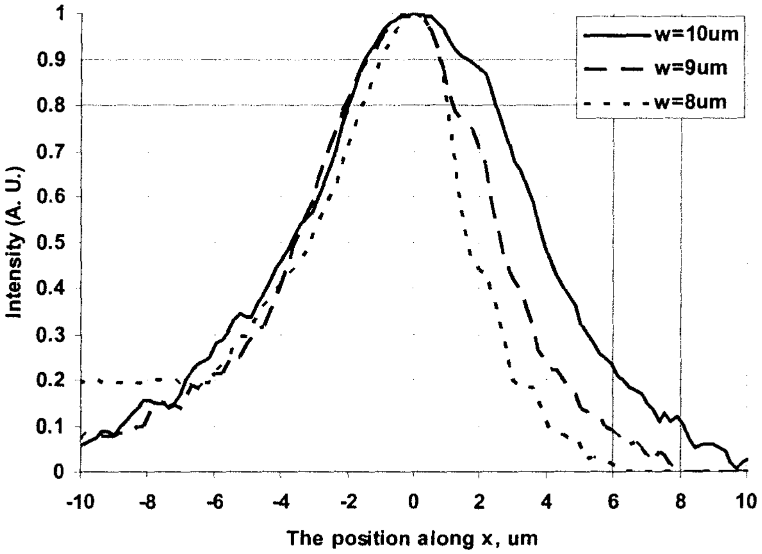

(a) Intensity distribution along x

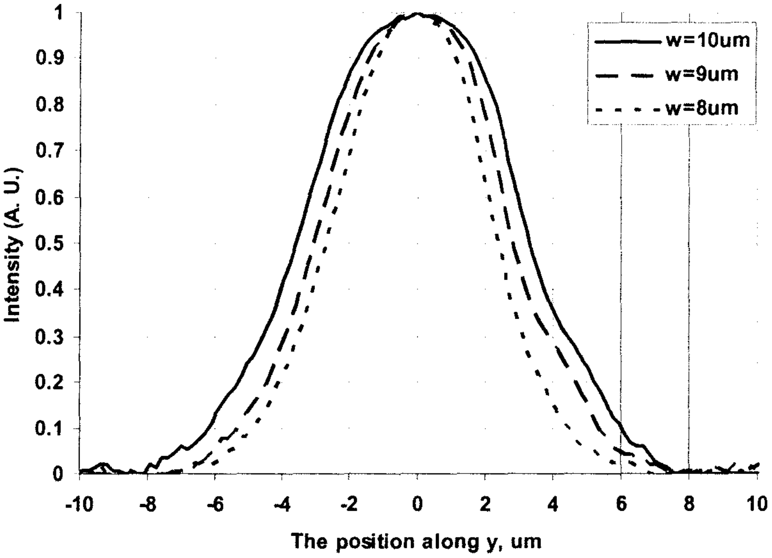

(b) Intensity distribution along *y*

Figure 6.6 Measured intensity distribution of Z-cut Ti:LiNbO3 optical waveguides with $T = 1050$ °C, $t = 4$ hrs, and $\tau = 0.11$ μm.

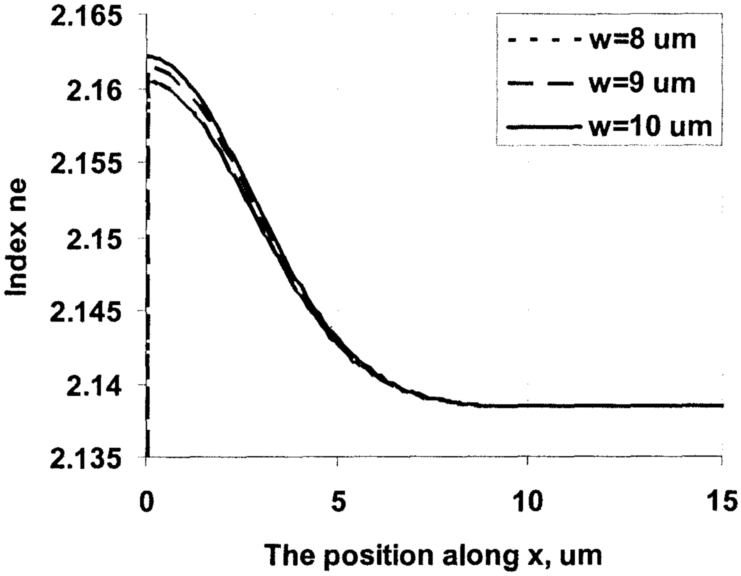

(a) Refractive index distribution along *x*

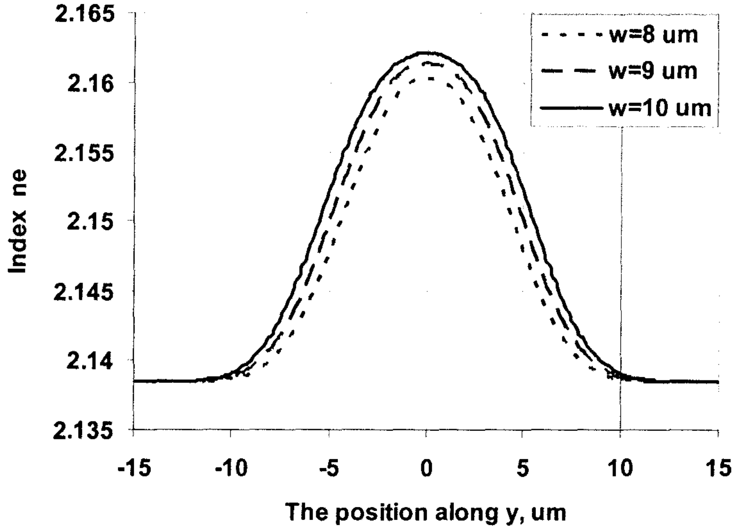

(b) Refractive index distribution along y

Figure 6.7 Index distribution of Z-cut Ti:LiNbO3 optical waveguides with T = 1050 °C, t = 4 hrs, and τ = 0.11 μm.

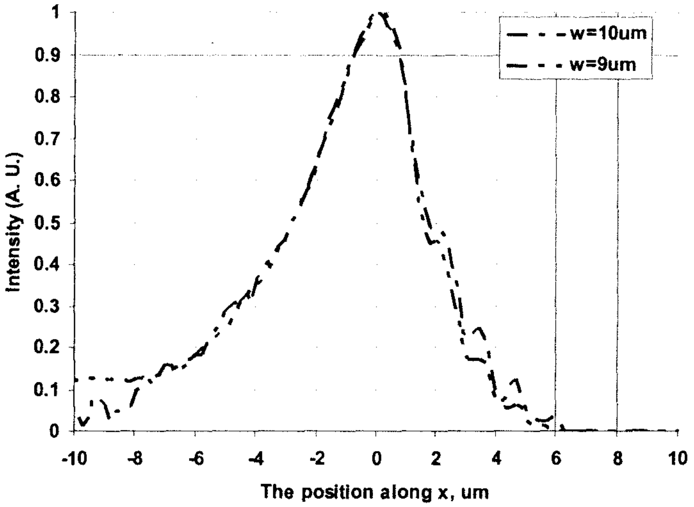

(a) Intensity distribution along x

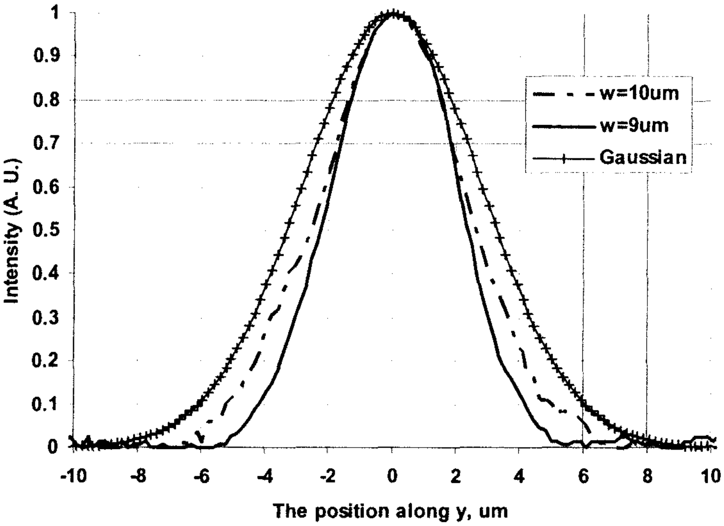

(b) Intensity distribution along *y*

Figure 6.8 Measured intensity distribution of Z-cut Ti:LiNbO$_3$ optical waveguides with $T = 1050$ °C, $t = 3$ hrs, and $\tau = 0.11$ μm.

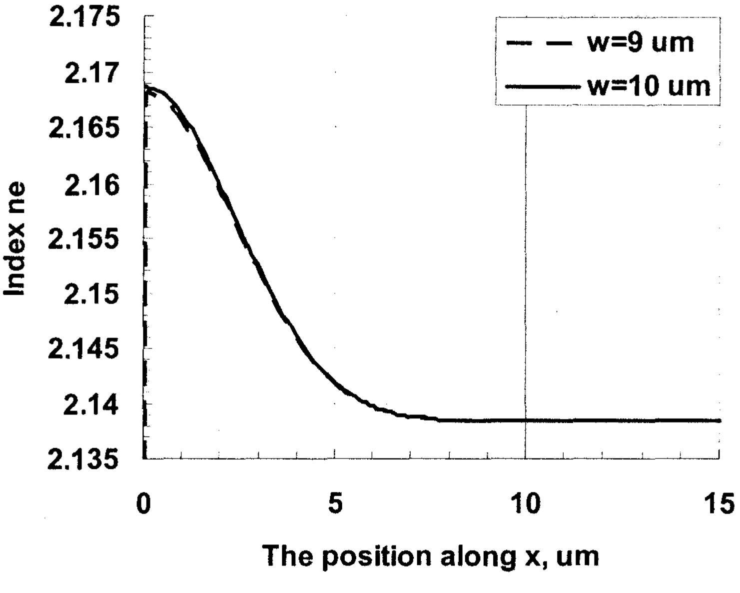

(a) Refractive index distribution along *x*

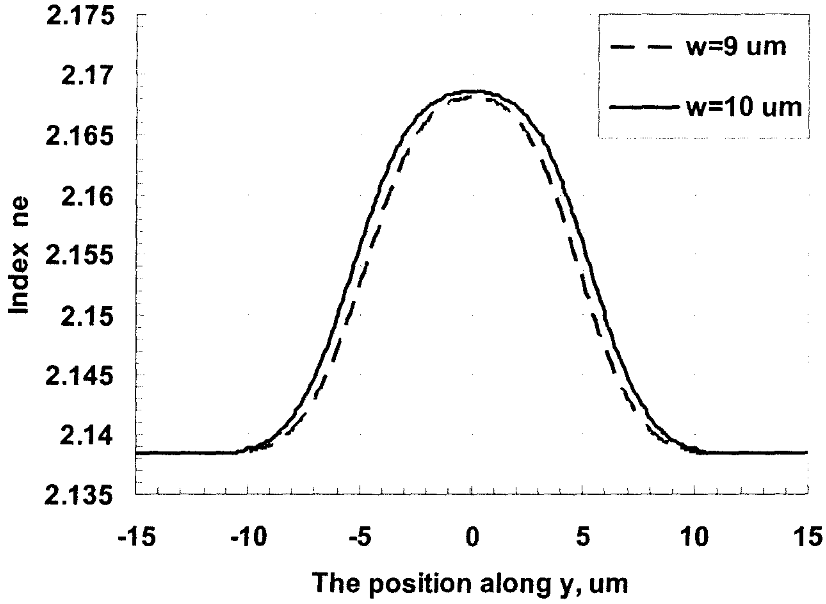

(b) Refractive index distribution along *y*

Figure 6.9 Index distribution of Z-cut Ti:LiNbO3 optical waveguides with $T = 1050$ °C, $t = 3$ hrs, and $\tau = 0.11$ μm.

6.3 Index Profile of APE LiNbO$_3$ Waveguides

In modeling of APE LiNbO$_3$ waveguides, a cosh^{-2} profile of the hydrogen concentration of (5.19) and an isotropic index distribution of (4.12) are utilized in Ref [45]. Here we utilize material and refractive index models discussed in chapter 5. By comparison the simulated near-field patterns with the measured patterns for various optical waveguides, the relationship between the parameter's value of model and fabrication condition can be obtained.

As discussed previously, a two-step method (i. e., proton-exchange and thermal annealing) is used in the modeling of APE LiNbO$_3$ optical waveguides. From (5.4) and (5.5), the PE exchanged depth $\tau = 0.77$ μm with $T_1 = 200$ °C and $t_1 = 1.92$ hrs. From (5.21), the extraordinary refractive index change $\Delta n_e = 0.093$ with $\lambda = 1.55$ μm. From (5.20), the refractive index profile $n_e(x, y, \lambda) = n_{eb} + \Delta n_e C(x, y)$ with $n_{eb} = 2.1372$, $\alpha_e = 1$, and $\lambda = 1.55$ μm, $n_o(x, y, \lambda) = n_{ob} = 2.20542$. Based on measured near-field mode profiles through the indirect iterative method, the index distributions of the APE waveguides can be calculated.

By comparing with the measured values of modal profiles, as shown in Figure 6.10, and the refractive index distribution can be calculated easily. Figure 6.11 shows the calculated index distributions of *Z*-cut APE LiNbO$_3$ waveguides. The corresponding diffusion coefficients and depths during the annealing process are calculated as shown in Table 6.3.

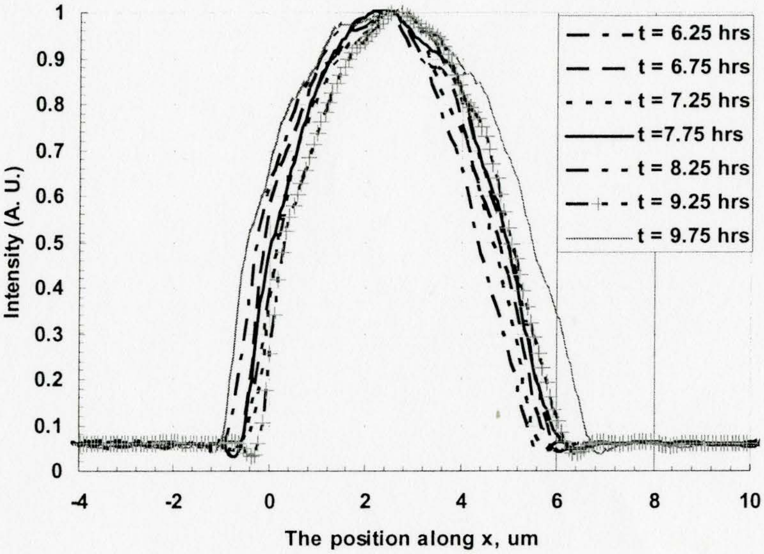

(a) Intensity distribution along *x*

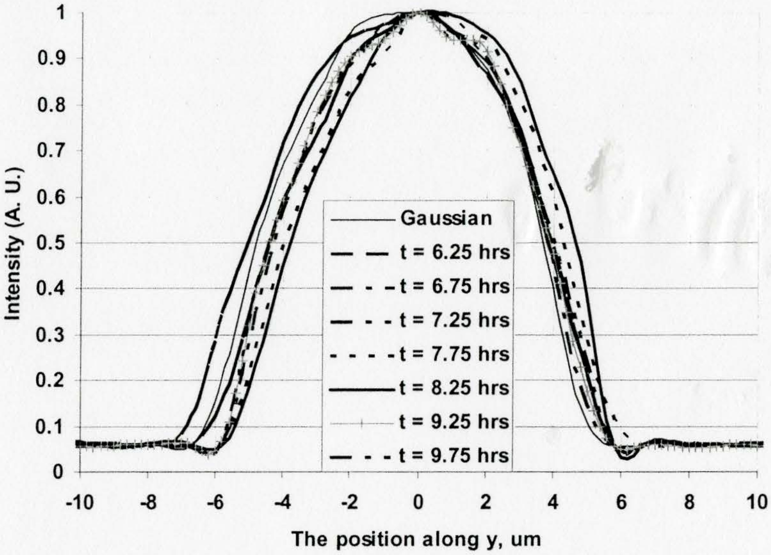

(b) Intensity distribution along *y*

Figure 6.10 Measured intensity distributions of Z-cut APE LiNbO$_3$ waveguides

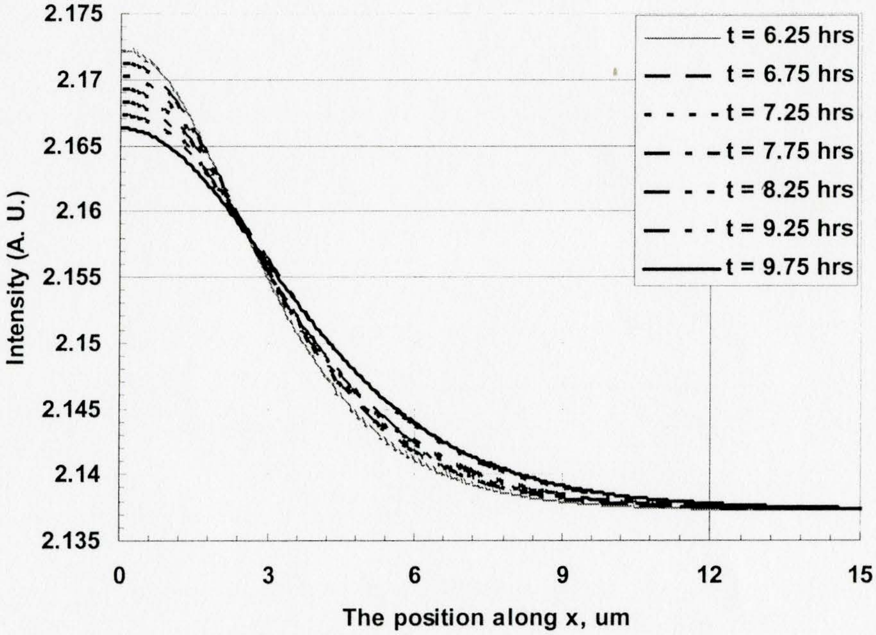

(a) Refractive index distribution along *x*

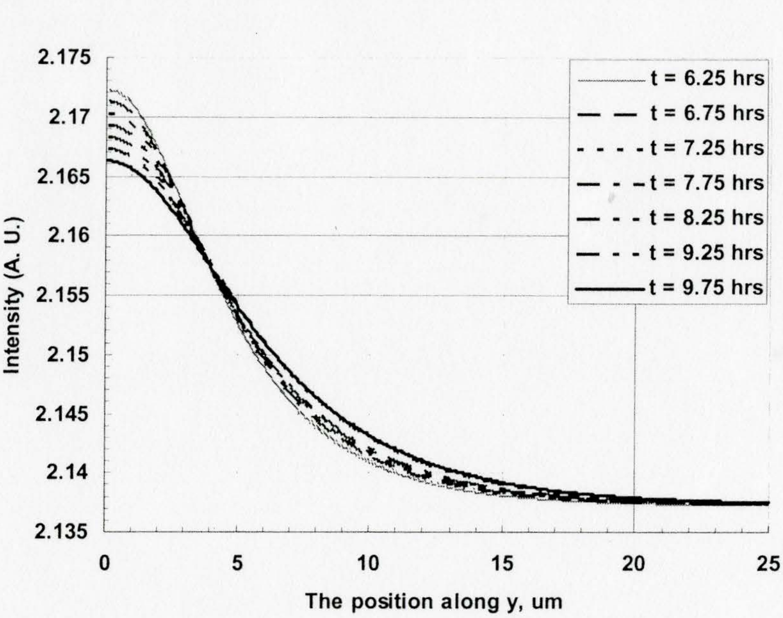

(b) Refractive index distribution along *y*

Figure 6.11 Simulated index distribution of *Z*-cut APE $LiNbO_3$ waveguides

Table 6.3 Diffusion coefficients and depths of APE in *Z*-cut $LiNbO_3$ waveguides

Sample	T(°C)	t(min)	t(h)	D_x, μm²/h	D_y, μm²/h	d_x, μm	d_y, μm
1	350	375	6.25	1.8225	1.5625	6.75	6.25
2	350	405	6.75	1.8828	1.5408	7.13	6.45
3	350	435	7.25	1.8628	1.5497	7.35	6.70
4	350	465	7.75	1.8632	1.5358	7.60	6.90
5	350	495	8.25	1.8436	2.6505	7.80	7.13
6	350	555	9.25	1.9527	1.5202	8.50	7.50
7	350	585	9.75	1.9631	1.5400	8.75	7.75

6.4 Summary

In this chapter, several indirect nondestructive methods, based on mode effective index and near-field mode profile, are introduced. Their advantages and disadvantages are discussed. By comparing with the measured results of modal profiles, the index distribution of Ti:$LiNbO_3$ and APE optical waveguides are obtained.

Chapter 7
Conclusions

In this thesis, the material properties and modal characteristics of the lithium niobate optical waveguides based on the titanium in-diffusion and annealed proton-exchange process are investigated thoroughly. By linking the relation of the design and fabrication parameters with modal properties of the $LiNbO_3$-based waveguides, a comparative study on modeling and characterization of diffused optical waveguides is presented.

First we investigate the material property of $LiNbO_3$-based optical waveguides. We start with the two-dimensional (2D) Fickian thermal diffusion equation for general diffusion process. Both analytical and numerical methods are introduced to solve the 2D diffusion equation. The accuracy and the scope of validity for the analytical methods and numerical methods with different solver settings are presented. Then the index model with relation of the species concentration is built and the index distribution of the $LiNbO_3$-based optical waveguides with considering different processes such as diffusion, exchange, and annealing can be calculated analytically and numerically. After understanding the physical insight of the diffused waveguides, some important fabrication and design parameters are abstracted and used for calculating the index distribution of the optical waveguides. In addition, the different models of the refractive indices of ordinary and extraordinary n_o and n_e of the bulk $LiNbO_3$ crystal are investigated.

Then, by applying a rigorous finite difference method, the modal properties of the diffused waveguides, such as modal profile, effective index, and coupling loss with the standard fiber, can be calculated. In order to understand the physical insight of the diffused waveguides, the analytical methods such as WKB method are also introduced. The modal properties of the optical waveguides are directly linked to the fabrication parameters of corresponding waveguides. Based on modal properties of optimized waveguides, the device performances of the related devices can be easily obtained.

Based on the analysis of general $LiNbO_3$ optical waveguides, the detail material and modal properties of the titanium in-diffusion and annealed proton-exchange $LiNbO_3$ optical waveguides are further investigated. Their fabrication processes are reviewed and typical process parameters are given. Through comparing different models of index change with concentration of the related species such as titanium and hydrogen, the material properties can be calibrated. Furthermore, by comparing with measurement results of the titanium in-diffusion and annealed proton-exchange $LiNbO_3$ optical waveguides made in McMaster University, the relation between the waveguide modal performance and design parameters is built through some effective methods and ready to be applied in the design of optical devices.

Finally, we reconstruct the refractive index distribution of the optical waveguides by using the measurement results of modal properties such as mode profile and effective index.

Appendix A

Lithium Niobate and Types of Cuts

The crystalline lithium niobate ($LiNbO_3$) is one of important waveguide materials for modern optoelectronic device applications. Due to several profound physical properties such as low loss, large electro-optic coefficient, and high second-order nonlinearity, $LiNbO_3$ has found to be intensively used in many areas of guided-wave devices such as optical modulation, optical switching and filtering, signal processing, mode splitting, and wavelength conversion.

A.1 Lithium Niobate

Lithium Niobate ($LiNbO_3$) is a synthetic single crystal oxide material and has a transparency wavelength range from 0.33 to 5.5 μm. In general, $LiNbO_3$ is a negative uniaxial crystal (i. e., $n_o > n_e$, where n_o and n_e are ordinary index and extraordinary refractive index of the media, respectively). Mathematically, according to the definition of media refractive index in section 1.1, its relative dielectric constant $\vec{\varepsilon}_r$ can be described in tensor format,

$$\vec{\varepsilon}_r = \begin{bmatrix} n_X^2 & 0 & 0 \\ 0 & n_Y^2 & 0 \\ 0 & 0 & n_Z^2 \end{bmatrix} = \begin{bmatrix} n_o^2 & 0 & 0 \\ 0 & n_o^2 & 0 \\ 0 & 0 & n_e^2 \end{bmatrix} \tag{A.1}$$

where X, Y, Z are the crystal axes and n_o, n_e are ordinary and extraordinary indices, respectively. With the uniaxial crystal property of $LiNbO_3$, we have $n_X = n_Y$ (i. e., n_o) $\neq n_Z$ (i. e., n_e), or $n_X = n_Y = n_o$ and $n_Z = n_e$.

A.2 Types of Cuts

Normally, the guided-wave devices are realized based on the crystal wafer. In order to express the dielectric constant tensor explicitly of the wafer substrate, a suitable coordinate system needs to be determined as well. As discussed in chapter 1, Figure A.1

shows the corresponding coordinate system, where the *x*-*y* plane defines the cross-section of the waveguide and the axis *z* defines the wave propagation direction.

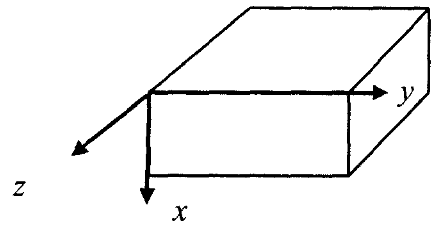

Figure A.1 Schematic view of optical waveguide coordinate system

According to different crystal orientation cuts defined by the axis *x* (normal to the wafer facet) and propagation directions defined the axis *z*, there are six possible orientations of $LiNbO_3$ crystal in optical diffused waveguides as shown in Figure A.2. In other words, if the crystal orientation X (or Y, Z) is normal to the wafer facet plane, the wafer is said to X-cut (or Y-cut, Z-cut).

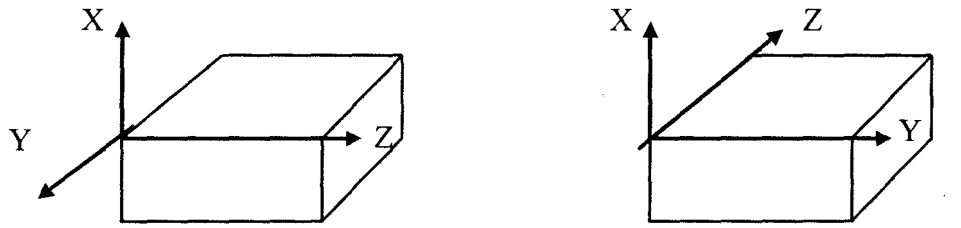

(a) X-Cut and Y-Propagation

(b) X-Cut and Z-Propagation

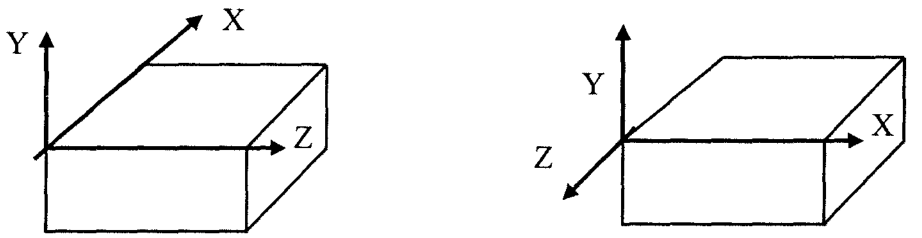

(c) Y-Cut and X-Propagation

(d) Y-Cut and Z-Propagation

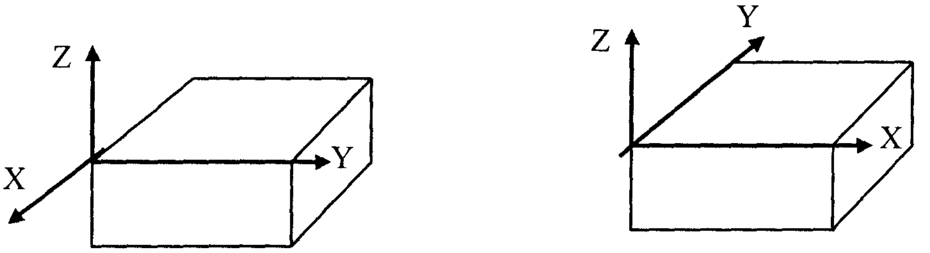

(e) Z-Cut and X-Propagation (f) Z-Cut and Y-Propagation

Figure A.2 Schematic view of possible orientations of $LiNbO_3$ crystal

In the current coordinate system defined in Figure A.1, by comparing with the crystal axis as shown in Figure A.2, for instances, the relative dielectric constants $\vec{\varepsilon}_r$ for Z-Cut and Y-Cut have the following forms,

$$\vec{\varepsilon}_r = \begin{bmatrix} n_x^2 & 0 & 0 \\ 0 & n_y^2 & 0 \\ 0 & 0 & n_z^2 \end{bmatrix} = \begin{bmatrix} n_e^2 & 0 & 0 \\ 0 & n_o^2 & 0 \\ 0 & 0 & n_o^2 \end{bmatrix} \quad \text{for Z-Cut} \qquad \text{(A.2)}$$

$$\vec{\varepsilon}_r = \begin{bmatrix} n_o^2 & 0 & 0 \\ 0 & n_e^2 & 0 \\ 0 & 0 & n_o^2 \end{bmatrix} \quad \text{for Y-Cut and X-Propagation} \qquad \text{(A.3)}$$

$$\vec{\varepsilon}_r = \begin{bmatrix} n_o^2 & 0 & 0 \\ 0 & n_o^2 & 0 \\ 0 & 0 & n_e^2 \end{bmatrix} \quad \text{for Y-Cut and Z-Propagation} \qquad \text{(A.4)}$$

where n_o and n_e are ordinary and extraordinary refractive indices, respectively. The detail relations between crystal axes and waveguide coordinate system are summarized in Table A.1.

Table A.1 The relations between crystal axes and waveguide coordinate system

Relation between crystal axes and waveguide coordinate	n_x	n_y	n_z	Configuration
Z-axis || x	n_e	n_o	n_o	Z-Cut, and X/Y-Propagate
Z-axis || y	n_o	n_e	n_o	X-Cut, and Y-Propagate Y-Cut, and X -Propagate
Z-axis || z	n_o	n_o	n_e	X/Y-Cut, and Z-Propagate

Appendix B

$LiNbO_3$ Waveguide Fabrication Technologies

As mentioned previously, titanium in-diffusion and proton exchange have become the most important fabrication techniques for the $LiNbO_3$-based optical waveguides. In this appendix, some major features of those two fabrication techniques are discussed.

B.1 Titanium In-diffusion Optical Waveguide

Titanium in-diffusion technique is one of the most widespread and well-established techniques for fabrication of optical waveguide based on $LiNbO_3$ substrate. For the $LiNbO_3$ waveguides based on titanium in-diffusion, there are two typical fabrication processes as shown in Figure B.1. In general, the former is called the lift off method and the later is the etching method.

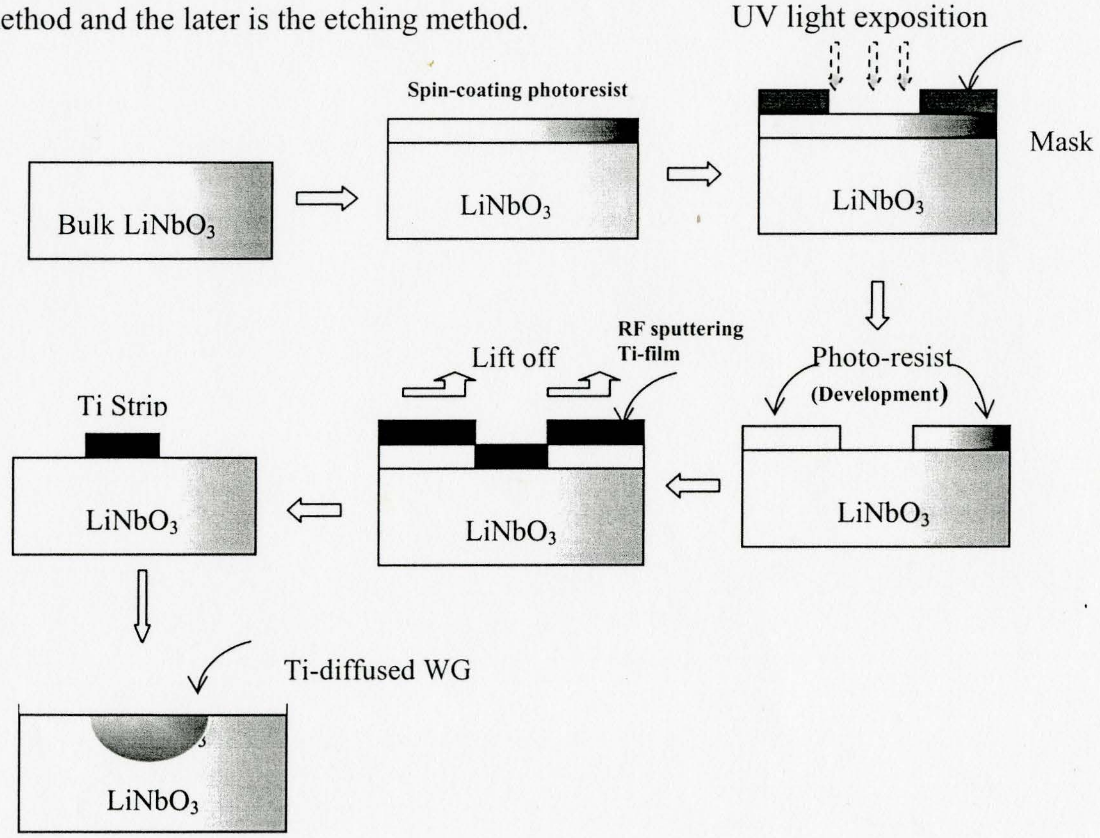

(a) The Lift off method for $Ti:LiNbO_3$ optical waveguide

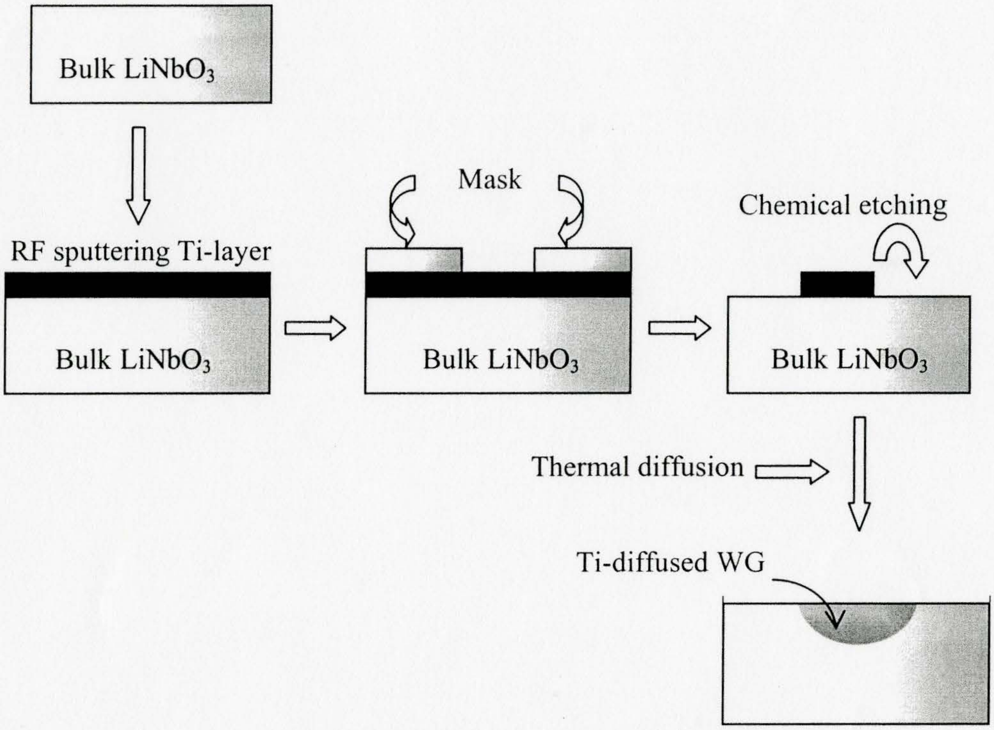

(b) The Etching method for $Ti:LiNbO_3$ optical waveguide

Figure B.1 Fabrication techniques of $Ti:LiNbO_3$ optical waveguides

In order to realize the optical waveguide on $LiNbO_3$ wafer, the main steps of the fabrication techniques of $Ti:LiNbO_3$ optical waveguides, as shown in Figure B.1, are summarized as followings:

1. Clean the polished bulk $LiNbO_3$ wafer carefully.
2. Deposit the patterning photo-resist for the lift off method or the Ti layer for the etching method.
3. Deposit the Ti layer for the lift off method or set photolithographic mask for the etching method.
4. Pattern the Ti stripe by using lift-off or etching techniques.
5. Put the $LiNbO_3$ wafer at a high temperature environment of 950-1100°C with flowing gas (e. g., oxygen, argon, or air) for high temperature diffusion.

6. Spin-on buffer layer (e. g., SiO_2) for some applications such as modulators.
7. Cut the wafer into small pieces and polish the waveguide for testing.

Some typical fabrication conditions for $Ti:LiNbO_3$ waveguides are shown in Table B.1.

Table B.1 Fabrication conditions of some examples of z-cut $Ti:LiNbO_3$ substrate.

Year[Ref]	Wavelength, λ(μm)	Ti thickness, τ(μm)	Diffusion temperature, T(°C)	Diffusion time, t(h)	Environment A
1974 [23]	0.633	0.05	960	6	
1978 [29]	0.633	0.04	950-1050	5	
1979 [27]	1.15	0.05	1000	10	
1980 [30]	1.15	0.05	1000,1030,1050	5	Dry air
1987 [16]	0.633-1.523	0.03-0.21	1000-1050	9	Dry O_2 /Ar

B.2 Annealed Proton-Exchang Waveguide

As we discussed previously, annealed proton-exchanged (APE) process on the $LiNbO_3$ wafer is an effective technique for formation of low loss and high index difference optical waveguides. In this technique, whole fabrication procedure is divided into three major processes: a photolithography process, the proton-exchange (PE) process, and the annealing process. Figure B.2 shows the typical fabrication procedure of the APE $LiNbO_3$ waveguide.

As the first step of the APE process, a photolithography process is needed to define the waveguide channels. In this stage, waveguide channel layout is patterning on the $LiNbO_3$ wafer through a single-step photolithographic processing by using 1-μm thickness positive photo-resist. A mask film, made by chromium, aluminum, or SiO_2, is deposited and lifted off for the PE opening. Then the whole wafer is cut into small pieces of samples by using a diamond blade dicing machine for the PE process.

In the PE process, the dicing $LiNbO_3$ wafer is put into the liquid such as benzoic or pyrophosphoric acid at a low fixed temperature (150-250°C). Hydrogen atoms in the liquid are exchanged with lithium (Li) atoms of the $LiNbO_3$ wafer, which leads to a large increase in the extraordinary refractive index and a slightly decrease in the ordinary refractive index. Because the rate of proton diffusing in is much less than that of the lithium ions diffusing out, the index distribution of the $LiNbO_3$ wafer after the PE process is a step-like function with certain compositional instabilities in the exchanged layer. After the immersion of a certain PE exchange time, the $LiNbO_3$ samples are allowed to cool down and then the mask is removed for the annealing process.

In order to eliminate compositional instabilities in the exchanged layer and to restore desirable optical properties such as the large electro-optical coefficients, a thermal annealing process is required at a higher temperature (350°C) in a longer period of time (several hours). The graded hydrogen profile, with lower concentration, extends far deeper than the original exchange depth. The highly graded profile of the extraordinary refractive index in the PE layer is strongly dependent upon the annealing procedures such as temperature, time, and annealing atmosphere. Finally, two ends of the waveguide need to be polished. Some typical fabrication conditions for APE $LiNbO_3$ waveguides are shown in Table B.2.

Table B.2 Fabrication conditions of some examples of Z-cut APE $LiNbO_3$ substrate. The proton source is benzoic acid.

Years	λ(μm)	W (μm)	Mask film	Proton exchange		Annealing		
				T_1(°C)	t_1(min)	Gas	T(°C)	t(min)
04[45]	1.55	6	Cr	200	115	air	350	375, 405, 435, 465, 495, 555, 585
89	0.82	3	Al	200	20	oxygen	350	180
99	1.5	3.5	Al	200	90	oxygen	350	240
93	1.5	10	Cr	200	60	wet oxygen	350	60
91	2.1	2-15	Al	200	120	air	333	720

Note: W--width of mask opening, T_1--PE temperature, t_1--proton-exchange duration, T--annealing temperature, t--annealing duration

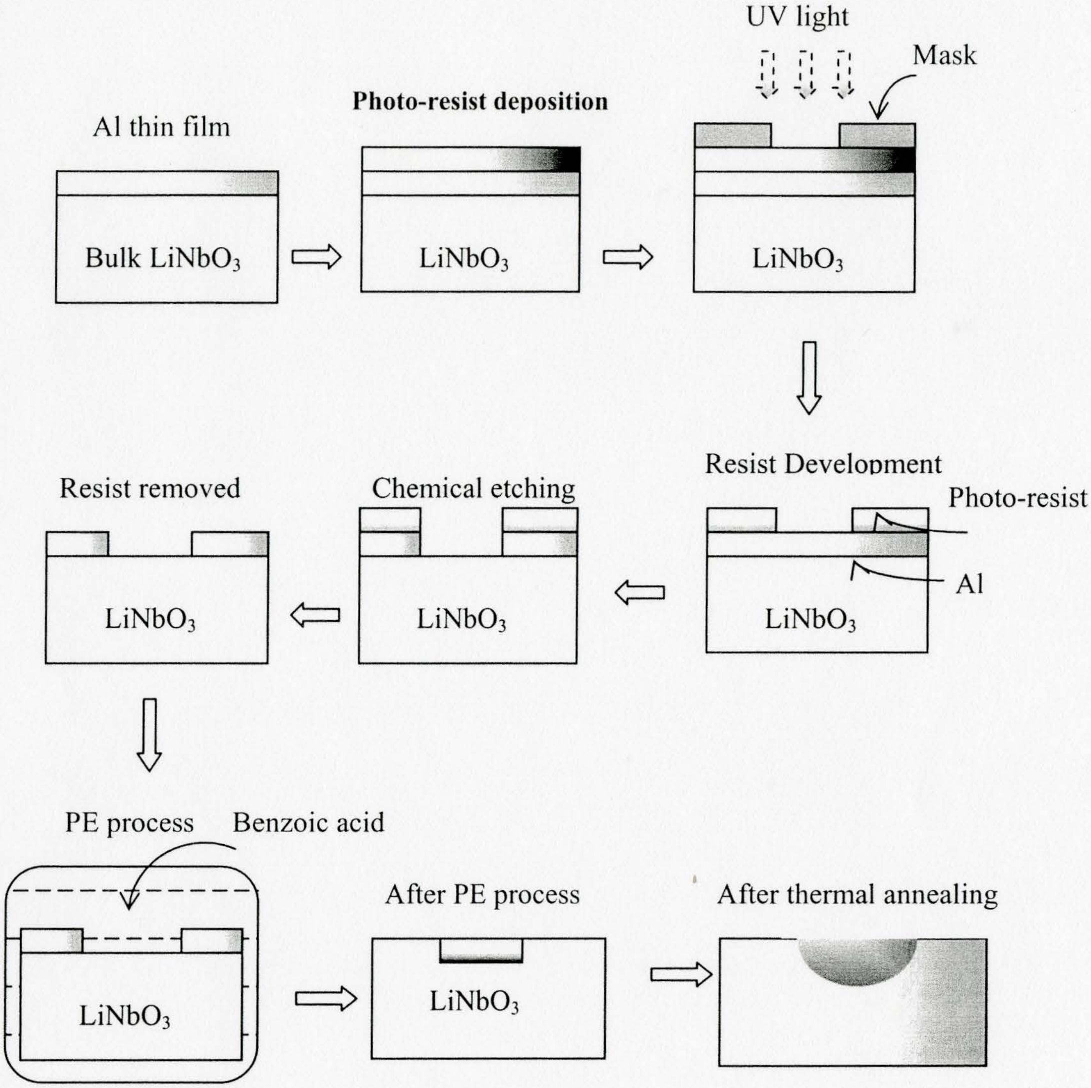

Figure B.2 The fabrication procedure of an APE LiNbO$_3$ waveguide

B.3 Comparison Between Ti:LiNbO$_3$ and APE Waveguides

Through comprehensive analysis of previous chapters, the typical design parameters and modal properties of the Ti:LiNbO$_3$ and APE LiNbO$_3$ waveguides related to the Ti in-diffusion, proton exchange and thermal annealing process are summarized in Table B.3.

Table B.3 Comparison between Ti:$LiNbO_3$ and APE $LiNbO_3$ waveguides

Parameters	Ti indiffusion	Proton exchange	Thermal annealing
Crystal cuts	Y and Z	X and Z	X and Z
Temperature T, °C	High (890~1100)	Low (120~250)	Mediate (300 ~ 400)
Time t, hour	Long (4~10)	Short (0.3~2.0)	Mediate (2 ~ 9)
Index change Δn	Small (10^{-2} ~ 10^{-3})	Large(0.1~ 0.14) of Δn_e Negative(-0.04) of Δn_o	Mediate (10^{-1} ~ 10^{-2}) of Δn_e, negative of Δn_o
Supporting modes	TE and TM	TE or TM	TE or TM
Loss, dB/cm	Small (0.5~ 1.0)	high (1.0~ 1.5)	Small (0.5~ 1.0)
Photorefractive	high	Mediate	Low

Appendix C

Error Function and Law of Conservation of the Matter

C.1 Error Function

The error function *erf*(*x*) and its complementary error function *erfc*(*x*) are defined as follows [15],

$$erf(x) = \frac{2}{\sqrt{\pi}} \int_0^x \exp(-u^2) du \qquad \text{(C.1)}$$

$$erfc(x) = \frac{2}{\sqrt{\pi}} \int_x^\infty \exp(-u^2) du \qquad \text{(C.2)}$$

where x is a real variable and $erf(x) + erfc(x) = 1$. The error functions have the following limit values and symmetry properties,

$$erf(0) = erfc(\infty) = 0,\ erf(\infty) = erfc(0) = 1 \qquad \text{(C.3)}$$

$$efr(-x) = -\ erf(x),\ efrc(-x) = 1 - erf(-x) = 1 + erf(x) \qquad \text{(C.4)}$$

As shown in Figure C.1, the values of error function *erf*(*x*) are within [-1, 1] and its complementary error function *erfc*(*x*) belongs to [0, 2].

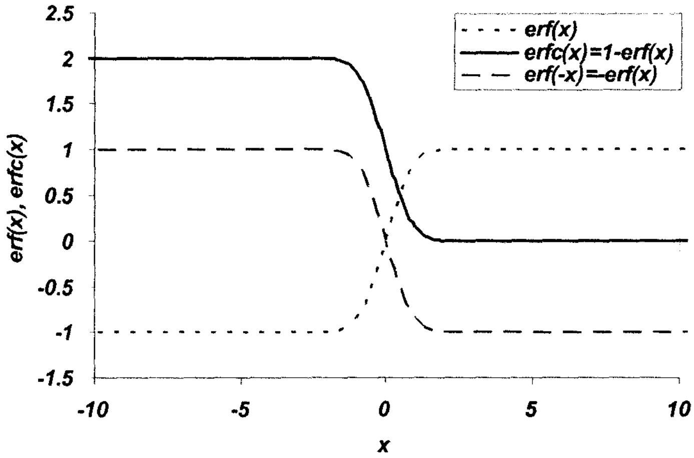

Figure C.1 The error function *erf*(*x*) and complementary error function *erfc*(*x*)

C.2 Solution Function *F*(*x*) of Diffusion Equation

The solution of 1D diffusion equation, from (2.29), is a function $F(x)$ related to error functions, which have the following normalized form,

$$F(x)=\frac{1}{2}\left[erf\left(\frac{W-x}{D}\right)+erf\left(\frac{W+x}{D}\right)\right] \qquad \text{(C.5)}$$

where W is the half-width of the strip (i.e., $2W$ is the width of the strip), D is the diffusion length. From (C.4), it is found that $F(x)$ is an even function of the variable x: $F(-x) = F(x)$. In general, the function $F(x)$ is a function of variables W, D, and x.

Here we can prove that function $F(x)$ becomes unity when $W \gg D$ (e. g., $W = 10D$) and a Gaussian function when $W \ll D$ (e. g., $W = 0.1D$) analytically and numerically. According to the definition of error function of (C.1), when $W \gg D$, the function $F(x)$ becomes,

$$\begin{aligned} F(x) &= \frac{1}{2}[erf(\frac{W-x}{D})+erf(\frac{W+x}{D})]\approx erf(\frac{W}{D}) \\ &= \frac{2}{\sqrt{\pi}}\int_0^{\infty}\exp(-u^2)du = erf(\infty) = 1 \end{aligned} \qquad \text{(C.6)}$$

where an equality of $\int_0^{\infty}\exp(-u^2)du = \sqrt{\pi}/2$ was used. When $W \ll D$, the function $F(x)$ becomes,

$$\begin{aligned} F(x) &= \frac{1}{2}[erf(\frac{x+W}{D})-erf(\frac{x-W}{D})] = \frac{1}{\sqrt{\pi}}\int_{(x-W)/D}^{(x+W)/D}\exp(-u^2)du \\ &= \frac{1}{D\sqrt{\pi}}\int_{-W}^{W}\exp(-(x-u)^2/D^2)du \approx \frac{2W}{D\sqrt{\pi}}\exp\left(-\frac{x^2}{D^2}\right) \end{aligned} \qquad \text{(C.7)}$$

which is the Gaussian function with a amplitude of $2W/(D\sqrt{\pi})$.

On the other hand, we prove (C.6) and (C.7) numerically. Without loss of generality, we assume that $D = 4$ μm. The curves of $F(x)$ for different $W = 100, 10, 4, 0.1$, and 0.01 μm are shown in Figure C.2. From Figure C.2, it is found that curves of the function $F(x)$ with $W > 10$ μm are unity. In order to show the Gaussian-like behavior of the function $F(x)$, the values of normalized function $F'(x) = D\sqrt{\pi}F(x)/2W$ with the Gaussian function $\exp(-x^2/D^2)$ are shown in Figure C.3.

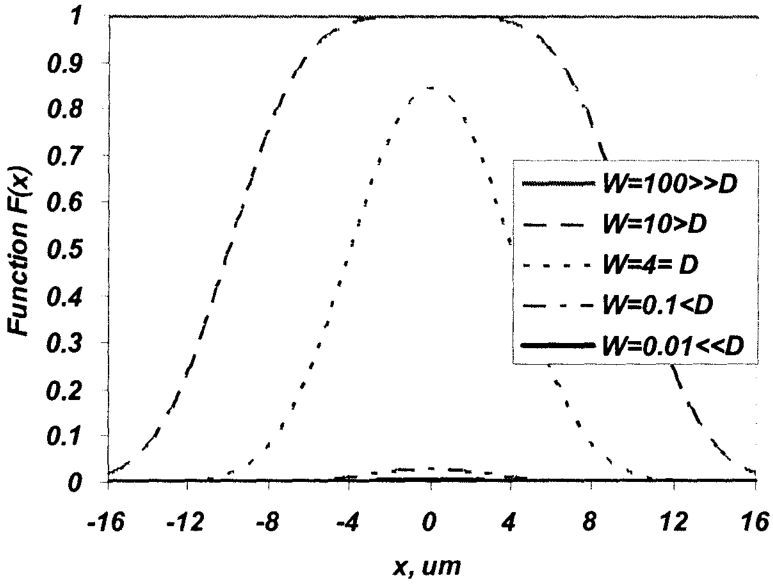

Figure C.2 The solution F(x) of 1D diffusion equation with different W

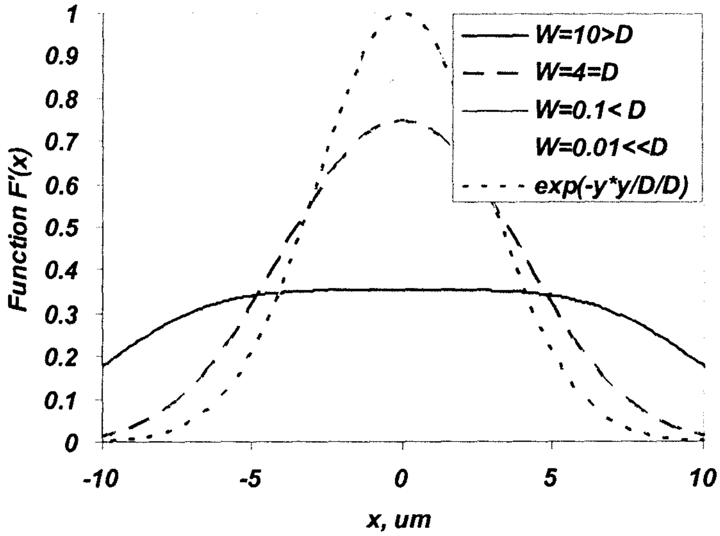

Figure C.3 The normalized $F'(x)$ of 1D diffusion equation with small W/D

From Figure C.3, it is found that curves with $W < 0.1$ μm are indistinguishable with the Gaussian function. In other words, when $W << D$ (or $W = 0.1$ μm), the solution Function $F(x)$ of the diffusion equation becomes a Gaussian function.

C.3 Law of Conservation of the Matter

Finally, a very interesting property of the function $F(x)$ can be obtained analytically or numerically. For example, from (C.6) with the equality $\int_0^{\infty} \exp(-x^2/D^2)dx = D\sqrt{\pi}/2$, we have

$$\int_{-\infty}^{\infty} F(x)dx = 2W \qquad \text{(C.8)}$$

which is called the law of conservation of the matter and means that total matter on the strip is normalized with respect to the strip width $2W$ and the law of conservation of the matter is guaranteed no matter how changes of the diffusion length D.

For a two-dimensional waveguides with a strip width $2W$ and thickness τ, the law of conservation of the matter has the following formula,

$$\int_{-\infty}^{\infty} dy \int_0^{\infty} C(x,y)dx = \int_{-\infty}^{\infty} G(y)dy \int_0^{\infty} F(x)dx = 2\tau W \qquad \text{(C.9)}$$

where the function $C(x,y)= F(x)G(y)$ and the $G(y) = \frac{1}{2}\left[erf\left(\frac{\tau - y}{D'}\right) + erf\left(\frac{\tau + y}{D'}\right)\right]$ are used.

References

[1] R. C. Alferness, "Guided-wave devices for optical communication (Invited paper)," *IEEE J. Quantum Electron.*, vol.17, pp. 946-, 1981.

[2] R. C. Alferness, "Waveguide electro-optic modulators (Invited paper)," *IEEE Trans. Microwave Theory Technol.*, vol. 30, no. 8, pp. 1121–1137, 1991.

[3] P. Ganguly, D. C. Sen, S. Datt, J. C. Biswas, and S. K. Lahiri, "Simulation of refractive index profiles for Titanium induffused lithium niobate channel waveguides," *Fiber and Integrated Optics*, vol. 15, pp.135-147, 1996.

[4] C.-C.Chen, V. Armbruster, H. Porte, A. Carenco, and J.-P. Goedgebuer, "Effective refractive index change of X-cut Z-propagation Ti:LiNbO$_3$ waveguides by laser ablation," *Opt. Eng.*, vol. 41, no. 11, pp. 2930 –2933, 2002.

[5] W. Charczenko, I. Januar, and A. R. Mickelson, "Modeling of proton-exchanged and annealed channel waveguides and directional couplers," *J. Appl. Phys.,* vol. 73, no. 7, pp. 3139–3148, 1993.

[6] L. P. Shen, H. Wang, C. Xu, and W.-P. Huang, "Numerical analysis of multimode interference effect in Ti:LiNbO$_3$ waveguides," Paper No. 5970A-33, Photnic North 2005.

[7] H. Wang, W.-P. Huang, and C. Q. Xu, "Comparative study of modeling and characterization of diffused LiNbO3 waveguides," Paper No. 5970A-20, Photnic North 2005.

[8] B. T. Matthias and J. P. Remeika, "Ferroelectricity in the Ilmenite Structure," *Phys. Rev.*, vol. 76, pp. 1886–1887, Nov. 1949.

[9] Crystal Technology Inc., "Lithium niobate devices finally make it to market," *Electronics*, vol. 76, no. 10, pp. 20–21, Nov. 1986.

[10] M. V. Hobden and J. Warner, "The temperature dependence of the refractive indices of pure lithium niobate," *Phys. Lett.*, vol. 22, no. 3, pp. 243–244, 1966.

[11] E. Strake, G.P. Bava, and I. Montrosset, "Guided modes of Ti:LiNbO$_3$ channel waveguides: a novel quasi-analytical technique in comparison with the scalar finite-element method," *J. Lightwave Technol.,* vol. 6, no. 6, pp. 1126- 1135, June 1988.

[12] E. D. Palik, *Handbook of optic constants of solid.* 2nd edition, New York: Academic Press, 1998.

[13] U. Schlarb and K. Betzler, "Refractive indices of lithium niobate as a function of wavelength and composition," *J. Appl. Phys.,* vol. 73, no. 7, pp. 3472–3476, 1993.

[14] D. S. Smith and H. D. Ricciys, "Refractive indices of lithium niobate," *Opt. Comm.*, vol. 17, pp. 332-335, 1976.

[15] J. Crank, The *mathematics of diffusion.* Oxford, U. K.: Carendon Press, 1975.

[16] S. Fouchet, A. Carenco, C. Daguet, R. Guglielmi, and L. Riviere, "Wavelength dispersion of Ti induced refractive index change in LiNbO3as a function of diffusion parameters," *J. Lightwave Technol.,* vol. 5, no. 5, pp. 700 - 708, May 1987.

[17] J. M. Zavada, H. C. Casey, Jr. and R. J. States, S. W. Novak, and A. Loni, "Correlation of substitutional hydrogen to refractive index profiles in annealed proton-exchanged Z- and X-cut $LiNbO_3$," *J. Appl. Phys.,* vol. 77, no. 6, pp. 2697–2708, 1995.

[18] M. D. Feit and J. A. Feck, "An analysis of intersecting diffused channel waveguides," *IEEE J. Quantum Electron.*, vol. 21, no. 11, pp. 1799-1805, Apr. 1984.

[19] C. L. Xu, W. P. Huang, M. S. Stern, and S. K. Chaudhuri, "Full-vectorial mode calculations by finite difference method," *IEE Proc.-J*, vol. 141, no. 5, pp. 281-286, 1994.

[20] W. W. Lui, K. Magari, N. Yoshimoto, S. Oku, T. Hirono, K. Yokoyama, and W.-P. Huang, "Modeling and design of bending waveguide based semiconductor polarization rotators," *IEEE Photon. Technol. Lett.*, vol. 9, pp. 1379 -1381, 1997.

[21] M. J. P. Berenger, "A perfectly matched layer for the adsorption of electromagnetic waves," *J. Comput. Phys.*, vol. 114, pp. 185-200, 1994.

[22] L. P. Shen, "Modeling and design of photonic crystal waveguides and fibers," Ph. D. thesis, McMaster University, 2003.

[23] R. V. Schmidt and I. P. Kaminow, "Metal-diffused optical waveguides in $LiNbO_3$," *Appl. Phys. Lett.*, vol. 25, no.8, pp. 458-460, 1974.

[24] M. Fontaine, A. Delage, and D. Landheer, "Modeling of titanium diffusion into $LiNbO_3$ using a depth-dependent drffusion coefficient," *J. Appl. Phys.*, vol. 60, no. 7, pp. 2343–2350, 1986.

[25] E. Strake, G.P. Bava, and I. Montrosset, "Guided modes of $Ti{:}LiNbO_3$ channel waveguides: a novel quasi-analytical technique in comparison with the scalar finite-element method," *J. Lightwave Technol.*, vol. 6, no. 6, pp. 1126- 1135, June 1988.

[26] M. Minakata, S. Saito, M. Shibata, and S. Miyazawa, "Precise determination of refractive-index changes in Ti-diffused $LiNbO_3$ optical waveguides," *J. Appl. Phys.*, vol. 49, no. 9, pp. 4677–4682, 1978.

[27] M. Minakata, S. Saito, and M. Shibata, "Two-dimensional distribution of refractive-index changes in Ti-diffused $LiNbO_3$ strip waveguides," *J. Appl. Phys.*, vol. 50, no. 5, pp. 3063–3067, May 1979.

[28] W. K. Burns, P. H. Klein, E. J. West, and L. E. Plew, "Ti diffusion in Ti: $LiNbO_3$ planar and channel optical waveguides," *J. Appl. Phys.*, vol. 50, no. 10, pp. 6175–6182, 1979.

[29] M. Fukuma, J. Noda, and H. Iwasaki, "Optical properties in titanium-diffused LiNbO3 strip waveguides," *J. Appl. Phys.*, vol. 49, no. 7, pp. 3693–3698, 1978.

[30] M. Fukuma and J. Noda, "Optical properties of titanium-diffused $LiNbO_3$ strip waveguides and their coupling-to-a-fiber characteristics," *Appl. Opt.*, vol. 19, no. 4, pp. 591–597, 1980.

[31] J. Ctyroky, M. Hofman, J. Janta, and J. Schrofel, "3-D analysis of $LiNbO_3$: Ti channel waveguides and directional couplers," *IEEE J. Quantum Electron.*, vol. 20, no. 4, pp. 400-409, Apr. 1984.

[32] M. D. Feit and J. A. Feck, "Comparison of calculated and measured performance of diffused channel-waveguide couplers," *J. Opt. Soc. Am.*, vol. **73**, no. 10, pp. 1296-1304, 1983.

[33] Photon Inc, “Beam Pro Model 2350 Video laser beam profiler,” *www.photon-inc.com*, 2004.

[34] J. L. Jackel, C. E. Rice, and J. 1. Veselka, “Proton exchange for high-index waveguides in LiNbO3,” *Appl. Phys. Lett.*, vol. 41, no. 7, pp. 607-608, 1982.

[35] M. De Micheli, J. Botineau, S. Neveu, P. Sibillot, and D. B. Ostrowsky, “Independent control of index and profiles in proton-exchanged lithium niobate guides,” *Opt. Lett.*, vol.8, no.2, pp. 114-115, 1983

[36] M. De Micheli, D. Ostrowsky, J. Barety, C. Canali, A. Carnera, G. Mazzi, and M. Papuchon, “Crystalline and optical quality of proton exchanged waveguides,” *J. Lightwave Technol.*, vol. 4, no. 7, pp. 743–745, July 1986.

[37] C. Canali, A. Carnera, G. Della Mea, P. Mazzoldi, S. M. Al Shukri, A. C. G. Nutt, and R. M. De La Rue, “Structural characterization of proton exchanged LiNbO3 optical waveguides,” *J. Appl. Phys.*, vol. 59, no. 8, pp. 2643-2649, 1986.

[38] I. Savatinova, S. Tonchev, R. Todorov, Mario N. Armenise, V. M. N. Passaro, and C. C. Ziling, “Electro-Optic Effect in Proton Exchanged LiNbO3 and LiTaO3 Waveguides,” *J. Lightwave Technol.*, vol. 14, no. 3, pp. 403–409, March 1996.

[39] D. F. Clark, A. C. G. Nutt, K. K. Wong, P. J. R. Laybourn, and R. M. De La Rue, “Characterization of proton-exchange slab optical waveguides in z-cut $LiNbO_3$,” *J. Appl. Phys.*, vol. 54, no. 11, pp. 6218-6220, 1983.

[40] M. L. Bortz and M. M. Fejer, “Annealed proton-exchanged $LiNbO_3$ waveguides,” *Opt. Lett.*, vol.16, no.23, pp. 1844-1846, 1991.

[41] W. Charczenko, P. S. Weitzman, H. Klotz, M. Surette, J. M. Dunn, and A. R. Mickelson, “Characterization and simulation of proton exchanged integrated optical modulators with various dielectric buffer layers,” *J. Lightwave Technol.*, vol. 9, no. 1, pp. 92–100, 1991.

[42] W. Charczenko, I. Januar, and A. R. Mickelson, “Modeling of proton-exchanged and annealed channel waveguides and directional couplers,” *J. Appl. Phys.*, vol. 73, no. 7, pp. 3139–3148, 1993.

[43] I. Januar and A. R. Mickelson, "Characteristics of S-shaped waveguide structures by the annealed proton exchange process in $LiNbO_3$," *J. Lightwave Technol.,* vol. 12, no. 12, pp. 2044–2051, Dec. 1993.

[44] M. M. Howerton, W. K. Burns, P. R. Skeath, and A. S. Greenblatt, "Dependence of refractive index on hydrogen concentration in proton exchanged $LiNbO_3$," *IEEE J. Quantum Electron.*, vol. 27, pp. 593–601, Mar. 1991.

[45] F. F. Zhang, "Modeling and fabrication of annealed proton exchanged $LiNbO_3$ waveguides", M. Sc. Thesis, McMaster University, 2004.

[46] J. Helms, J. Schmidtchen, B. Schuppert, and K. Petermann, "Error analysis for refractive-index profile determination from near-field measurements," *J. Lightwave Tech.*, vol. 8, no.5, pp. 625–633, 1990.

[47] J. M. White and P. F. Heidrich, "Optical waveguide refractive index profiles determined from measurement of mode indices: A simple analysis," *Appl. Opt.,* vol. 15, pp. 151–155, 1976.

[48] K. S. Chiang, "Construction of refractive index profiles of planar dielectric waveguides from the distribution of effective indexes," *J. Lightwave Technol.,* vol. 3, p. 385–391, 1985.

[49] K. S. Chiang, C. L. Wong, H. P. Chan, and Y. T. Chow, "Refractive-index profiling of graded-index planar waveguides from effective indexes measured for both mode types and at different wavelengths," *J. LightwaveTechnol.*, vol. 14, pp. 827–832, 1996.

[50] L. McCaughan and E. R. Bergmann, "Index distribution of optical waveguides from their mode profile," *J. Lightwave Technol.*, vol. LT-1, pp. 241–244, Jan. 1983.

[51] I. Mansour and F. Caccavale, "An improved procedure to calculate the refractive index profile from the measured near-field intensity," *J. Lightwave Technol.,* vol. 14, p. 423, 1996.

[52] F. Caccavale, F. Gonella, G. Caneva, and I. Mansour, "Iterative simplex-finite difference method for the characterization of optical waveguides," *J. Lightwave Techn.,* vol. 14, p. 1825, 1996.